Said Al Rabadi

Prediction of droplet velocity and rain out in horizontal, isothermal two-phase free jet flows

Prediction of droplet velocity and rain out in horizontal, isothermal two-phase free jet flows

Dem Promotionsausschuß der

Technischen Universität Hamburg-Harburg

zur Erlangung des akademischen Grades

Doktor-Ingenieur

vorgelegte Dissertation

von

M. Sc. Said Al Rabadi

aus Ajloun, Jordanien

2007

Vorsitzender des
Prüfungsausschusses: Prof. Dr.-Ing. H. Herwig

1. Gutachter: Prof. Dr.-Ing. L. Friedel
2. Gutachter: Prof. Dr.-Ing. R. Eggers

Tag der mündlichen Prüfung: 18. Dezember 2007

Acknowledgment

Abstract

Investigations on two-phase free jets generally do not include much useful information on the near field behavior of the jet, where significant entrainment affects the two-phase flow. Uncertainties also remain regarding to the applicability of the laboratory results to large scale releases which might occur in real accidents. In industrial two-phase free jet flows, a model for the droplet velocity and rain out is needed for hazard and risk analysis. They depend on the self establishing droplet size distribution and velocity profile. The two-phase flow predictive models for droplet size and velocity include viscosity as intrinsic variable. They simply extend or correct single-phase flow models or base on two-phase flow experiments performed with liquid phase of relatively low viscosity. The major aim is the development of a validated two-phase jet dispersion model based on the process of liquid phase atomization induced by shear flow for the case of high viscosity liquid phase.

Two-dimensional Phase Doppler Anemometer measurements of the droplet size and the velocity, conducted under several nozzle conditions and a systematic variation of the air mass flow quality and the liquid phase viscosity, show that the jet perimeter is lower and the breakup length is longer in the free jet flow of air and relatively higher viscosity liquid phase. In this case the air entrainment process is enhanced and, in parallel, the Sauter droplet diameter decreases with increasing air/ liquid phase mass flow ratio. This leads to substantial liquid breakup, hence, fragments with small sizes are formed. The trend is also significant with higher liquid viscosity than that of water. The higher liquid viscosity affects the droplet formation by reducing the rates of surface perturbations and consequently droplet distortions, ultimately leading to the formation of smaller droplets. The axial droplet velocity decreases with the nozzle downstream distance due to the continual air entrainment and due to the collisions of droplets. In turn the droplet collisions may induce further liquid fragmentation, hence, formation of a large number of relatively smaller droplets, or the agglomeration to comparatively larger liquid droplets that may rain out the free jet. The combined effects of air entrainment and liquid fragmentation as well possible coalescence of droplets produce, in comparison to air/ water free jet flow, a specific bimodal droplet size distribution. At the same time, the liquid density as well the surface tension vary with increasing the liquid viscosity. Yet no systematic trends are incorporated for the effect of these physical properties on air entrainment.

A two-zone entrainment model is proposed as a function of the normalized axial distance. It is based on physical aspects of dispersion flows such as droplet acceleration and deceleration, and utilizes a variable two-phase entrainment coefficient and a virtual origin related to the nozzle Reynolds number. The proposal for predicting the droplet velocity and rain out in the free jet flow allows also for an adequate reproduction of the experimental data in comparison with those predicted by two-phase dispersion models in the literature. Moderate extrapolatability of the proposal with respect to other jet flow orientation, fluid type, outlet condition and geometry is expected in view of the physics-based modelling.

Contents

1 Introduction

The dispersion of two-phase flows has received considerable interest in the industry since they may originate from a leakage of a flange connection, a wall crack or from the accidental release of an industrial unit running under an inadmissible overpressure. Such releases have a potentially hazardous impact on the environment and the personnel health. For risk and hazard assessment, the spread width and the intact length scale of the established jet flow are required for the computer codes utilizing integral, resp., multidimensional balance equations of mass, energy, momentum and species. For solving these equations essential closure parameters in the form of submodels are required, namely, the entrainment coefficient which is characterizing the mixing of the entrained air from the ambient with the free jet flow. Regarding the droplet rain out, a droplet size model must be determined allowing for the definition of a characteristic droplet diameter which, in turn, depends on the self-establishing droplet size spectrum and velocity distribution.

Droplets are generated from the liquid disintegration process in the case of two-phase free jet flow. Concerning the type of the droplet disintegration, it may be caused due to the fluid dynamic shear stress induced by the velocity difference between both phases in the jet flow, or by superimposed violent phase change (flashing) of the liquid or the liquefied pressurized gas. The codes are valid only in narrow parameter boundaries to model two-phase dispersion flows on the physical basis. Hence, there is still a lack of validated descriptive parameters for the effect of fluid properties (viscosity, density, surface tension, droplet coalescence affinity, etc.) on the behavior of two-phase free jet flow.

1.1 Status

The jet flow is accelerated to a certain downstream distance. This is possible by only the air expansion, i.e., higher outlet pressure than that of the ambient. Thus, the expansion induces unstable flow perturbations on the liquid bulk ultimately leading to the breakup. The liquid disintegration is significantly affected by the aerodynamic forces associated with both the co-flowing and the entraining air into the jet. Observations of the droplet deformation in two-phase free jet flow confirm that the interactions between the air stream and the liquid bulk surface are becoming significant. Hence, the air entrainment process is especially enhanced in the jet far field region at a downstream distance of longer than 30 nozzle outlet diameters, due to the contribution of both the co-flowing and the entraining air streams in the two-phase free jet flow. Meanwhile, the effect of the liquid properties, especially the viscosity on the air entrainment in two-phase air/ liquid free jet, is still stochastic. Indeed, the liquid viscosity influences the primary droplet deformation and the secondary breakup through higher shear stresses continuously acting on the droplet surface. The disruptive and the adhesive, resp., conservation forces for each particular droplet compete along with the downstream distance.

On the other hand, analytical approaches involving the disintegration of the liquid bulk and the assessment of the jet breakup length are still a questionable general validity for the two-phase air/ liquid dispersion flows. The two-phase predictive models for droplet size and velocity include simplifications which may be applied to single-phase flow or two-phase dispersion experiments performed with a liquid phase of relatively low viscosity. Further uncertainties also remain regarding the extrapolation of the laboratory results to large scale releases which might occur in real industrial releases with fluids of a relatively higher viscosity.

1.2 Aim

In the frame of this work a two-phase entrainment model based on the upstream flow conditions of an air/ high viscosity liquid phase will be developed. This model accounts for the droplet formation process under the effect of the interactions between the turbulent air flow and the liquid bulk. Furthermore, the model validates the influence of the liquid phase properties, especially the influence of viscosity on the droplet velocity, rain out and air entrainment. Essentially, it would provide sufficient information to better understand the dispersion flow behavior and to assess the reproductive accuracy in comparison with other predictive models.

1.3 Thesis structure

In the next chapter, the characteristics of the single- and two-phase free jet flows will be reviewed to understand the conceptual aspects of such flow kinds. The related work in the field of two-phase air/ liquid free jets will be studied in the third chapter to shed light on the trials that are relevant to this subject. The experimental investigations with a description of the instrumentation and the methodology as well as the experimental results such as the mean droplet velocity and size spectra will be presented in the fourth chapter. Later on the analytical investigations involving self-proposed correlations and the derivation of trends are to be discussed in the fifth chapter. The sixth chapter focuses on the implication of the results along with the drawbacks encountered in the model validity and recommendations for further work. The seventh and the final chapter is a summary of the most important results.

2 Characteristics of single- and two-phase free jet flows

Free jet flows are established with particular behavior of mixing the content of the free jet with the surrounding, i.e., entraining the ambient fluid into the jet flow. For the sake of illustration, single-phase free jet flow is described in the next section.

2.1 Single-phase free jet flow

The release of a single-phase from a nozzle is considered as turbulent flow, where the Reynolds number, calculated based on the outlet conditions, is in excess of 5000 - 8000. Fig. 1 depicts the classification of air entrainment into the jet flow as was previously investigated. According to Chiang et al. [12], Epstein et al. [21], Hirst [36], Muralidar [73], Ooms [76], Schefer et al [89], Tickle et al. [99] or Woodward [114], the entrainment process can be classified into three main regimes dominated by:

1. Momentum. The jet flow is typically characterized in this regime by a dispersion flow originates from a venting nozzle to the ambient, where the storage pressure is normally higher than that of the ambient. At the nozzle outlet, this pressure difference will be converted into other forms mostly the kinetic energy. Consequently, the jet flow will be establishing with a significant outlet velocity higher than that of the ambient. With the nozzle downstream distance, the mean jet velocity will decrease due to mixing of the jet content with the ambient. The degree of mixing or so called the entrainment in this regime provides the potential for the decrease of the mean jet velocity and, hence, the rate of momentum transfer between the jet flow and the ambient.

2. Buoyancy/ gravity. The entrainment process is influenced in this regime to a great extent by the physical properties of the jet content, especially in the case of dense fluid dispersion of a distinctly different density from that of the ambient. The jet flow losses its momentum to the surrounding. The jet flow raises in the ambient due to the buoyancy effects in case of lower fluid density than that of the ambient, or settles down under the gravity force in case of high fluid density. At the final stage of this regime, the jet flow touches the ground level leading to wet the contact area and forming the liquid pool.

3. Atmospheric turbulence. The jet flow in this regime is sufficiently mixed and approaches an asymptotic condition close to that of the ambient. In reality, an alteration in the thermal or in the turbulent state of the atmosphere may happen leading to the evaporation from the pool. The entrainment is then affected to a great extent by the ambient state.
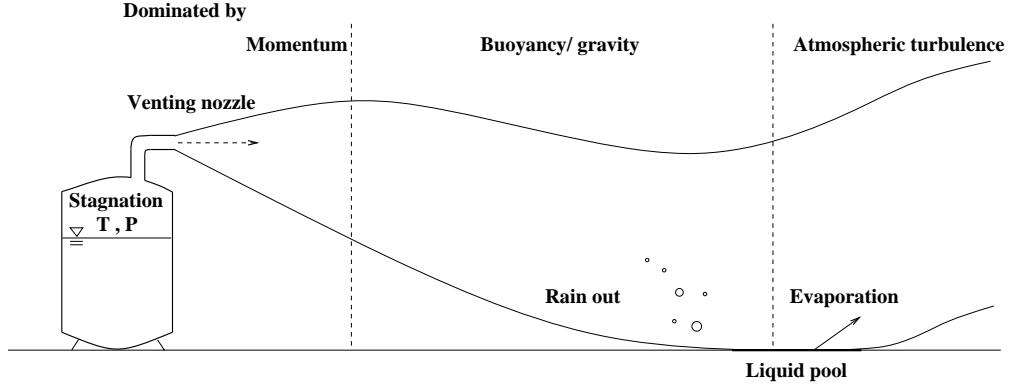
Fig. 1: Classification of air entrainment into a turbulent dispersion from a nozzle (dimensions of the Momentum dominated regime are overscaled)

For an estimation of the dominating length of each regime, Chiang et al. [12] and Epstein et al. [21] proposed field criteria to distinguish between the domination boundaries of the Momentum and the Buoyancy/ gravity regimes. In the near field, they define the Momentum length scale, while the Buoyant length scale was suggested for the far field regime. The length scales were determined according to the following correlations

$$L_{Moment} = \frac{u_{jet} \cdot d_{Nozzle}}{u_{Nozzle} \cdot C_{Ent,\,Moment}}$$

$$L_{Buoy} = \frac{g \cdot u_{jet} \cdot d_{Nozzle}^2 \cdot (T\,(P_{outlet}) - T\,(P_{ambient}))}{u_{Nozzle}^3 \cdot T\,(P_{ambient}) \cdot C_{Ent,\,Buoy}} \quad ,$$

where L_{Moment} and L_{Buoy} are the Momentum and the Buoyant length scales. u_{jet} is the mean jet velocity. $C_{Ent,\,Moment}$, $C_{Ent,\,Buoy}$ are the entrainment coefficients for the regimes dominated by Momentum and Buoyancy/ gravity effects. The Momentum length scale was determined by the downstream location where the jet velocity approaches that of the ambient. While, the Buoyant length scale was determined based on the downstream distance where the evaporation of the dispersed fluid is obvious. In the study by Epstein et al. [21], the entrainment process dominated by Momentum and Buoyancy/ gravity effects were only considered and given the values of 0.1, resp., 0.5 to the entrainment coefficient. The Atmospheric turbulence effects were neglected since the phase change was presumed to be established within the Buoyant/ gravity dominated regime. In general, the proposed values for the entrainment coefficient vary according to their definition. The entrainment coefficient is typically defined according to two common entrainment models used in the dispersion codes, namely the Morton et al. [72] and Ricou et al. [86] definitions. For illustration, a single-phase air free jet flow into the ambient will be considered. The definitions of the entrainment coefficient according to these models read

$$C_{Ent} = \frac{u_{Air(P_{ambient})}}{u_{Air_{jet}}} \qquad \text{Morton et al. [72]}$$

$$C_{Ent} = \frac{u_{Air(P_{ambient})}}{u_{Air_{jet}}} \sqrt{\frac{\rho_{Air(P_{ambient})}}{\rho_{Air_{jet}}}} \qquad \text{Ricou et al. [86]}$$

Here $u_{Air(P_{ambient})}$ and $u_{Air_{jet}}$ are the air velocity of the ambient and the jet flow. Webber et al. [107] and Buchlin et al. [9] illustrate in a detailed comparison of the above entrainment models an appropriate selection of the values for the single-phase entrainment coefficient. The only difference between these definitions is that Ricou et al. [86] accounts for the density ratio of the ambient air to that of the jet while Morton et al. [72] disregards the effect of the density ratio on the entrainment. Indeed, the predictions by these models are apparently different when applied to the case of free jet flow of fluid with physical properties distinctly differ from those of the ambient air. In total, the applicability of the relevant entrainment model will differ according to the regime of interest.

The overall mass balance on the jet flow considering the entrainment processes in the three regimes reads

$$\frac{d[\rho \cdot u \cdot A]_{jet}}{ds} = \dot{M}_{Ent,Total} = \dot{M}_{Ent,Moment} + \dot{M}_{Ent,Buoy} + \dot{M}_{Ent,Atmos}$$

$$= \frac{\pi}{2} \cdot d_{jet}(s) \cdot \rho_{Air(P_{ambient})} \cdot \left(C_{Ent,Moment} \cdot u_{jet}(s) + u_{Air(P_{ambient})}(C_{Ent,Buoy} + C_{Ent,Atmos}) \right) \quad ,$$

where $\dot{M}_{Ent,Total}$ is the total entrainment rate. $d_{jet}(s)$ and $u_{jet}(s)$ account for the jet diameter and the velocity with the downstream distance. The total entrainment rate into the jet flow is taken as the summation of the three individual entrainment rates. $C_{Ent,Moment}$, $C_{Ent,Buoy}$ and $C_{Ent,Atmos}$ are the entrainment coefficients for the Momentum, the Buoyancy/ gravity and the Atmospheric turbulence dominated regimes. Typical values for these entrainment coefficients are listed in Tab. 1.

Model	$C_{Ent,Moment}$	$C_{Ent,Buoy}$	$C_{Ent,Atmos}$
Muralidar [73]	0.081	0.5	1.0
Tickle et al. [99]	0.074	0.6	1.0
Ooms [76] and Chiang et al. [12]	0.057	0.5	1.0
Woodward [114]	0.04	0.2	0.25

Tab. 1: Typical values for the entrainment coefficients in the Momentum, Buoyancy/ gravity and Atmospheric dominated regimes

Clearly, the value stated for the entrainment coefficient in the Momentum dominated regime is relatively lower than those for the other regimes of Buoyancy/ gravity and Atmospheric turbulence. This is attributed to the smaller jet periphery in comparison to that in the other regimes. For instance, Muralidar [73] had chosen the entrainment coefficient as 0.081, 0.5 and

1.0 for $C_{Ent,Moment}$, $C_{Ent,Buoy}$ and $C_{Ent,Atmos}$. The Momentum dominated regime entrainment coefficient had been chosen to match the experiments by Ricou et al. [86]. Tickle et al. [99] proposed a model for single-phase dense gas dispersion flows proposing values of 0.074, 0.6 and 1.0 for the entrainment coefficient in the Momentum, the Buoyancy/ gravity, resp., the Atmospheric turbulence dominated regimes. Accordingly, the entrainment coefficient follows the Morton et al. [72] model, where no consideration is given to the jet properties variations from those of the ambient. Ooms [76] and Chiang et al. [12] assumed the value of 0.057 for the entrainment coefficients in the Momentum dominated regime obtained from stack gas releases data, while the entrainment coefficient for the Buoyancy/ gravity and for the Atmospheric turbulence regimes are identical to those used by Muralidar [73]. The entrainment coefficients were given values of 0.04, 0.2 and 0.25 by Woodward's model [114] in the Momentum, the Buoyancy/ gravity and the Atmospheric dominated regime. In general, these models propose different values for the entrainment coefficients in order to fit the experimental data in the relevant regime, as well as to account for the jet flow changes with the downstream distance. Many industrial applications focus on the entrainment process in the momentum dominated region. This fact will be described in more details in the next section.

2.1.1 Gas free jet flow

The idealized behavior of a stationary, compressible, subcritical, single-phase gas free jet flow from a nozzle into a quiescent ambient with the same pressure, is depicted in Fig. 2. Downstream of the nozzle, an idealized time-averaged mean boundary is established between the jet flow and the ambient. It is highly unstable and subject to rotational flow instabilities that eventually lead to the formation of large scale vortical structures as indicated by the arrows. The interaction of these structures with the surrounding produces strong flow fluctuations, entraining ambient fluid into the jet fluid, and enhancing the mixing. The jet flow is, by convention, characterized by three distinct regions. The Core region with a conical velocity profile in which only the centerline nozzle outlet velocity is preserved. Ultimately, the core region disappears at a downstream distance of about five nozzle outlet diameters. Further downstream, the flow enters the Transition region where the jet boundary spreads due to the entrainment. Then the jet flow ideally establishes a rotationally symmetric velocity profile, or what is called the bell-shaped velocity distribution. The maximal axial velocity is found on the jet centerline.

The velocity decreases in the radial direction towards the jet periphery to equalize - on average - to that of the surrounding, if a quiescent ambient does not prevail. The so called half jet spread angle, $\beta_{0.5}$, is the inclination angle of the line that passes through the half way point of the maximum velocity at each axial distance and the jet centerline. The half jet spread angle is related to the entrainment coefficient that characterizes the amount of the entrained gas into the jet, and the corresponding self-establishing virtual origin that is determined by the downstream distance between the intersection point and the nozzle outlet.
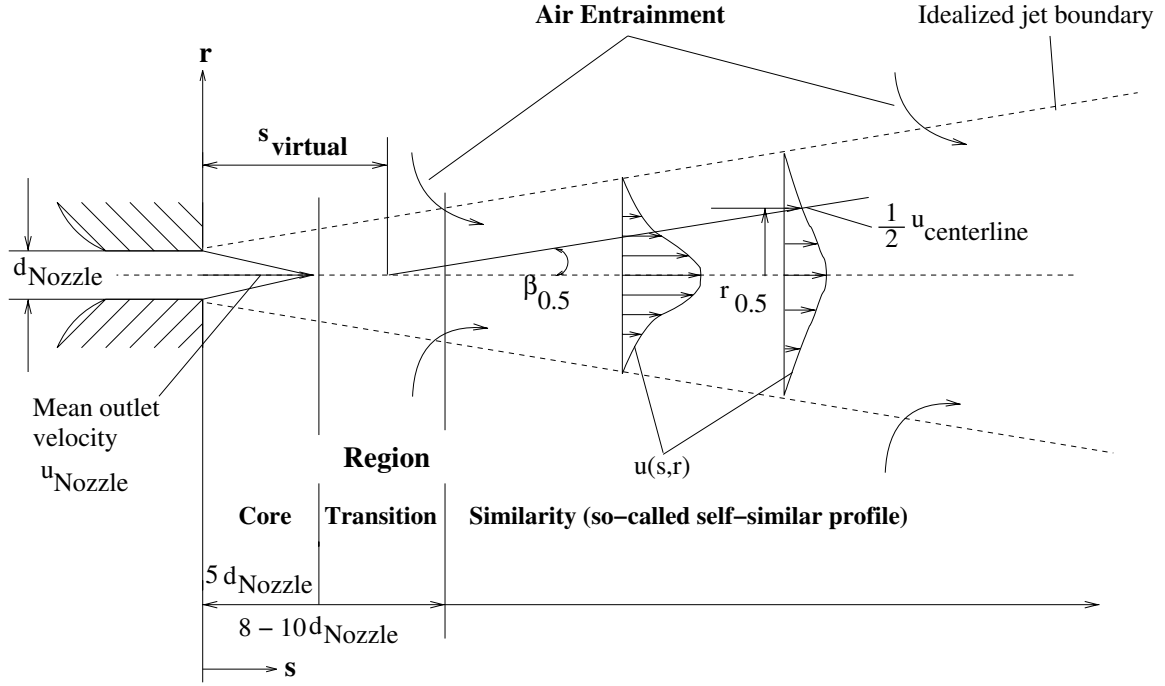
Fig. 2: Characteristics of a subcritical gas free jet flow in quiescent ambient with the same pressure (nozzle downstream dimensions are underscaled)

The fluctuations in the turbulent jet flow, along the downstream distance, result in entraining the ambient air into the jet flow. For a proper interpretation of this finding, turbulence and balance equations will be presented in the next section.

Turbulence and balance equations

After a jet is established, the flow produces the rolling up of a vortex at the jet boundary. Subsequent amplifications involve the formation of a relatively greater strength vortex through the pairing of individual vortices. Further downstream, the vortices become heavily distorted and less distinct. Many large scale eddies are established and, hence, the jet flow undergoes rapid transition to the fully turbulent region. The small scale of the eddy motion occurring in the turbulent flow is dictated by the gas viscous forces. The eddy Reynolds number is based on the characteristic velocity and length scale for which the gas viscous effects become dominant. Work is performed against the action of viscous stresses, so that the energy associated with the eddy motion is dissipated and converted into other forms such as overproportional deceleration of the jet. The eddy Reynolds number of a gas flow gives a measure of the competence between inertial and viscous forces. It is defined by

$$Re_{Gas_{jet}} = \frac{u_{Gas_{jet}} \cdot L_{jet} \cdot \rho_{Gas(P_{outlet})}}{\eta_{Gas(P_{outlet})}} \qquad ,$$

7

where $u_{Gas_{jet}}$ is the mean gas velocity at the nozzle outlet. L_{jet} is the characteristic eddy length, $\rho_{Gas(P_{outlet})}$ and $\eta_{Gas(P_{outlet})}$ are the gas density and viscosity calculated at the outlet conditions. In general, it would be pertinent to characterize a turbulent flow by the mean gas velocity and its fluctuations. Furthermore, visualizations of the turbulent flows reveal rotational flow structures, the so called turbulent eddies, with a range of the length scale approximately ten times larger than the nozzle outlet diameter as was stated by Middlemann [71]. The relatively higher turbulent eddies interact with the ambient and extract the kinetic energy from the jet flow to build up vortical structures, hence, they gradually slow the jet flow with the downstream distance.

The general balance equations for a horizontal gas free jet read

$$\text{Species :} \qquad \frac{d[c \cdot u \cdot A]_{jet}}{ds} = 0$$

$$\text{Mass :} \qquad \frac{d[\phi \cdot u \cdot A]_{jet}}{ds} = \frac{\pi}{2} \cdot C_{Ent} \cdot d_{jet}(s) \cdot u_{Gas_{jet}}$$

$$\text{Momentum:} \qquad \frac{d[\phi \cdot u^2 \cdot A]_{jet}}{ds} = C_{Ent} \cdot u_{Gas_{jet}} \cdot \frac{d[\phi \cdot u \cdot A]}{ds} - g \cdot \frac{d[A \cdot s \cdot (\phi - 1)]}{ds}$$

$$\text{Energy:} \qquad \frac{d[\phi \cdot u \cdot A \cdot h]_{jet}}{ds} = \frac{\pi}{2} \cdot C_{Ent} \cdot d_{jet}(s) \cdot u_{Gas_{jet}} \cdot h_{Gas(P_{ambient})} \quad,$$

where c refers to the species concentration. ϕ is the ratio of the jet density to that of the ambient and approaches the value of unity with the nozzle downstream distance. The entrainment coefficient, C_{Ent}, is needed for the conservation laws of mass, momentum and energy equations to present the balance between the jet components and the air entrained from the ambient. Mass transfer within the gas free jet follows the same general trend as the momentum exchange. After establishing the jet flow, the radial distributions for the velocity, the density and the concentration are assumed to follow the Gaussian function in the fully developed region which can be written as

$$u_{Gas_{jet}}(s,\, r) = u_{Gas(P_{ambient})} + u_{jet_{centerline}}(s) \cdot \exp\left(-\ln 2 \left(\tfrac{r}{r_{0.5}}\right)^2\right)$$

$$\rho_{Gas_{jet}}(s,\, r) = \rho_{Air(P_{ambient})} + \rho_{jet_{centerline}}(s) \cdot \exp\left(-\ln 2 \left(\tfrac{r}{\lambda \cdot r_{0.5}}\right)^2\right)$$

$$c_{Gas_{jet}}(s,\, r) = c_{jet_{centerline}}(s) \cdot \exp\left(-\ln 2 \left(\tfrac{r}{\lambda \cdot r_{0.5}}\right)^2\right) \quad \text{with}$$

$$r_{0.5} = tan\beta_{0.5} \cdot (s - s_{virtual}) \quad \text{and} \quad C_{Ent} = tan\beta_{0.5} \quad,$$

where $r_{0.5}$ is the jet width that corresponds to the half way point of the maximum velocity. The entrainment coefficient is, by convention, determined from the spreading angle of the gas

free jet, while λ parameter is the turbulent Schmidt number defined by the ratio of the width of the density or the concentration profile to the width of the velocity profile. In literature, the turbulent Schmidt is given a value in the range of 1 to 1.35. Tab. 2 summarizes typical values for the turbulent Schmidt number.

Model	Turbulent Schmidt number
Chiang et al. [12]	1.0
Morton et al. [72]	1.0
Hirst [36]	1.16
Ooms [76]	1.35

Tab. 2: Typical values for the turbulent Schmidt number

Chiang et al. [12] and Morton et al. [72] suggest a value of 1.0, while Hirst [36] proposes a value of 1.16 and Ooms [76], however, states a value of 1.35. In summary, these models are stating constant values for the turbulent Schmidt number which are needed for the prediction of the species concentration in the jet flow. Species concentration may also be subject to change with the downstream distance due to the distinct difference in the physical properties between the dense single-phase dispersion flow and the ambient. In this context, the main features in the case of a liquid free jet are presented in the following section.

2.1.2 Liquid free jet flow

Experimental studies on liquid jets performed by Faeth et al. [22], Hsiang et al. [38], Mayer et al. [66], O'Neill et al. [75], Varga et al. [103], Vandroux et al. [102], Wheatly [109] and Wierzba [111] describe the conceptual aspects of such dispersion flow kinds. The main subject of each study is the breakup of liquid bulk which is attributed to the disturbances at the liquid surface induced by the shear forces exerted by the surrounding fluid. The difference in velocity of the liquid jet and the ambient provides the potential for the formation of a non-uniform distribution of droplet sizes due to non-linear surface instabilities. The most important and influential parameters on the liquid phase breakup are the liquid physical properties as well the inertial forces.

Analogous to the gas dispersion flow, the liquid free jet spreads downstream and the mean jet velocity gradually decreases. The velocity decay with the downstream distance is attributed to the air entrainment. Walter et al. [105] and Wygnanski et al. [115] state that the turbulence, presented by the fluctuating jet velocity, and the entrainment phenomena are combined by the velocity ratio as

$$\frac{u_{Air(P_{ambient})}}{u_{jet}} = f_1(\frac{r}{r_{0.5}}) \quad , \quad \frac{\acute{u_{jet}}^2}{u_{jet}^2} = f_2(\frac{r}{r_{0.5}})$$

Accordingly, u_{jet} and $\acute{u}_{jet}$ are the mean and the fluctuating jet velocity. f_1 and f_2 are, by convention, Gaussian functions related to the spatial distance. Consequently, the turbulent jet velocity achieves a self-preserving state after a further downstream distance. Approaching an asymptotic downstream value for the mean velocity and its fluctuation has been investigated for both constant density jets, e.g., by Wygnanski et al. [115] and variable density turbulent jets by Birch et al. [4]. This value is consistent with the general simplification of the energy transport from the turbulent jet flow to the ambient. The transfer of the jet turbulent energy to the ambient is substantially responsible for the velocity decay in the downstream direction, which is relatively high close to the jet near field region. Further downstream, the mean velocity gradients decrease and, hence, the turbulent energy is balanced by the losses due to the viscous dissipation and redistribution of the turbulent energy to the radial flow direction. The so called turbulence intensity approaches an asymptotic downstream value due to the balance between the production and the loss terms.

A comparison between the centerline and radial velocity gradients made by Sirignano [93] shows that the radial gradients increase less rapidly than those of the centerline velocity in the jet near field region. The results were explained in terms of a stepwise mechanism of the turbulent energy transfer in which the momentum is transferred directly from the mean jet flow to the ambient. Subsequently, the energy transfer is partially consumed by the liquid disintegration process and the redistribution of the droplet velocity in the radial direction normal to the mean jet flow. Within the Core region of the liquid free jet flow, the interactions between the air and the liquid phase are becoming significant, leading to the formation of the surface instabilities that grow in magnitude and, hence, enhancing the breakup of the liquid bulk to fragments. In the following section, the jet breakup length will be addressed.

Jet breakup length

The jet extension from the source to the downstream distance, where the liquid bulk is completely disintegrated into droplets is, by tradition, presumed as the jet breakup length. It is strongly related to the physical properties of the liquid phase as well as the upstream flow conditions. Fig. 3 depicts the three main patterns for the liquid jet breakup as a function of the nozzle outlet velocity according to Bayvel [3], Czerwonatis [17] and Rayleigh [82]. At low nozzle velocities, primary individual droplets with sizes in the same order of magnitude of the nozzle diameter are periodically formed under the capillary pinching effects, while the influence of the aerodynamic forces due to motion of the ambient air over the liquid surface are negligible. This corresponds to the jet breakup characterized by Single droplet formation (Rayleigh).

Obviously an increase in the nozzle outlet velocity causes the jet breakup length to increase approaching a maximum. Behind the maximum point increasing the nozzle outlet velocity would result in a decrease in the jet breakup length. Herewith, the aerodynamic forces grow in magnitude to build axisymmetric capillary waves that dominate the surface tension forces and break up the liquid bulk into fragments. This is described by the String formation pattern. At increased nozzle outlet velocity, the aerodynamic forces have the most significant influence on the liquid breakup. The atomization pattern will be established leading to the complete disintegration of the liquid bulk into droplets, within a relatively shorter downstream distance compared to that of the two above mentioned patterns of the liquid jet breakup. The primary droplets are, thus, much smaller due to the intensive interactions between the liquid bulk and the entrained air from the ambient.
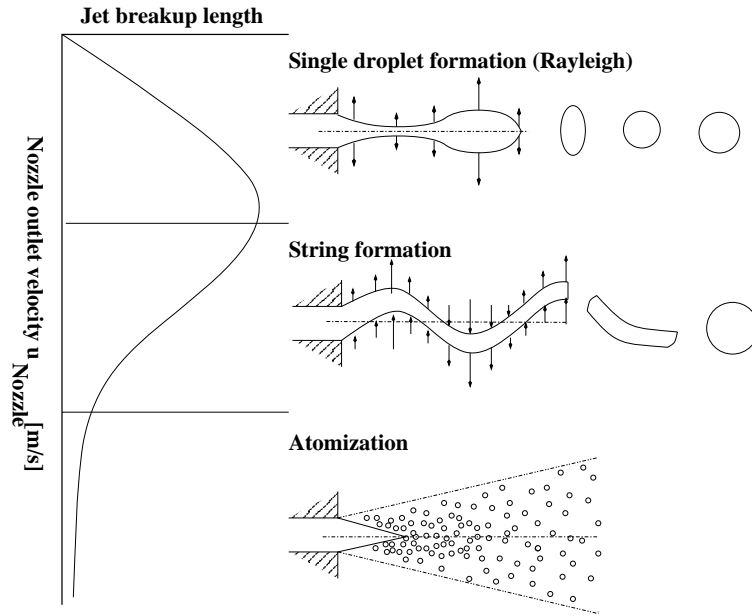
Fig. 3: Liquid jet breakup patterns as a function of nozzle velocity according to Bayvel [3], Czerwonatis [17] and Rayleigh [82]

For the assessment of the breakup length of the liquid jet under the impact of the aerodynamic forces, the predictive equation for the jet breakup length according to Reitz et al. [83, 84] reads

$$L_{Aero} = 2.75 \cdot 10^{10} \cdot d_{Nozzle} \cdot \frac{\sqrt{We_{Nozzle}}}{Re_{Nozzle}^2} \quad , \quad Re_{Nozzle} > 4.8 \cdot 10^4 \quad \text{and} \quad 10 < We_{Nozzle} < 50$$

The breakup correlation includes the terms of the nozzle diameter, Reynolds number and Weber number defined as

$$Re_{Nozzle} = \frac{u_{Nozzle} \cdot d_{Nozzle} \cdot \rho_{Liq}}{\eta_{Liq}} \quad \text{and} \quad We_{Nozzle} = \frac{u_{Nozzle}^2 \cdot d_{Nozzle} \cdot \rho_{Air(P_{ambient})}}{\sigma}$$

11

The Reynolds number is defined by the ratio of the liquid inertia to the viscous forces, while the Weber number accounts for the competition between the inertial and the surface tension forces. This model is applicable for estimating the jet breakup length in case of free jet flow of liquid phase with physical properties close to those of water. The Reynolds number and Weber number range imply that the inertial forces have a significant effect on the generation droplets from the liquid bulk with different size distribution. In this domain, the droplet size spectrum will be discussed in the next section.

Droplet size spectrum

Generally, the modelling of the free jet relies heavily on droplet size spectrum. It can be summarized that the droplet size distribution is basically affected by the velocity gradients in the downstream and radial directions. The velocity gradients are responsible for the instabilities at interface due to the intensive interactions between the air stream and the liquid bulk. In dispersion flows, the droplets are formed with different size classes. So it would be more appropriate to consider a characteristic droplet diameter that represents the droplet size distribution of the free jet flow. For this purpose, the Sauter droplet diameter is most convenient and is presented next.

Sauter droplet diameter

This characteristic droplet diameter is traditionally considered for the efficiency aspects in the industrial applications. It is defined as

$$d_{Sauter} = d_{32} = \frac{\sum n_{droplet} \cdot d_{droplet}^3}{\sum n_{droplet} \cdot d_{droplet}^2} \qquad ,$$

where $n_{droplet}$ is the number of the droplets with a certain size class of $d_{droplet}$. Based on this expression, the Sauter mean diameter is accessible through dedicated experiments. A relatively larger Sauter droplet diameter indicates, in this context, larger droplets and/ or a wider droplet spectrum. Another convenient diameter definition, that is of great interest in industrial applications, is the maximum stable droplet diameter. It will be presented in the following section.

Maximum stable droplet diameter

Breakup occurs when the linear cohesive forces are less than the local external shear forces exerted by the ambient. The non-dimensional Weber number [108] is used to characterize these competing forces. The Weber number is defined by the ratio of the inertial to the surface tension forces as

$$We = \frac{\rho_{Air(P_{ambient})} \cdot u_{rel}^2 \cdot d_{droplet}}{\sigma} \quad \text{with} \quad u_{rel} = u_{Air_{jet}} - u_{droplet} \quad ,$$

where u_{rel} is the initial local velocity difference between the air and the droplet. It implicitly accounts for the course of acceleration. For the calculation of Weber number, the mean velocities of the air as well as the deformed droplets are needed. Droplet breakup occurs when the local shear exerted by an eddy is larger than the surface tension forces. Generally, the critical Weber number, a quantity representing the minimum force or energy required to cause the disintegration of the liquid droplet, is utilized as criterion to calculate the maximum stable droplet diameter. It is defined as

$$We_{crit} = \rho_{Air(P_{ambient})} \cdot (u_{Air_{jet}} - u_{droplet})^2 \cdot d_{max}/\sigma \quad ,$$

$$d_{max} = We_{crit} \cdot \sigma/(\rho_{(P_{ambient})} \cdot (u_{Air_{jet}} - u_{droplet})^2) \quad \text{with} \quad 12 < We_{crit} < 25$$

The critical Weber number varies according to the changes made to the flow conditions. Typical values for the critical Weber number are in the range between 12 as was proposed by Iannello et al. [40] or Pilch et al. [78] and 25 according to Woodward [114]. The droplet breakup mechanisms are illustrated in the next section.

Droplet breakup mechanisms

The breakup of liquid droplets in a turbulent air stream is attributed to disturbances at the liquid surface induced by shear forces. In detail, two kinds of disturbances cause the droplet breakup, i.e., shock wave disturbances that are pronounced by the steep changes in the turbulence intensity of the ambient and steady disturbances enhanced in the Similarity region. These disturbances induce waves on the liquid phase surface with amplitudes, that have a magnitude of several times the mean film thickness between air and liquid phase, and travel with a velocity greater than that of the film. A close examination of the process of droplet generation indicates that droplets are not created from the entire film interface, but very specifically as they arise from these disturbance waves. The size classes of the formed droplet from the liquid bulk disintegration result from the magnitude and the intensity of the waves established at the surface. Blaisot [5] and Bousfield et al. [6] state that the size of the primary droplets strongly depends on the wave number of the instability. It was reported that the instability causing the jet breakup changed from axisymmetrical to non-axisymmetrical with increasing flow rate and changing liquid physical properties.

Once a droplet has been entrained by the air flow, it can break up according to the main mechanisms that occur in the range of the flow conditions of the specific free jet experiments. The classification of the breakup mechanisms is entirely based on the observations made in gas

13

flow fields. According to Dhainaut [19] and Pilch et al. [78], bag breakup occurs at low gas and liquid flow rates with a critical Weber number between 12 and 50, see Fig. 4(a). A part of the disturbance wave is undercut and an open-ended droplet is formed with a thick filament rim. Gas pressure builds up within the droplet causing it to expand and eventually to burst. This produces a number of small droplets while the rim breaks up shortly afterwards giving a large number of smaller droplets. At higher flow rates corresponding to a Weber number between 50 and 100, ligament breakup occurs, in which the crests of roll waves are elongated and thin ligaments are torn off from the film, see Fig. 4(b). These ligaments immediately break up into droplets. Further breakup mechanisms are sheet stripping ($100 \leq We \leq 350$), wave crest stripping ($We \geq 350$) and catastrophic breakup with the Weber number in excess of 350. These occur in a range of flow conditions which is outside the sphere of interest.

(a) Bag breakup mechanism

(b) Ligament breakup mechanism
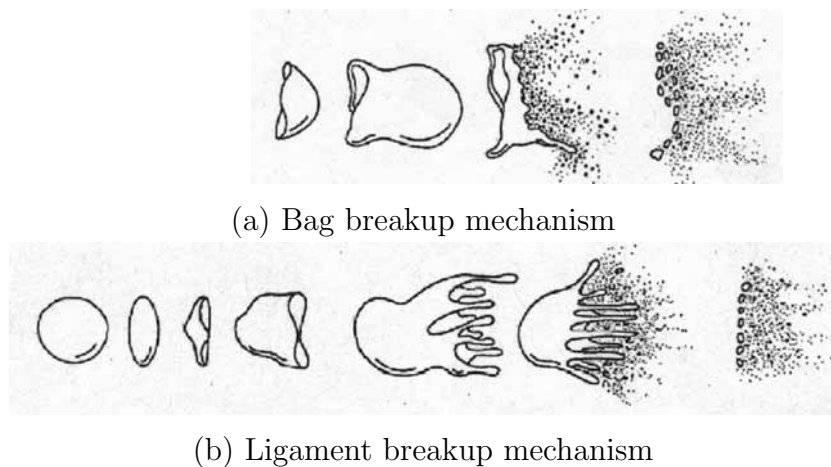
Fig. 4: Droplet breakup mechanisms in a gas stream according to Dhainaut [19] and Pilch et al. [78]

The droplets generated from liquid phase breakup are subject to collisions in the downstream distance. These collisions often lead to coalescence, provided that the droplets remain in contact for a period of time sufficient for the liquid film in between to thin to a critical value necessary for rupture. In the next section, droplet collision is reviewed.

Droplet collision

The contact time between the surfaces of two colliding droplets depends on the droplet size class and the turbulence intensity of the surrounding. Larger droplets with higher inertia provide a longer contact time and increase the likelihood of droplet coalescence. While a higher level of turbulence increases the probability that an eddy will separate the droplets. On the basis of a Collision Weber number and an impact parameter as controlling factors for the different outcomes, Qian et al. [80] and Ko et al. [47] produced a map for the identification of the collision regimes and the post-characteristics of droplet collisions. The relevant expressions read

$$We_{Collision} = \rho_{Air(P_{ambient})} \cdot (u_{Air_{jet}} - u_{droplet})^2 \cdot d_{ref}/\sigma \quad \text{and}$$

$$b = 2 \cdot B/(d_1 + d_2) \quad \text{with} \quad B = 2 \cdot \sin\theta/(d_1 + d_2) \quad ,$$

where $We_{Collision}$ is the collision Weber number while d_{ref} is the reference diameter for the two colliding droplets. The collision Weber number is again calculated based on the carrier gas density, the relative velocity as the difference in the linear velocity between that of the gas and the droplet, and a specific reference droplet diameter. In the original references by Qian et al. [80] and Ko et al. [47], the droplet diameter is based on the average size of the colliding droplets, while the diameter of the smaller colliding droplet was considered in others according to Kollár et al. [49].

Basically, the prediction of the reference droplet diameter and droplet velocity are based on theoretical approaches supported by experimental evidences, applying mass and momentum equations before and after the droplet collisions had taken place. Whilst the impact parameter, b, is defined by the dimensionless perpendicular distance between the relative velocity vector located at the center of one droplet with respect to the spatial distance of the summation of the radii of both droplets, see Fig. 5, B is the perpendicular distance between the vectors of two droplet trajectories.
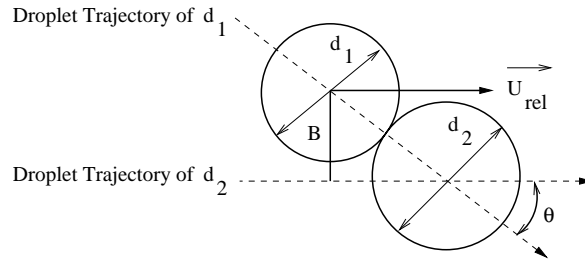
Fig. 5: Characteristic parameters of droplet collision model

The underlying collision regimes in Fig. 6 can be illustrated as follows. As two droplets are approaching each other, the gas inside the gap is trapped building up a gas pressure. If the kinetic energy of the droplets, indicated by their relative velocity, is not large enough to overcome the gas pressure force, they do not coalesce but separate from each other. This is referred to Bouncing (regime I). For the case of higher relative velocity, resp., Weber number, one droplet comes in direct with the another and, in turn, permanent Coalescence (regime II) occurs as an outcome of the collision between them. At higher Weber numbers, the droplets dispose of excess kinetic energy, which leads to the separation of droplets coalesced tentatively, which frequently goes along with the simultaneous production of relatively smaller droplets.

Reflexive Separation (regime III) would occur when the effective reflexive kinetic energy exceeds about 75% of the surface energy of the two droplets coalescing temporarily. This arbitrarily chosen percentage value was introduced to consider the deformation effect of the colliding droplets. Stretching Separation (regime IV) would take place when the effective stretching energy exceeds the surface tension energy of the two colliding droplets. The temporarily coalesced droplets tend to undergo a Reflexive and a Stretching Separation, resp., at low and high impact parameters. Thus, $b = 0$ and 1 designate head-on, resp., grazing collisions [80]. Indeed, the other collision outcomes, such as Bouncing, Stretching and Reflexive Separation are possible, but are excluded here.
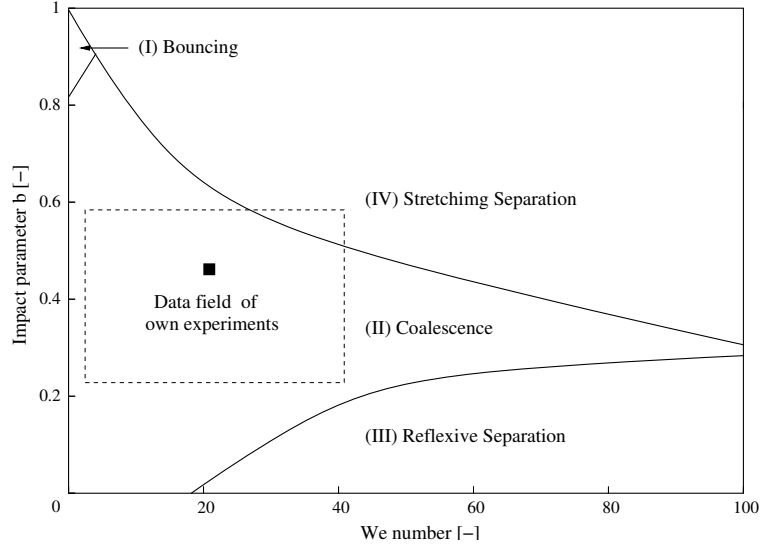
Fig. 6: Boundaries between collision regimes according to Ko et al. [47]

In anticipation of the experimental results to be described later on, the data field of current test conditions is characterized mainly in region II and partially in IV. In detail, droplet diameters in the range of 100 - 200 μm were considered for the experiments, with droplet collisions carried out under different flow conditions and liquid physical properties. The boundary curves between the regimes of the corresponding outcomes are subsequently introduced according to Kollár et al. [49] as dimensionless figures.

Stretching Separation and Coalescence

The criterion for Stretching Separation implies that

$$We_{Collision} > \frac{4.8}{b^2} \cdot \frac{[1 + \gamma^2 - (1 + \gamma^3)^{2/3}] \cdot (1 + \gamma^3)^{11/3}}{\gamma^6 \cdot (1 + \gamma)^2} \quad \text{with} \quad \gamma = 1/\Delta \quad \text{and} \quad \Delta = \frac{d_1}{d_2}$$

The velocity of each droplet after Stretching Separation is calculated as follows

$$U^{new} = \frac{U_1 d_1^3 + U_2 d_2^3 + (U_1 - U_2) \cdot d_2^3 \cdot Z}{d_1^3 + d_2^3} \quad \text{with} \quad Z = \frac{b - b_{crit}}{1 - b_{crit}} \quad \text{and} \quad b = \frac{2 \cdot B}{d_1 + d_2}$$

Here, b_{crit} is the critical impact parameter in excess of which the collision results in Stretching Separation and below of which the Coalescence is permanent. It can be calculated according to

$$b_{crit} = \min \left(1.0, \frac{4.8}{We_{Collision}} \cdot \sqrt{\frac{[1 + \gamma^2 - (1 + \gamma^3)^{2/3}] \cdot (1 + \gamma^3)^{11/3}}{\gamma^6 \cdot (1 + \gamma)^2}} \right)$$

Reflexive Separation and Coalescence

The condition for the Reflexive Separation can be expressed by

$$We_{Collision} > 3 \cdot (7 \cdot (1 + \Delta^3)^{2/3} - 4 \cdot (1 + \Delta^2)) \cdot \frac{\Delta \cdot (1 + \Delta^3)^2}{\Delta^6 \cdot \zeta_1 + \zeta_2}$$

with $\quad \zeta_1 = 2 \cdot (1 - \xi)^2 \cdot (1 - \xi^2)^{1/2} - 1 \quad , \quad \zeta_2 = 2 \cdot (\Delta - \xi)^2 \cdot (\Delta^2 - \xi^2)^{1/2} - \Delta^3 \quad$ and $\quad \xi = \frac{b}{2} \cdot (1 + \Delta)$

On resuming the definition of the Collision Weber number, the reference droplet diameter was specified based on the summation of both radii of the colliding droplets

$$d_{ref} = \frac{d_1 + d_2}{2}$$

In Fig. 5, the situation of two droplets that are spatially in contact is presented, the impact parameter, b, can be reformulated by

$$b = 2 \cdot \sin \theta \quad \text{with} \quad \sin \theta = B/(d_1 + d_2) \quad ,$$

where θ is the inclination angle between the two vectors of the droplet trajectories, while the parameter B is determined by the perpendicular distance between the trajectory of the first droplet and the vector of the relative velocity located at the center of the second droplet. Indeed, the authors have not proposed a method for the prediction of the reference droplet diameter. Here, the reference diameter was taken as the Sauter droplet diameter obtained from Phase Doppler Anemometer measurements. It is found that the Sauter diameter is merely adequate for the calculation of the droplet collisions. However, a predictive method can not also be presented. In the macroscopic dimensions, the vortical air structures appeal intensive interactions with the liquid bulk producing droplets. In parallel, the progressive collisions between droplets have also an influence on the establishment of the droplet velocity distribution with the downstream distance. This topic is presented with more details in the next section.

Droplet velocity distribution

By tradition, the droplet velocity distribution in the free jet flow is given the expression following the Top-hat or the self-establishing Gaussian profiles. The Top-hat or the so called Rectangular profile is derived with the simplification of a momentum conservation along the direction normal to the jet plane. This model states a value of the droplet velocity similar or equal to that at the jet centerline with the nozzle downstream distance. Herewith, the total jet momentum is calculated based on the individual momentum of the liquid phase and the air flow. As an example from the literature, the model by Görtler [27] suggests the rectangular profile for the local droplet velocity and reads

$$u(s,r) = u_{jet}(s) \left[1 + 57.76 \cdot \left(\frac{r}{s} \right)^{-2} \right] \quad \text{with}$$

$$u_{jet}(s) = \frac{7.4}{s} \sqrt{\frac{J}{\rho_{Nozzle}}} \quad \text{and} \quad J = \dot{M}_{Liq} \cdot u_{Nozzle} \quad ,$$

where J is the jet momentum and $\dot{M}_{Liq}$ is the liquid mass flow rate. It was deduced that the jet momentum is balanced at any downstream location with the jet source due to the momentum transfer from the liquid jet to the ambient. It appears here that the nozzle flow conditions are required for the calculation of the local droplet velocity. On the other hand, the Gaussian or the so called bell-shaped profile describes the dispersion flow from a nozzle of circular outlet. The Gaussian profile suggests a maximum value of the droplet velocity that is locating theoretically on the jet centerline. In the direction towards the jet periphery, the droplet velocity decreases to establish - on average - a value corresponding to the surrounding state. The Gaussian profile, applied by Schlünder [91] to predict the droplet velocity decay, reads

$$u(s,r) = u_{Nozzle} \cdot \sqrt{1 - exp\left(-48 \left(\frac{d_{Nozzle}}{s} \right)^2 \right)} \cdot \sqrt{exp\left(-193 \left(\frac{r}{s} \right)^2 \right)}$$

It is worthwhile to note that the fitting parameters in the model by Schlünder [91] are subject to change, with respect to the release state under sub- or critical flow conditions, in order to increase the model predictions. As a result, it can be deduced that the release conditions involve phenomena that affect the droplet velocity distribution, which must be considered for improving the predictions of the theoretical model.

The associated phenomena within the free jet flow, established from the dispersion of two-phases, rely on the release flow direction. Probable horizontal, vertical or inclined directions may occur in real industrial dispersions. For ecological as well environmental concerns, the release devices, e.g. safety valves or relief nozzles, are mounted to allow for the establishment

of a horizontal dispersion flow. In considering the advantages of the possible collection of the dispersion flow content, hence, the spreading of this hazard to the surrounding would be better prevented than in the case of vertical or inclined dispersion flows. For this reason, the characteristics of two-phase dispersion flows in the horizontal direction will be considered. Two-phase gas/ liquid free jet flow is presented next.

2.2   Two-phase gas/ liquid free jet flow

The behavior of two-phase gas/ liquid free jet flow is characterized in the momentum dominated regime, to a great extent, by the outlet conditions and particularly the existence of two-phases in the flow system. When two-phase flow passes through a pipe, the system potentially shows a phenomenological behavior that arbitrarily differs in comparison to that of single-phase flow under identical flow conditions. This is attributed to the interactions between both phases, governed by the flow conditions and the fluid properties. By studying a simultaneous flow of gas/ liquid in a horizontal pipe the mean superficial velocity, by convention a characteristic parameter denotes the volume rate density of each phase, is implemented to characterize the establishing flow patterns. The superficial liquid velocity is plotted as a function of the superficial gas velocity for a horizontal two-phase gas/ liquid pipe flow in Fig. 7.
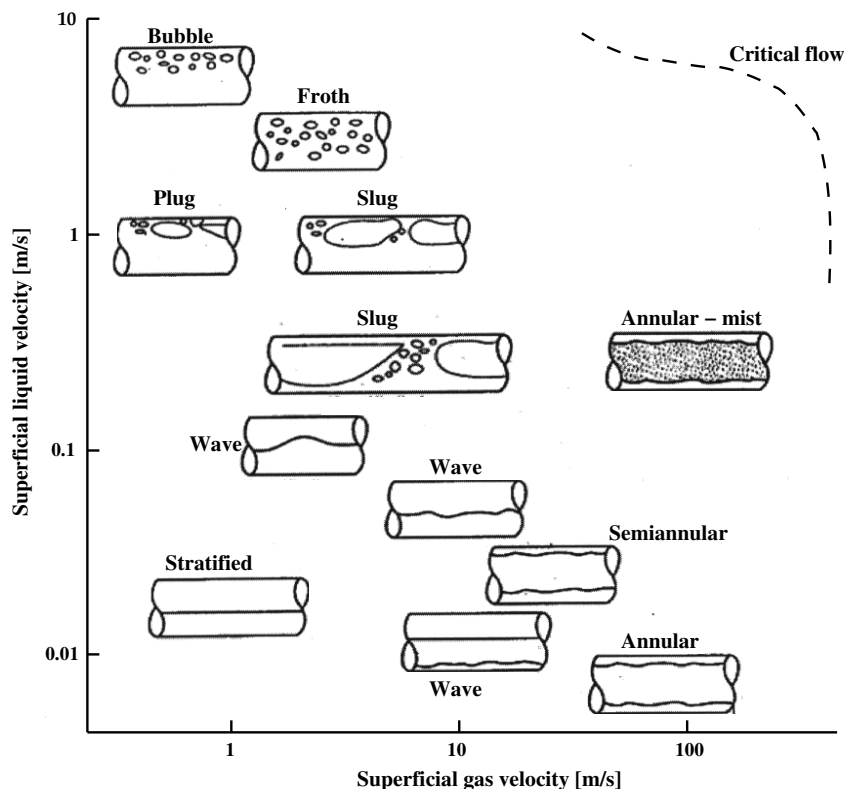
Fig. 7: Flow patterns for a horizontal two-phase gas/ liquid pipe flow corresponding to Mandhane et al. [64]

19

At low flow velocities, both phases will form a stratified liquid film at the interface presented at the lower left hand corner. The gas occupies the upper part of the flow due to the relative lower density. As either the liquid flow rate or the gas flow rate is raised, the film becomes prone to the flow perturbations exerted by the gas flow leading to create a wave at the interface and, hence, will be disturbing the interface to establish the Wave flow. With further increases in the liquid flow rate, the waves grow in amplitude to touch the upper wall of the pipe, thereby, destroy the continuity of the gas phase flow. This is called the Plug or the Slug flow. The former term is characterized by the more gentle action, where the gas bubble moves forward without intense agitation. The latter is expressing the more violent action observed when increasing the gas flow rate. As the liquid flow rate is further increased, the gas bubbles are broken up into rather small ones. The flow may then be described as Bubble or Froth flow, according to whether the gas volume fraction is small, resp., high.

If the gas flow rate is increased at a relatively low liquid flow rate, a phase transition is observed for the above-mentioned patterns, which in turn increases the likelihood of coalescence in case of bubble collisions. A regime with both continuous gas and liquid phases is reestablished, this time the gas occupies the core surrounded by a predominantly liquid annular film. Under these conditions there is usually some gas dispersed as bubbles in the liquid and some liquid dispersed as droplets in the gas stream. The flow is then called Annular or Semiannular. However, the liquid may wet the entire wall surface establishing the Annular - mist flow when rising the liquid flow rate at relatively high gas flow rates. At very high flow rates of both phases, a critical flow phenomenon is approached, where it is then impossible to recognize a flow pattern established at rates beyond those indicated by the dashed border.

Other significant phenomena associated with two-phase gas/ liquid flow are the surface instabilities at the gas-liquid interface. For illustration, both instability patterns are depicted in Fig. 8.
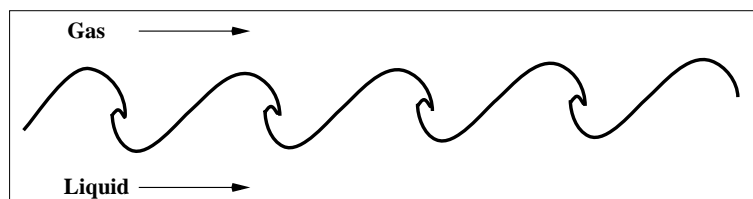
(a) Kelvin-Helmholtz instability
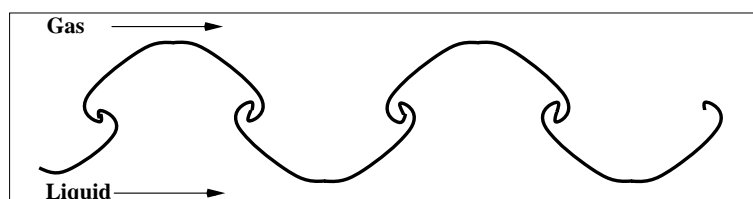
(b) Rayleigh-Taylor instability

Fig. 8: Instability patterns on the liquid surface due to the co-flowing gas stream according to Dhainaut [19] and Hewitt et al. [34]

The first scroll pattern is called the Kelvin-Helmholtz instability. When two fluids are flowing adjacent to each other, the film creates scroll waves causing a local drop in the liquid level that may develop to the formation of a gas pocket due to the effect of gravity. The second scroll pattern is the Rayleigh-Taylor instability. It takes place when massively dynamic interactions between the two fluids are generating pressure waves under the conditions, where a dense fluid being accelerated by the lighter one in the flow direction normal to the interface plane. Kelvin-Helmholtz instability can not be a sufficient condition for the liquid disintegration of a stratified liquid film, since it does not account for the efficient transfer of momentum from the gas stream to the liquid bulk. Admittedly, the liquid bulk disintegration occurs in the pipe flow and, hence, the generated droplets will be entrained by the gas stream.

Experiments on droplet entrainment in a gas flow indicate that there are, in general, three basic types of entrainment mechanisms in the stratified film according to Ishii et al. [42], Fig. 9.
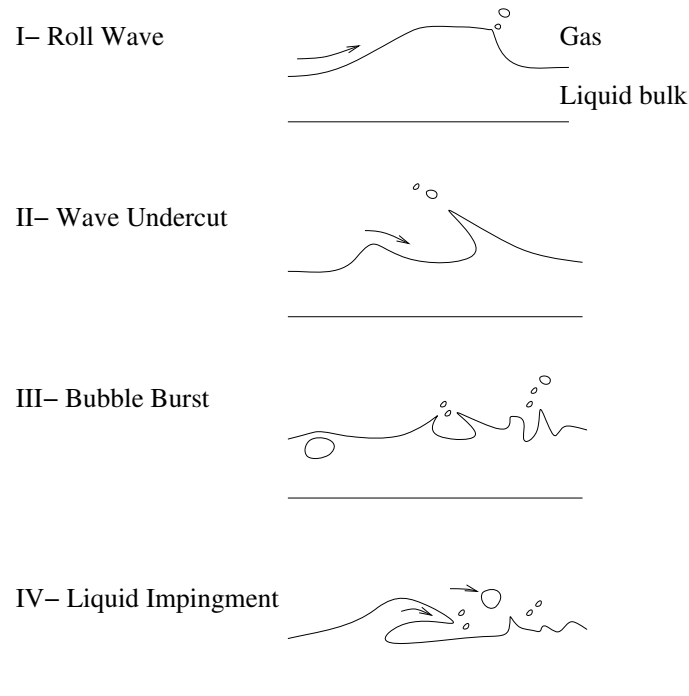
Fig. 9: Types of droplet entrainment mechanisms in a stratified film flow in a pipe according to Ishii et al. [42]

In the annular flow pattern such mechanisms may, under certain conditions, lead to an extreme deformation of the interface which result in breakup of the liquid bulk into droplets to be entrained by the gas stream. The first type of droplet entrainment mechanism is the so called Roll Wave, where the crests of large amplitude roll waves are sheared off by the gas flow. When the drag force, acting on the wave tops, deforms the interface and overcomes the retaining force, this type of entrainment is then called the Wave Undercut. It takes place where also a significant slip exists between the mean velocities of both phases causing a relatively higher

shear force exerted by the gas flow. This eventually leads to the submergence of the gas into the liquid surface and thinning of the interface boundary layer. The third type of entrainment is the Bubble Burst. The bubble does not break through immediately upon reaching the liquid surface. Instead, it undergoes an oscillatory motion until the instability overcomes the surface tension force at the liquid interface. In the course of the break through of the bubble, the liquid drains a part of the gas bubble to form a dome. The bubble dome then bursts to very small droplets and establishes a well-defined gap at the interface. The momentum of the in-flowing liquid to refill the gap is relatively high, establishing a mini liquid free jet with a high flow velocity. Afterward, the top of this liquid jet detaches and generates additional droplets. As confirmed by Grolmes et al. [28], McKeogh et al. [68], Piesche et al. [77], Reitz et al. [83] or Snyder et al. [94], an additional droplet entrainment type due to the dynamics of the liquid mass at the interface may be established and is described as Liquid Impingement. It is characterized by the formation of a large amplitude wave that may be separated from the liquid at the interface or may even form a liquid bridge connecting another preceding wave. Consequently, a liquid bulge impinges its surface enhancing the interface instabilities and then segregating the liquid bulk into droplets.

The assumptions used in the description of the single-phase free jet flow characteristics and velocity profiles are, by convention, also taken in the literature to be valid in the case of a two-phase gas/ liquid free jet into a quiescent ambient with equal or lower pressure. The flow patterns in the nozzle may be a homogeneous bubble, a slug or rather an annular flow with a Gas core as often observed in reality, Fig. 10.
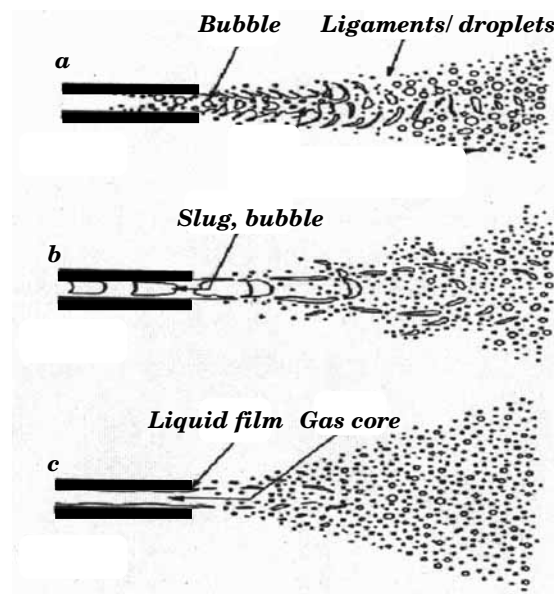
Fig. 10: Flow patterns of the two-phase free jet as a function of the upstream flow condition according to Lörcher [60] and Witlox et al. [112]

Downstream from the nozzle, various modes of atomization prevail depending on the flow conditions at the nozzle aperture, e.g., the formation of tree-like jets has been observed under annular flow conditions. The bubble, slug and mist flow patterns are obviously not considered further due to the lack of interest in the industry. In Fig. 11, the characteristics of the momentum dominated two-phase gas (here air)/ liquid free jet flow, when the nozzle outlet pressure is higher than that of the stagnant ambient air, are depicted. The air/ liquid stream disperses with an assumed mean outlet velocity of u_{Nozzle}. The mean outlet velocity is generally calculated on the basis of one-dimensional homogeneous flow model, although in the nozzle a bubble, annular or mist flow pattern may prevail.
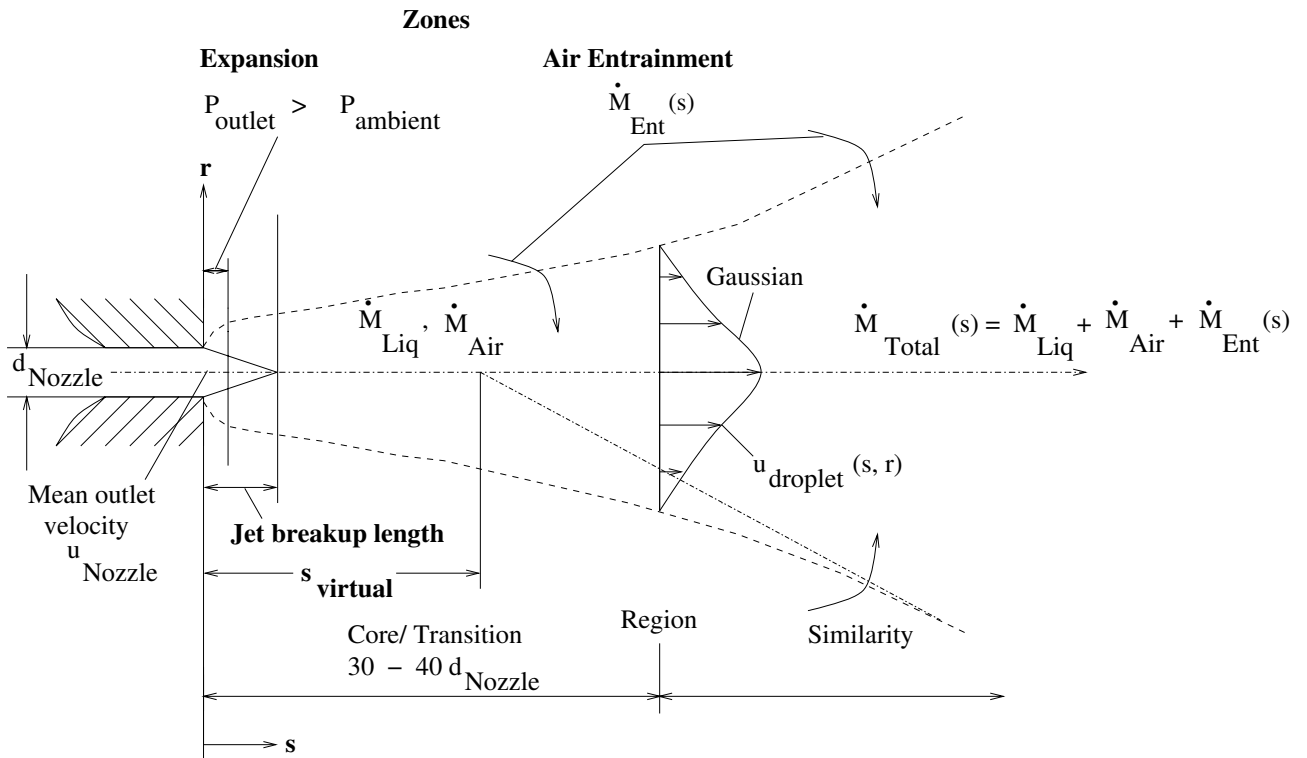
Fig. 11: Characteristics of a momentum dominated two-phase free jet flow in stagnant ambient air with lower pressure (nozzle downstream dimensions are underscaled)

Whatsoever, the two-phase jet flow is characterized in the axial direction by the formation of only two distinct flow regions. The Core / Transition region, which dilates up to a downstream distance of thirty to forty nozzle outlet diameters, now includes the jet breakup length. A portion of the jet breakup length is formed by the Expansion Zone, the outlet pressure is higher than the ambient pressure, whereby the flow fluctuations are supposed to become established on the jet boundaries but no air entrainment is expected to take place in view of the macroscopic radial and axial expansion of the air, in the latter mentioned case, with the velocity $u_{expansion_{Air}}$. Consequently, the turbulence intensity within the Expansion Zone is high, so that

already a significant impact on the liquid bulk, that is the droplets, takes place. These large scale interactions between both phases - induced by the air flow expansion - promote a primary breakup of the liquid to droplets, in case of annular flow that may (here) occur initially in the two-phase nozzle flow. Within the jet breakup length, the continuous liquid phase stream entirely disintegrates into individual fragments, i.e., droplets are entrained by the ambient air, leading to an increase in the jet perimeter in the Core/ Transition region.

The subsequent Similarity region is characterized by the entrainment of the ambient air. The free jet flow now establishes, ideally, symmetric self-similar droplet and air velocity profiles. The turbulence intensity, i.e., ratio of the turbulent velocity, that is, the root mean square droplet velocity with respect to the mean centerline velocity and, hence the flow fluctuations, are expected to reach a self-preserving state. Indeed, the air stream impact on the liquid droplets is still significant, leading to further downstream disintegration of the droplets, the so called secondary breakup in the dispersing jet flow. Since the entrainment process is continual, in total, an overproportional deceleration of the jet is imposed with downstream distance or the mass flow quality of the jet. The liquid viscosity influences the primary droplet size and deformation, and further downstream, the secondary breakup by the fact that now in relation higher shear stresses continuously act at the liquid surface, comprising competition between the disruptive and the adhesive or conservation forces for each particular droplet along with the downstream distance.

On resuming the flow patterns of a two-phase nozzle flow, it is difficult to calculate the mean flow velocity as well the two-phase density and viscosity. For this purpose, methods for quantitative calculation of the two-phase flow parameters are developed, in comparison to those of a single-phase flow from some empirical correlations, to connect the two-phases with significantly different properties. In the next section, the definitions of the most relevant parameters for a two-phase flow will be presented.

2.3   Definitions

Considering a two-phase flow system of air and the liquid inside a control volume with a circular cross sectional area under isothermal flow conditions, the most important definition is the dimensionless mass flow quality. It reads

$$\dot{x}_{Air} = \frac{\dot{M}_{Air}}{\dot{M}_{Total}} = \frac{\dot{M}_{Air}}{\dot{M}_{Air} + \dot{M}_{Liq}} \qquad \text{and} \qquad 1 - \dot{x}_{Air} = \frac{\dot{M}_{Liq}}{\dot{M}_{Air} + \dot{M}_{Liq}} \quad ,$$

where $\dot{x}_{Air}$ is the air mass flow quality. $\dot{M}_{Air}$, $\dot{M}_{Liq}$ and $\dot{M}_{Total}$ are the mass fluxes for the air, the liquid phase and the total flow rate of both phases. The so called mean void fraction is used for the determination of the pressure drop along the pipe as well for the heat and mass

balance and the momentum exchange. It is a self-adjusting parameter and is dependent on the volume of both phases. Under stagnant conditions, it is defined as

$$\epsilon = \frac{V_{Air}}{V_{Air} + V_{Liq}} \qquad \text{and} \qquad 1 - \epsilon = \frac{V_{Liq}}{V_{Air} + V_{Liq}} \quad,$$

whereby V_{Air} and V_{Liq} are the volumes for the air and the liquid phase. In the literature, several models, describing the void fraction for air/ liquid system, differ in the physical boundaries and the assumptions they rely on. The correlation proposed by Rouhani [87] for the application in case of horizontal, inclined and vertical oriented flow is recommended for the calculations of the void fraction and reads

$$\epsilon = \frac{\dot{x}_{Air}}{\rho_{Air}} \bigg/ \left(C_o \cdot \left(\frac{\dot{x}_{Air}}{\rho_{Air}} + \frac{(1 - \dot{x}_{Air})}{\rho_{Liq}} \right) + \frac{w_R}{\dot{m}_{Total}} \right) \quad \text{with} \quad C_o = 1 + 0.12 \cdot (1 - \dot{x}_{Air}) \quad,$$

$$w_R = 1.18 \cdot (1 - \dot{x}_{Air}) \left(\frac{g \cdot \sigma \cdot (\rho_{Liq} - \rho_{Air})}{\rho_{Liq}^2} \right)^{0.25} \quad \text{and} \quad \dot{m}_{Total} = \frac{\dot{M}_{Air} + \dot{M}_{Liq}}{A_{pipe}}$$

The correlation constant C_o describes the radial distribution parameter that characterizes the local mass flow quality and the velocity profile, while w_R refers to the velocity difference of the mean air flow to that of the two-phase flow. σ is the static surface tension against air. ρ_{Air} and ρ_{Liq} are the air and the liquid densities. $\dot{m}_{Total}$ is the total mass flow rate. The local and mean velocities of both phases must be considered with respect to the contribution of both phases. The mean or the linear velocity for each phase is defined according to

$$u_{Air} = \frac{\dot{M}_{Air}}{\rho_{Air} \cdot A_{pipe}} = \frac{\dot{x}_{Air} \cdot \dot{M}_{Total}}{\epsilon \cdot \rho_{Air} \cdot A_{pipe}} \qquad \text{and} \qquad u_{Liq} = \frac{(1 - \dot{x}_{Air}) \cdot \dot{M}_{Total}}{(1 - \epsilon) \cdot \rho_{Liq} \cdot A_{Pipe}}$$

The two phase flow pattern is determined by applying a characteristic velocity of the two phase flow. The so called superficial velocity, the volume flow rate of the air and the liquid through the whole cross sectional area of the pipe, reads

$$u_{i\,o} = \frac{\dot{V}_i}{A_{pipe}} \qquad \text{with} \qquad i = \text{Air, liquid}$$

For a detailed description of the flow patterns for horizontal as well vertical oriented two-phase an additional parameter, the slip ratio, is introduced. The slip ratio is defined as the ratio of the mean velocities of the air and the liquid phase. It attempts to account for the acceleration of the gas in relation to the liquid phase and is defined as

$$S = \frac{u_{Air}}{u_{Liq}} = \frac{\dot{x}_{Air}}{(1 - \dot{x}_{Air})} \cdot \frac{(1 - \epsilon)}{\epsilon} \cdot \frac{\rho_{Liq}}{\rho_{Air}}$$

In general, both phases will be accelerating and, hence, increasing their mean velocities, due to decreasing the stagnant pressure, to approach a value that is near to the speed of sound as the cross sectional area of the pipe is decreased, e.g., the flow through a nozzle. At this point the flow becomes choked and any further decrease in the stagnation pressure will not result in an increase in the total mass flow rate. In gas dynamics, this is called the critical flow and corresponds to the maximum nozzle release capacity. The modelling of the fluid dynamic critical flow is considered in the following section.

2.4 Modelling of fluid dynamic critical flow

The total mass flow rate from a nozzle, in addition to the air mass flow quality, is required for the calculation of the two-phase parameters. The homogenous equilibrium model enables a realistic prediction of the two-phase system properties. In the next section, it is briefly presented.

2.4.1 Homogeneous Equilibrium Model

This model implies an idealized case of isentropic two-phase flow through a nozzle oriented in the horizontal direction. Both phases are consistently distributed along the flow cross sectional area and, hence, both phases establish a uniform mean velocity, i.e., both phases are in kinetic as well as thermodynamic equilibrium. The energy balance applied between the point under the stagnation conditions and the nozzle outlet reads

$$h_{stagn} = h_{Nozzle} + \frac{u_{Nozzle}^2}{2} \qquad ,$$

where h_{stagn}, h_{Nozzle}, are the specific enthalpy of the two-phase flow at the stagnation and the outlet conditions. u_{Nozzle} is the mean nozzle outlet velocity. The outlet mass flow rate according to the homogeneous equilibrium model is determined as

$$\dot{m}_{hom} = \frac{\sqrt{2(h_{stagn} - h_{hom}(P_{outlet}))}}{\dot{x}_{Air}/\rho_{Air\,(P_{outlet})} + (1 - \dot{x}_{Air})/\rho_{Liq}} \qquad \text{and}$$

$$h_{hom}(P_{outlet}) = \dot{x}_{Air} \cdot h_{Air}(P_{outlet}) + (1 - \dot{x}_{Air}) \cdot h_{Liq}$$

In case of a subcritical flow, the outlet pressure corresponds to the ambient pressure. The slip ratio exhibits the value of unity for applying the Homogeneous Equilibrium Model. The existence of two-phases makes the homogeneous flow equations a near approximation under special

conditions of bubble, slug even annular flow. Consequently, the homogeneous flow model will be applied for the calculation of the two-phase parameters. For the evaluation of the model performance, the statistical numbers used for the characterization of the model reproductive accuracy will be presented in the next section.

2.5 Characterization of model reproductive accuracy

The predictions of a self-establishing quantity are normally compared against the experimental results to evaluate the model performance and generality. The predictions are, in addition, characterized by using statistical numbers, namely the absolute scatter and the logarithmic scatter. The definitions of these statistical numbers are

$$\text{Absolute scatter} \qquad S_{abs} = \pm \sqrt{\sum_{i=1}^{n} ln^2(Y_{iexp}/Y_{ipred})/(n-f-1)}$$

$$\text{Logarithmic scatter} \quad S_{ln} = exp\left(\sqrt{\sum_{i=1}^{n} ln^2(Y_{iexp}/Y_{ipred})/(n-f-1)}\right) - 1 \quad ,$$

where Y means the self-establishing experimental or the predicted quantity, while n is the number of the experimental data and f is the number of the correlation variables or so called degree of freedom. Basically, the lower the numbers the higher the predictive accuracy. The advantages of using these statistical numbers are to allow for a balanced description of the relative merits of each model in the whole region of experimental conditions.

In the next chapter, the related work will be reviewed.

3 Related work

Previous experimental and analytical trials performed on the dispersion of the two-phase air/ liquid free jet have been investigated. The experimental data in the literature describing the characteristics of two-phase free jet flow are introduced in the next section.

3.1 Experimental data in the literature

The mathematical models based on the experimental data in two-phase free jet flow, are developed for hazard and risk assessment. With the help of non-intrusive measuring techniques, it becomes possible to perform quite detailed measurements for small scale releases in both the laboratory and outdoors. In addition to the operational conditions, other circumferential parameters have to be considered, such as the climate stability and the ambient conditions, to improve the performance of the mathematical models. Approaches in two-phase free jet flows yield measurements of droplet size, velocity and rain out along with entrainment of the ambient air into the jet flow that are summarized in Tab. 3.

Tickle et al. [99] performed outdoor releases of dense gases like Ammonia, Freon 11 and Propane under flashing and fluid dynamic conditions. Their experimental investigations include measurements of the jet velocity and the entrainment in the far field downstream distance from the jet source. The experimental data were essentially validated by applying the entrainment model of Morton et al. [72] for the development of a universal model. In a similar approach, Webber et al. [107] investigated the releases of gaseous jets of Ammonia and Hydrogen fluoride. The buoyancy/ gravity effects on the jet behavior become more significant with the downstream distance. The gravity effects are stated to bend the jet trajectory, thereby, suppress entrainment. Upstream from this spatial location, the jet momentum has the major role on the entrainment process. In an advanced attempt to correlate the outlet flow conditions with respect to the dispersion characteristics, Whitlow et al. [110] utilized vertical two-phase air/ water free jet flows. A correlation for estimating the droplet size was proposed and validated based on experimental data of droplet size, velocity and rain out under a variation of air to liquid mass flow ratio.

Chen et al. [11] examined the effect of the flow conditions and the liquid properties on only the air entrainment for air/ water, oil and corn syrup free jet flows, where visualization methods were implemented to investigate the variation of the air entrainment established for different types of nozzles. In the investigations by Surma [96] a model was derived correlating the two-phase jet characteristics with the nozzle flow conditions based on the measurements of droplet size and velocity of air/ water free jet flows. Hetsroni et al. [32, 33] performed air/ oil dispersion by using a liquid phase with higher viscosity than that of water in two-phase free jet flows. The entrainment coefficient based on these experimental investigations was included in the calculations of the droplet velocity following the Gaussian profile. It was also deduced that the viscous

liquid phase in the jet flow causes suppression of the jet turbulence level and, hence, the model values for the two-phase entrainment coefficient differ distinctly with the nozzle downstream distance.

Author	Test fluids	Droplet Size	Velocity	Rain out	Entrain- ment
Tickle et al. [99]	Ammonia, Freon 11, Propane	−	+	−	+
Webber et al. [107]	Ammonia, Hydrogen fluoride	−	+	−	+
Whitlow et al. [110]	Air/water	+	+	+	−
Chen et al. [11]	Air/water, oil, corn syrup	−	−	−	+
Surma [96]	Air/water	+	+	−	−
Hetsroni et al. [32, 33]	Air/oil	−	+	−	+
Theofanous et al. [98]	Air/glycerin, tributyl phosphate	+	+	−	−
Kumagai et al. [52]	Air/corn syrup	−	−	−	+
Van de Sande et al. [101]	Air/water	−	−	−	+
Faeth et al. [22]	Air/water, glycerol, n-heptane, ethyl alcohol	+	+	−	+

Tab. 3: Test fluids and measurements of droplet size and velocity, rain out and entrainment in two-phase free jet flows

Theofanous et al. [98] applied high speed cinematography in addition to measurements of the droplet size and velocity in air/ Newtonian liquid, specifically, glycerin and tributyl phosphate free jet. Further more, these experimental investigations accentuated the effect of the liquid viscosity on the jet characteristics by retarding the droplet velocity due to the development of surface wave or so called interfacial roughness, without considerations taken for the effects of entrainment process on the droplet velocity. While in the study by Kumagai et al. [52], the air entrainment was only investigated and validated based on two-phase air/ corn syrup free jets. The effect of other liquid physical properties, e.g., the surface tension was disregarded since the jet flow possesses enough inertia to overcome these effects as was confirmed in other studies by Langner [54] or Hoyt et al. [37]. Van de Sande [101] performed experiments with air/ water free jet along with the jet visualization of vertical oriented jet flows. Their experimental results

provide information on the aerodynamic effects of the ambient on the droplet motion. This is also stated in the experimental investigations of Faeth et al. [22] based on the measurements of the droplet size and the velocity along with the air entrainment of two-phase air/ liquid phase such as water, glycerol, n-heptane and ethyl alcohol free jet flows under fluid dynamic conditions. In total, it was deduced that there is a variation in the jet characteristics with the downstream distance, and the acceleration plays a major role in establishing the droplet velocity in the jet near field region.

On resuming these experimental and analytical approaches performed on the dispersion of the two-phase air/ liquid free jet, the validity of the effect of high viscosity liquid phase on the entrainment process has not yet been investigated, especially, the momentum induced two-phase free jet flow under fluid dynamic and isothermal conditions. In the mean time, the effect of liquid viscosity on the air entrainment in two-phase air/ liquid free jet is still stochastic. Measuring the droplet velocity and size in the jet near as well as far field regions would provide sufficient information for characterizing the effect of liquid viscosity and flow conditions on dispersion flow. Herein, high inertia of the viscous liquid phase has the effect on the established droplet velocity in both the radial and downstream directions and, hence, should be considered for the prediction of the droplet velocity and the droplet spectra for the purpose of the validation in real dispersion scenarios.

In the jet far field region, the generated droplets will be progressively entrained into the air stream and, hence, the air entrainment significantly affects the behavior of the free jet. This entrainment is especially enhanced at a downstream distance of longer than 30 nozzle outlet diameters due to the contribution of both the co-flowing and the entraining air streams, this as well was stated by Bricard et al. [7], Crow et al. [16], Dahm et al. [18], Kuhlman [51], Pitts [79] or Schlünder [91]. For a proper understanding of the effect of the physical properties especially the liquid viscosity and the nozzle flow conditions on the entrainment coefficient, the state of the literature on this feature is introduced in the following section.

3.1.1 Entrainment coefficient

In an attempt to correlate the air entrainment coefficient with the fluid physical properties and the nozzle outlet flow conditions, the experiments by Hill [35], MacGregor [62] or Song et al. [95] reveal, in the two zones of Expansion and Air Entrainment, that the air mass flow rate entraining from the ambient increases with the axial distance, due to the larger perimeter of the expanding and the growing jet width. This finding is used to relate the normalized entrained air mass flow rate with the normalized axial distance and the air density ratio of the ambient to that of the jet at the nozzle, with the help of a constant entrainment coefficient following the definition

$$\frac{\dot{M}_{Ent}(s)}{\dot{M}_{Air,\,Nozzle}} = C_{Ent} \cdot \frac{s}{d_{Nozzle}} \cdot \sqrt{\frac{\rho_{Air(P_{ambient})}}{\rho_{Air,\,Nozzle}}} \quad \text{with} \quad 0.15 \le C_{Ent}\,[-] \le 0.457 \quad,$$

where $\rho_{Air,\,Nozzle}$ is the air density related to the nozzle outlet flow conditions. The entrainment constant, C_{Ent}, characterizes the local amount of air entrained into the jet. Hill [35] gives a value of 0.15 that is valid for the jet near field region, and a value of 0.35 refers to the jet far field regio, while MacGregor [62] states, irrespective of the jet field region, a constant value of 0.4 in comparison to a fixed value of 0.457 advocated by Song et al. [95]. Meanwhile, Ricou et al. [86] proposes a model for the air entrainment coefficient that is to be regarded constant with a value of 0.282. The variation in the proposed values is likely due to differences in the measuring techniques as well as to the nozzle downstream locations where the measurements were taken.

For the case of a two-phase air/ liquid free jet flow, MacGregor [62] speculates that the liquid phase may alter the degree of air entrainment. The two-phase entrainment coefficient definition basically relates to the local total air mass flow including that entrained from the ambient into the free jet boundary to the constant liquid mass flow as

$$C_{Ent,\,2ph} = \frac{\dot{M}_{Air}(s)}{\dot{M}_{Liq}} = \frac{\dot{M}_{Air,\,Nozzle} + \dot{M}_{Ent}(s)}{\dot{M}_{Total}(s) \cdot (1 - \dot{x}_{Air}(s))} \quad \text{with} \quad \dot{x}_{Air}(s) = \frac{\dot{M}_{Air}(s)}{\dot{M}_{Total}(s)}$$

$$\text{and} \quad 0.1 \le C_{Ent,\,2ph} \le 0.23 \quad,$$

whereby, according to Falcone et al. [23], the two-phase flow entrainment coefficient varies within the jet near field region from a value of 0.1 to 0.23. This variation is likely to account for the different nozzle exit flow conditions applied for the measurements.

Following this definition, it becomes evident that the two-phase entrainment coefficient is indispensably and continuously increasing with the downstream distance, whereby, according to the degree of entrainment in the specific zones and regions of the jet, different gradients may become established. Indeed, this entrainment coefficient definition implies that the air entrainment rate is responsible for the increase of the total jet flow rate with the downstream distance. This is further confirmed by the experiments by Crow et al. [16] or Malmström et al. [63] in the two-phase jet flow near field region, i.e., at a downstream distance of less than ten nozzle outlet diameters, elucidating that the entrainment coefficient in this region is lower than that in the Similarity region of the jet, i.e., at a downstream distance of greater than thirty nozzle outlet diameters.

MacGregor [62] suggests a linear relation for the change of the jet total mass flow rate with the nozzle dimensionless downstream distance. This proposal, however, was based upon experiments with single-phase gas free jet flow. For the case of two-phase free jet, the difference between the two-phase jet density and that of the ambient air is included by Malmström et al. [63] by modifying the entrainment rate correlation with the square root term of the density ratio of the ambient air to that of the jet at the nozzle outlet conditions, following

$$\dot{M}_{Total}(s) = \dot{M}_{Total(Nozzle)} + \dot{M}_{Ent}(s) = \dot{M}_{Total(Nozzle)} + B \cdot \dot{M}_{Liq} \cdot \left(\frac{s}{d_{Nozzle}} \right) \cdot \sqrt{\frac{\rho_{Air(P_{ambient})}}{\rho_{Nozzle}}} \quad ,$$

where a variety of proposals for the correlation constant, B, can be found in the literature, the value of 0.288 was stated by Malmström et al. [63] compared to the value of 0.26 by Seifert et al. [92], while Kuhlman [51] used the value of 0.303. Again, the variation in the proposed constants is likely due to the attempts to fit the experimental data obtained by different measuring techniques of the air entrainment mass flow rate and possibly specific least square procedures.

The experimental results by Hussein et al. [39], Pitts [79], Liepmann et al. [58] or Van de Sande et al. [101] state that the nozzle flow conditions, or the Reynolds number of the jet flow, allow for the description of the variation of the entrainment intensity in the two-phase air/ liquid free jet flow with the downstream distance. From experiments by Sallam et al. [88], Wong et al. [113] or Wygnanski et al. [115] emerged accordingly that the intensity of the air entrainment process is expected to be significant for establishing droplet size distribution. In particular, the primary breakup of the liquid in the Core/ Transition region yields fragments that are intrinsically weakened against the impact of the relatively large vortical structures and, therefore, prone to further deformation, so that these vortical air flow structures govern the local self establishing droplet size distribution in a two-phase free jet flow. Now, the state of the technology for predicting the establishing droplet size in the nozzle downstream distance is described. The droplet size is required as a function of the nozzle flow conditions as well as liquid physical properties for modelling the dispersion flow and the droplet rain out.

3.1.2 Mean droplet diameter

As confirmed by Azzopardi et al. [1], Pilch et al. [78], Walton et al. [106] and Wierzba [111], the process of deformation and breakup of viscous liquid droplets in a turbulent gas stream is sensitive to small changes of the flow conditions. The dependence of the droplet breakup on the upstream flow conditions are stated by Brodkey [8]. Indeed, the critical Weber number was proposed as a relation of the Ohnesorge number and reads

$$We_{crit} = 12 \cdot \left(1 + 1.066 \cdot Oh^{1.6} \right) \quad \text{and} \quad Oh = \frac{\eta_{Liq}}{\sqrt{\rho_{Liq} \cdot \sigma \cdot d_{Nozzle}}}$$

This relation provides information to distinguish between the various breakup processes as well as the dominating mechanism taking place according to the operational conditions. It was examined with data from literature for two-phase flow systems along with the experimental results to obtain a model value for the critical Weber number. Fig. 12 depicts the prediction by Brodkey correlation along with the experimental data for the air/ liquid system according to Schmelz [90] and Hanson et al. [29] as well as for the liquid/liquid systems according to Li et al. [57]. Some data, included within the dashed lines, are also plotted. Obviously Brodkey correlation properly predicts the experimental data, provided that the two-phase flow possesses a relatively high level of turbulence intensity. Accordingly, the critical Weber number will be substituted a value of 12 for Ohnesorge number less than a value of 0.1, leading to an upper value in the calculations for the maximum stable droplet diameter in the range between 160 and 250 μm, with respect to current experimental results, while the Sauter droplet diameter ranges between 120 and 330 μm for the nozzle diameters of 3 mm and 10 mm.
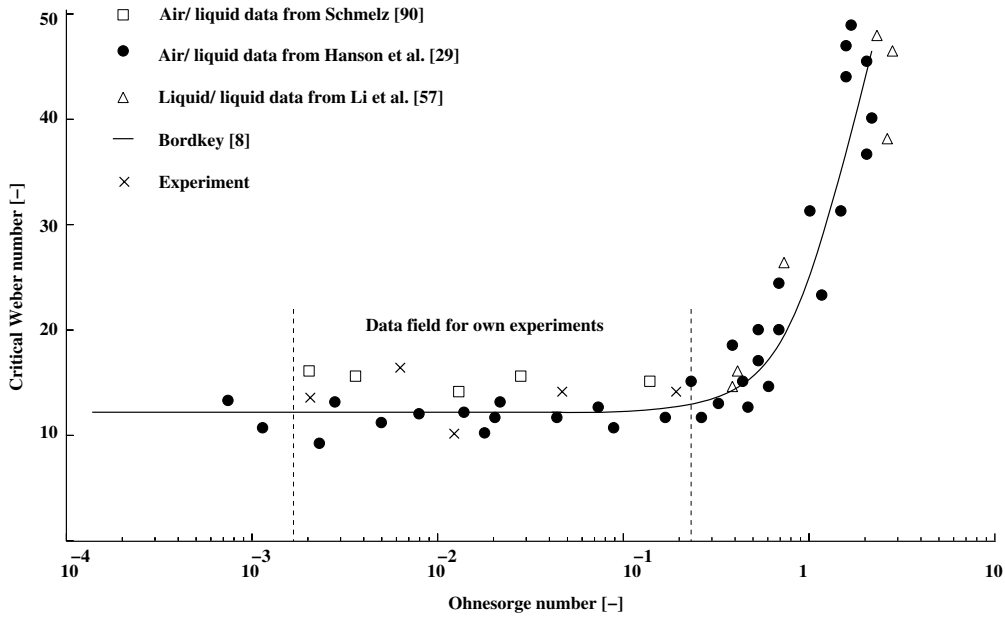
Fig. 12: Critical Weber number as a function Ohnesorge number according to Pilch et al. [78]

Basically, under stationary flow conditions at any local downstream distance within the jet flow, a sequence of droplet sizes will be established, leading to a spectrum of droplet sizes. A prediction for the characteristic droplet diameter of the spectrum on the jet centerline is given by Teng et al. [97] in case of air/ Newtonian liquid flow. Teng's model reads

$$\frac{d_{droplet_{centerline}}}{d_{Nozzle}} = 1.88 \cdot (1.16 + +0.0236 \cdot lnOh) \cdot (1 + 1.1 \cdot Oh)^{\frac{1}{6}} \qquad \text{with}$$

$$Oh = \frac{\eta_{Liq}}{\sqrt{\rho_{Liq} \cdot \sigma \cdot d_{Nozzle}}} \quad \text{for} \quad 0.003 \leq Oh \leq 0.167 \qquad \text{and} \qquad 0.4 \leq \eta_{Liq} \leq 22.9 \, \text{mPa s} \quad ,$$

where the Ohnesorge number [74] reflects the ratio of the viscous to the inertial forces. Within this parameter range, on average, the characteristic droplet diameter amounts to about one to two times the nozzle diameter.

Amongst others, Mansour et al. [65], based on experiments with a co-axial air-blast atomizer, where two independently controlled air streams are supposed to interact with the inner and outer surface of the liquid bulk flowing in the jet core, proposed a formula for the prediction of the Sauter droplet diameter, as the characteristic size in relation to the nozzle outlet diameter, as a function of the liquid to air mass flow ratio, the Weber number and the Ohnesorge number. The formula reads

$$\frac{d_{Sauter}}{d_{Nozzle}} = \left(1 + \frac{\dot{M}_{Liq}}{\dot{M}_{Air}}\right) \left[0.169 \cdot We^{-0.5} + 0.581 \cdot Oh\right] \qquad \text{with}$$

$$We = \frac{\rho_{Air} \cdot (u_{Air} - u_{droplet})^2 \cdot d_{Nozzle}}{\sigma} \quad , \quad Oh = \frac{\eta_{Liq}}{\sqrt{\rho_{Liq} \cdot \sigma \cdot d_{Nozzle}}} \quad \text{and}$$

$$d_{Sauter} = \frac{\sum n_{droplet} \cdot d_{droplet}^3}{\sum n_{droplet} \cdot d_{droplet}^2} \quad ,$$

where $N_{droplet}$ is the number of the detected droplets in a size class. A relatively larger Sauter diameter indicates, in this context, larger droplets and/or a wider size spectrum. The definition of the Sauter diameter is just included here for the sake of completeness. The Sauter droplet diameter is accessible only by dedicated experiments, so that these details are not required for the application of this method.

The Weber number and the Ohnesorge number are defined according to Mansour et al. [65] with respect to the nozzle diameter. By using the Ohnesorge number, especially with a higher exponent than that of the Weber number, the liquid viscosity and, hence, the viscous forces play the major role in the droplet deformation process, along with the superimposed effects of the aerodynamic forces related to the velocity difference between the air and the droplet. These effects may change with the nozzle downstream distance and, hence, may cause a variation in the self-establishing droplet size distribution, consequently, the Sauter droplet diameter. In total, the average Sauter droplet diameter amounts to about one half the nozzle diameter for the two-phase free jet flow of air/ liquid phase with a viscosity lower than 30 mPa s.

The dependence of the mean droplet diameter of an aerosol dispersion was characterized by Krishna et al. [50] on the basis of a dimensional analysis. Accordingly, mean droplet diameter depends on the operating conditions, the nozzle type and downstream distance. This could also

be valid for the macroscopic aerosol distribution meaning the discrete droplet size in a free jet. Density and viscosity of both phases as well the nozzle outlet velocity are also introduced, as independent parameters, in this approach. The self-established mean droplet diameter is given finally as the relation in the form

$$\frac{d_{droplet}}{d_{Nozzle}} = f(\rho_{Air}, \eta_{Air}, \frac{1}{\rho_{Liq}}, \eta_{Liq}, \sigma, \frac{1}{u_{droplet}}, \frac{1}{s}) \quad \text{with} \quad u_{Nozzle} = f(\Delta P, \rho_{Liq}) \quad ,$$

where ΔP is the pressure difference due to the flow through the nozzle. Accordingly, the droplet diameter in air, for otherwise equal conditions, is decreasing with a higher droplet velocity, a lower liquid density and a larger surface tension. While a higher nozzle outlet velocity is achieved by increasing the air/ or the liquid mass flow, thus, a dispersion under or close to critical flow conditions is achieved. In total, this approach does not include much useful information on the effect of the liquid viscosity on the behavior of a two-phase air/ liquid free jet within the momentum dominated region.

For the description of the characteristic droplet size in the free jet flow, many empirical correlations have been also proposed. Among the most well-known empirical correlations are Rosin - Rammler, Nukiyama - Tanasawa, and the upper limit distributions, their definitions are given in details by Azzopardi et al. [1] and only mentioned here. In general, these empirical correlations are mostly short of a universal reproductive capability with the nozzle downstream distance and, hence, will not be followed. As an alternative, Richter [85] applied the Rosin, Rammler, Sperling and Bennet distribution. It is basically a cumulative distribution function and reads

$$Q_{cum} = 1 - exp\left(-\frac{d_{droplet}}{\bar{d}_{droplet}}\right)^m \quad ,$$

where $\bar{d}_{droplet}$ is a mean droplet size determined by statistical methods for the droplet population, where 63.2 % of the droplets have a diameter less than this value. While m is the exponent for the cumulative function of the droplet size distribution. A smaller value of less than two implies a broader droplet size distribution if the turbulent conditions prevail. It is postulated that changes are caused to the droplet size due to the variation of the turbulent intensity and, hence, the established surface instability that is responsible for the droplet formation. In total, this model involves promising findings, consequently, will be further employed in current investigations. On resuming, some droplets also have larger diameters than the average size, so that they are distinctly affected by the gravity, i.e., to a greater extent than by the ambient air flow field. Thus, the domination of the effect of the gravitational force compared to that of the momentum induced inertia of a horizontal free jet flow, the droplets will rain out. This topic will be discussed in the next section.

3.1.3 Droplet rain out in horizontal jet flow

As a result of the intensive interactions between the generated droplets and the vortical flow structures within the jet central region, the droplets of small sizes, hence higher surface area per unit volume, are radially transported toward the jet periphery while the relatively larger droplets penetrate this region. With the downstream distance, the number of the smaller droplets increases at the jet periphery. Thereby, a droplet velocity profile is expected to be developed in the way that the jet flow approaches the velocity of the surrounding. In the jet central region, the centerline droplet velocity is postulated to have a maximal value, hence, the jet possess higher momentum with respect to the ambient. A cumulative droplet capture was proposed by Johnson et al. [43] to describe the droplet rain out. It reads

$$
f_{cum}(d_{droplet}) = \frac{\pi}{6} \cdot \rho_{Liq} \int_0^{d_{droplet}} d_{droplet}^3 \cdot p(d_{droplet}) \cdot \frac{d}{d_{droplet}}(d_{droplet})
$$

$$
with \quad p(d_{droplet}) = \frac{exp\left[-\frac{1}{2}\left(\frac{ln\,d_{droplet}}{ln\,\sigma_G}\right)^2\right]}{\sqrt{2\pi} \cdot ln\,\sigma_G} \qquad ,
$$

where $p(d_{droplet})$ is the probability function with respect to the droplet diameter, while σ_G is the standard deviation of the droplet size distribution. However, this approach principally requires a prior knowledge of the droplet size spectrum, which is only obtained with dedicating experiments. Due to the continual and the vortical flow structures with the nozzle downstream distance, the droplets will lose their momentum to the ambient. Consequently, the gravitational effects on the centerline droplet velocity will be significant. In the following section, the centerline droplet velocity will be presented.

3.1.4 Centerline droplet velocity

The centerline droplet velocity is defined in the literature as a function of the axial velocity in the Expansion Zone, the nozzle geometry, the two-phase free jet characteristics and the ratio of the local jet flow density to the that of the ambient. It is based on the one-dimensional momentum balance for a frictionless homogeneous flow and reads

$$
u_{droplet_{centerline}}(s) = \frac{u_{expansion_{Air}} \cdot d_{Nozzle}}{2 \cdot C_{Ent,\,2ph} \cdot (s - s_{virtual})} \cdot \sqrt{\left(\frac{\rho_{jet}(s)}{\rho_{Air(P_{ambient})}}\right)} \quad with
$$

$$
u_{expansion_{Air}} = u_{Nozzle} + \frac{(P_{outlet} - P_{ambient}) \cdot A_{Nozzle}}{\dot{M}_{Total(Nozzle)}} \quad , \quad u_{Nozzle} = \frac{\dot{M}_{Total\,(Nozzle)}}{\rho_{Nozzle} \cdot A_{Nozzle}} \quad ,
$$

$$\rho_{jet}(s) = 1 / \left(\frac{\dot{x}_{Air}(s)}{\rho_{Air(P_{ambient})}} + \frac{1 - \dot{x}_{Air}(s)}{\rho_{Liq}} \right) \quad , \quad \dot{x}_{Air}(s) = \frac{\dot{M}_{Air,\,Nozzle} + \dot{M}_{Ent}(s)}{\dot{M}_{Total}(s)}$$

$$\text{and} \quad C_{Ent,\,2ph} = \frac{\dot{M}_{Air}(s)}{\dot{M}_{Liq}}$$

The local jet density follows the so called homogenous two-phase flow density definition, while the jet mass flow quality is expressed as the ratio of the air mass flow to the total jet mass flow.

The local droplet velocity, at normalized downstream and radial distances, is calculated on the basis of the centerline droplet velocity with the assumption of a velocity profile according to the Gaussian function. Surma [96] proposed the following correlation with an exponent of 1.3 instead of the usual exponent of two in air/ relatively low viscosity liquid phase free jet flow

$$u(s,\,r) = u_{droplet_{centerline}}(s) \cdot \exp\left(-ln2 \left(\frac{r}{C_{Ent,\,2ph}\,(s - s_{virtual})} \right)^{1.3} \right)$$

$$\text{with} \quad C_{Ent,\,2ph} = 0.1 - 0.02 \cdot ln\left(\frac{1 - \dot{x}_{Air(Nozzle)}}{\dot{x}_{Air(Nozzle)}} \right) \quad ,$$

$$s_{virtual} = \left(19.1 - 1.1 \left(\frac{1 - \dot{x}_{Air(Nozzle)}}{\dot{x}_{Air(Nozzle)}} \right) \right) \cdot d_{Nozzle} \quad \text{and} \quad \dot{x}_{Air(Nozzle)} > 0$$

The two-phase jet characteristics, namely the two-phase entrainment coefficient and the virtual origin, are basically related to the discharged liquid to air mass flow ratio for an air quality at the nozzle outlet in excess of zero.

In contrast to the model by Surma [96], the Ejet code developed by Woodward [114] applies the Gaussian function with the usual exponent of two. Exemplarily, the velocity profile for a horizontal jet flow is defined by

$$u(s,\,r) = \frac{u_{Nozzle} \cdot d_{Nozzle}}{0.08 \cdot s} \cdot \sqrt{\left(\frac{\rho_{Nozzle}}{\rho_{jet}(s)} \right)} \cdot exp\left(-ln2 \left(\frac{r}{0.04 \cdot s} \right)^{2} \right)$$

The velocity profile is valid for the momentum dominated two-phase free jet flow and includes a constant two-phase entrainment coefficient with a value of 0.04. The related virtual origin is set to zero, while the air expansion was not considered. The square root of the normalized jet density at the nozzle flow conditions with respect to the local jet flow density accounts for the

37

development of the nominal width of the jet with the nozzle downstream distance.

The model by Iannello et al. [40] includes, in contrast to Surma, a Top-hat profile for the droplet velocity and is based on a constant value for the two-phase entrainment coefficient of 0.08 and a related virtual origin of zero. It reads

$$u(s,\,r) = u_{droplet_{centerline}}(s) = \frac{u_{Nozzle} \cdot d_{Nozzle}}{0.16 \cdot s} \cdot \sqrt{\left(\frac{\rho_{Nozzle}}{\rho_{Air(P_{ambient})}} \right)}$$

The velocity difference between that of the air and the droplet according to Iannello et al. [40] can be neglected, since the entire liquid bulk in the jet flow is completely disintegrated into droplets of fine sizes. The droplets properly conform to the air flow field and, hence, the calculations for the two-phase free jet flow parameters are carried out corresponding to the nozzle outlet conditions without consideration of the air expansion effect on accelerating the droplet. In contrast, the radial and the axial expansion of the air is ascribed the major effect in establishing the droplet velocity. The radial or so called the normalized mean droplet velocity will be presented next.

3.1.5 Normalized mean droplet velocity

The normalized mean droplet velocity at a specific spatial location of the jet is evaluated on the basis of the centerline droplet velocity. It reads according to the model by Surma [96] the following correlation

$$\frac{u(s,\,r)}{u_{droplet_{centerline}}(s)} = \exp\left(-ln2 \left(\frac{r}{C_{Ent,\,2ph}\,(s - s_{virtual})} \right)^{1.3} \right)$$

Similar approach can be followed to express the normalized mean droplet velocity according to Woodward [114] and reads

$$\frac{u(s,\,r)}{u_{droplet_{centerline}}(s)} = \exp\left(-ln2 \left(\frac{r}{0.04 \cdot s} \right)^{2} \right)$$

The model of Iannello et al. [40] is calculating the normalized droplet velocity as a function of the centerline droplet velocity at each downstream distance. For the sake of evaluation of model predictions, the reproductive accuracy of the jet models is presented in the next section.

3.2 Reproductive accuracy of jet models

The reproductive accuracy of the mean centerline droplet velocity in two-phase free jet by the models of Surma [96] and Iannello et al. [40] will be discussed first in order to present drawbacks on the models evaluation as well the demands for further investigations.

Mean centerline droplet velocity

The centerline velocity downstream from the nozzle, which has an outlet diameter of 10 mm, has been measured at a stagnation pressures of 3 and 5 bar and mass flow qualities between 1.8 and 42.5 %. Exemplarily in Fig. 13, the experimental centerline droplet velocity and the measured Sauter droplet diameter are plotted versus the normalized axial distance in case of a liquid phase with a viscosity of 100 mPa s, at a stagnation pressure of 5 bar and a mass flow air quality of 8.2 %. Basically, the experimental mean centerline droplet velocity decays with the normalized axial distance and asymptotically approaches a lower value of about 30 m/s.
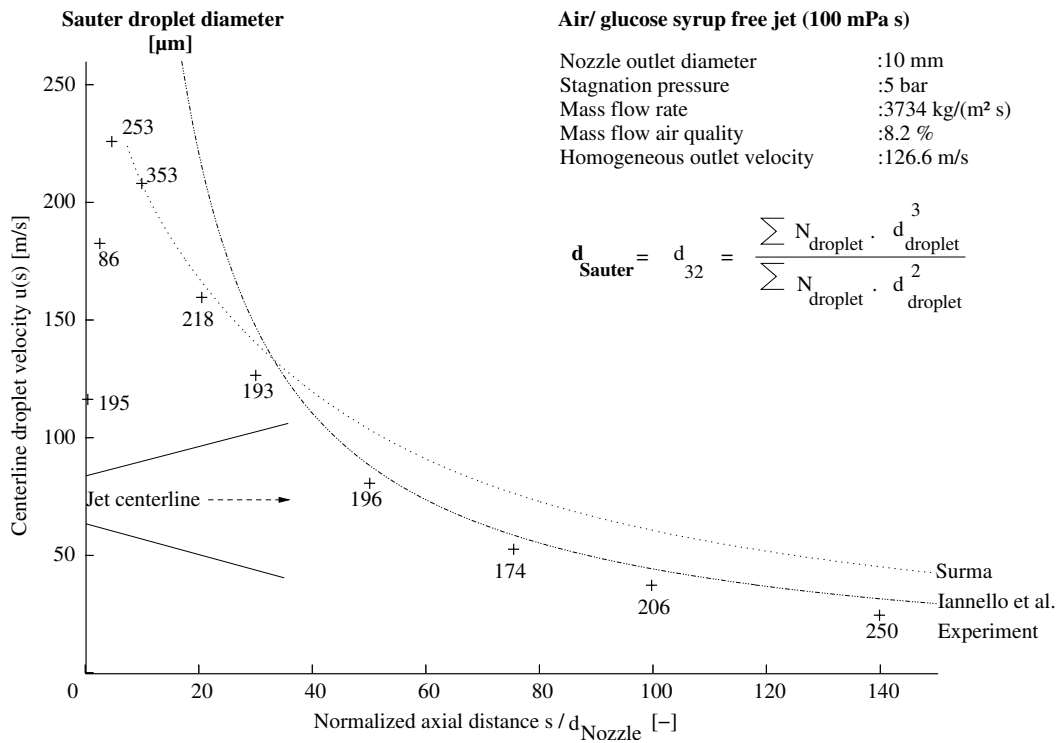
Fig. 13: Experimental centerline droplet velocity and Sauter droplet diameter as a function of the normalized axial distance and predictions by Iannello et al. [40] and Surma [96] model in case of viscous liquid phase

This trend is compared to the model predictions by Iannello et al. and Surma. It is obvious that the Surma model, originally developed for air and water mixtures, allows only for pertinent predictions of the centerline velocity in the near field distance of twenty outlet diameters from the nozzle outlet, i.e., in the Core/ Transition region. However, it shows a systematic

overprediction with the downstream distance. In comparison with the model by Iannello et al., which yields a considerable overprediction in the Core/ Transition region, that decreases in the far field distance allowing for a proper and moderate velocity overprediction in the Similarity region. This indicates that the actual length scale for the decay is somewhat shorter than that predicted by both models, leading in general to an overprediction of the centerline velocity. In view of an improved free jet flow modelling, this supports a variation in the defined constant jet characteristics with the normalized axial distance. A substantial change is also observed in the experimental Sauter droplet diameter, yet no systematic trend can be deduced for its variation with the normalized axial distance. This change can be attributed to the combined influence of the air entrainment and the subsequent liquid fragmentation which affects the local droplet size distribution. Obviously, also the predicted length scale for the centerline velocity should be formulated by a redefinition of the entrainment coefficient and the virtual origin.

Normalized mean droplet velocity

In Fig. 14, the experimental normalized mean droplet velocity is plotted against the normalized radial and downstream nozzle distance for a liquid phase with a viscosity of 8 mPa s, at a stagnation pressure of 3 bar and a mass flow air quality of 2 %.
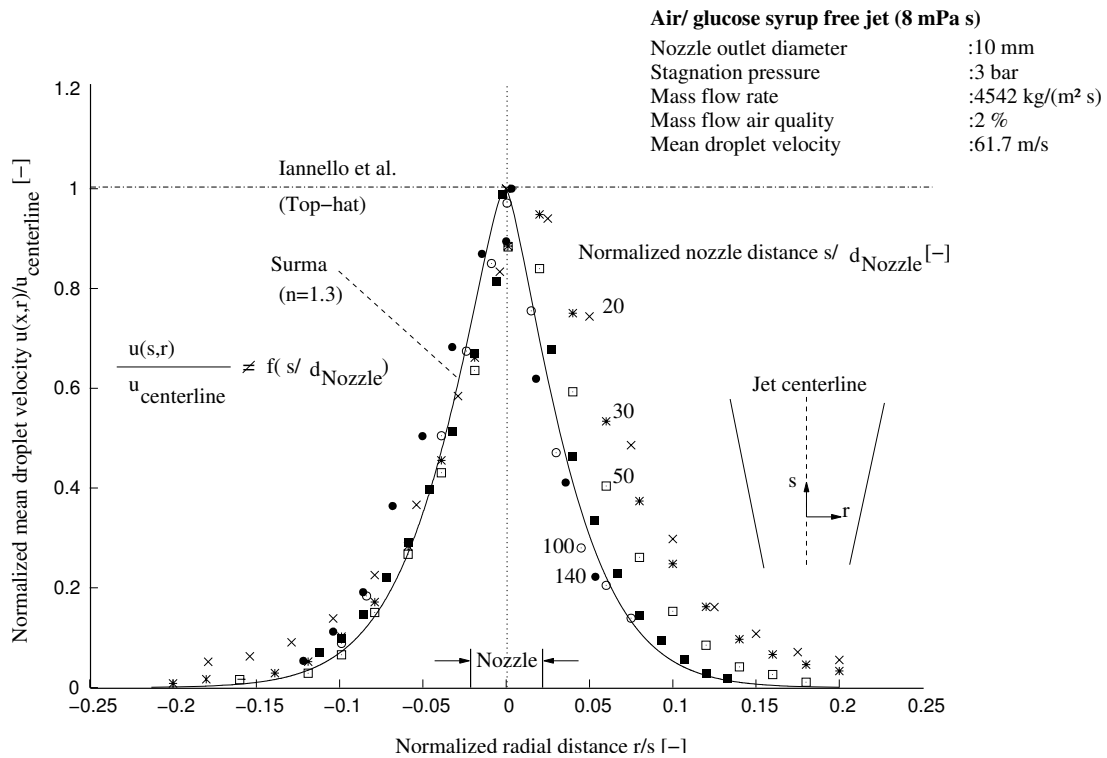
Fig. 14: Experimental normalized mean droplet velocity as a function of the normalized radial distance and prediction by Iannello et al. [40] and Surma [96] model in case of viscous liquid phase

40

It can be seen that the velocity distributions in the radial direction in the Core/ Transition as well as Similarity region, independent of the nozzle downstream distance, relax to an almost symmetric bell-shaped velocity profile as in single-phase gas free jets. A maximum value of the droplet velocity is achieved, as expected, at the jet centerline. It then monotonically starts to decrease in the direction towards the jet periphery, when it asymptotically approaches a value of zero. The proper predictions according to the model by Surma, which follows the Gaussian function for the radial velocity profile, are obvious even in the Core/ Transition region, whilst the Top-hat profile used in the model by Iannello et al. is obviously not adequate. The flow fluctuations can significantly induce a shift in the local velocity distribution, e.g., as it is manifested in the distribution of the measured velocity at downstream distances of 20 and 30 nozzle outlet diameters. In the domain of this spatial distance from the nozzle outlet, the aerodynamic forces have the dominant effect on the droplet formation process as such was reported, e.g., by Hsiang et al. [38] and Tseng et al. [100]. Likewise, these phenomena can be attributed to the locally different fluid dynamic shear stress induced by the velocity difference between both phases that becomes significant in the Core/ Transition region.

3.3   Conclusion and research demand

Based on the initial evaluation of the model predictions of the experimental data, a short predicted length scale for the jet flow is appeared, therefore, a poor accuracy is obtained in reproducing the droplet velocity. Better agreement, with respect to preliminary model predictions by Surma, prevails by following Gaussian profile rather than the Top-hat profile and applying homogeneous two-phase flow density and viscosity definitions for calculating of the two-phase parameters. The local droplet velocity should be simply related to the velocity at the jet centerline. The air expansion in the radial and the axial directions and the downstream deceleration, due to the air entrainment must be considered. In retrospect, the two-phase entrainment coefficient and the jet virtual origin should also be reformulated, with respect to the nozzle flow conditions and the downstream distance, to increase the predicted length scale of the centerline and the normalized mean droplet velocities rather than implementing constant values for the two-phase jet characteristics. Detailed experimental results would essentially provide the potential to achieve more comprehensiveness of the behavior of the two-phase air/ liquid phase free jet flow. For this purpose, experimental investigations including the measurements of the local droplet velocity distribution and size spectra are addressed in the next chapter.

4 Experimental investigations

This chapter is devoted to the measurements of the mean droplet velocity and size spectra by means of a two-dimensional Phase Doppler Anemometer. High speed cinematography was used to aid in the visualization of two-phase free jet flows. After presenting the instrumentation and fluids physical properties, the experimental results will be discussed.

4.1 Test rig

The test rig is depicted in Fig. 15. A steady liquid flow is supplied from the liquid phase capture system with the help of a pump and delivered across the flowmeter to the mixer. Ambient air is used as the test gas phase. It is pressurized by a compressor and subsequently flows through a dryer to extract humidity and is then stored in a buffer tank. Both phases are introduced into the mixer formed by two interpenetrated pipes. The air flows into the central pipe where the liquid phase stream is in the gap in between. The two-phases are mingled in the mixing chamber prior to the nozzle.
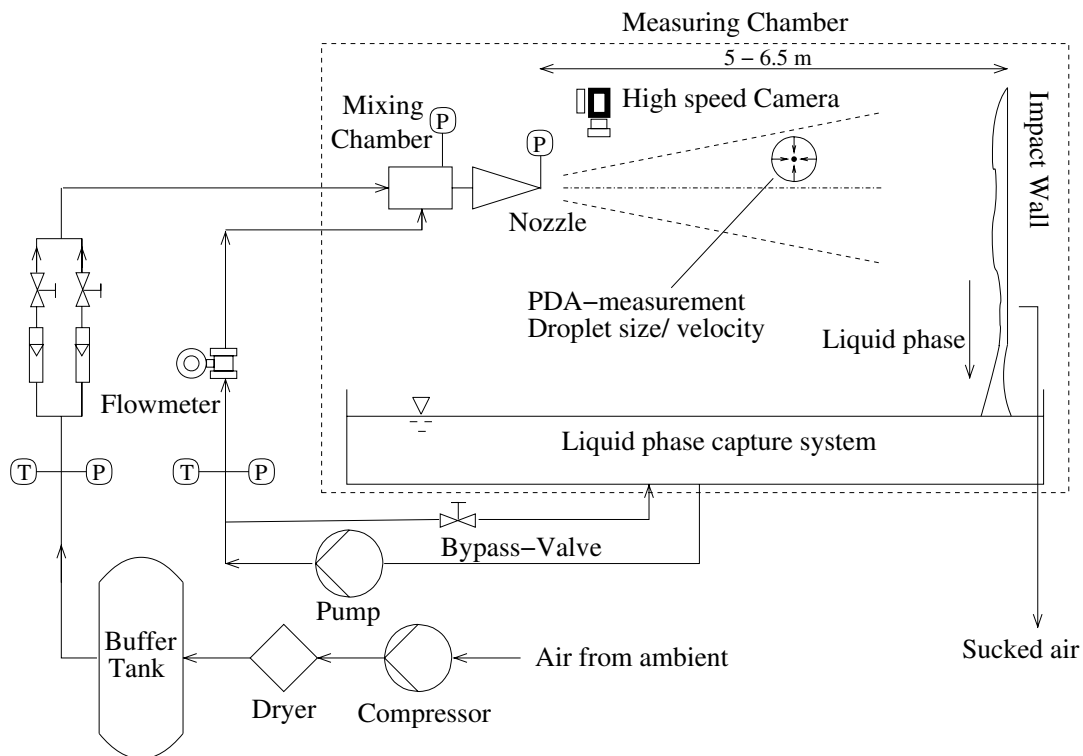
Fig. 15: Test rig for two-phase free jet flow experiments

The free jet is observed in a measuring chamber with a length of 6.5 m. At the end of the measuring chamber, an impact wall is mounted to overcome the dynamics of the jet. The impact wall is equipped with an air suction port to extract the excess air to the surrounding and, hence, to prevent secondary air flows as well as a pressure build up. This arrangement

ensures that the free stream ambient air velocity in the measuring chamber is kept at quiescent conditions. The liquid phase is collected in the capture system and is recycled. The liquid phase and air volume flow rates are measured by flowmeters with a maximum capacity of 3 m^3/h of the liquid phase and 58 Nm^3/h of air under a maximum storage pressure of 10 bar. The air mass flow quality can be determined with measuring the pressure, temperature and flow rate of each phase. The error margin for the calculation of air volumetric flow rate is within ± 0.5 Nm^3/h resp., ± 1.5%. While the liquid flowmeter exhibits a measuring error of ±30 L/ h which is about ± 1 % of the measured value.

Although the normalized mean droplet velocity gives an indication of the two-phase jet symmetry, it provides little information on how the liquid mass flux is distributed radially and circumferentially within the jet flow. To acquire this information, droplet rain out basin or the so called patternator is implemented. It typically consists of a number of square sectors, each one drains into separate collecting flasks. The definition of the experimental dimensionless droplet rain out capture at a specific location is given as

$$f = \frac{\dot{M}_{Liq\,(Rain\,out)}(s,\,r)_i}{\sum_{i\,=\,1}^{8} \dot{M}_{Liq\,(Rain\,out)}(s,\,r)_i}$$

Eight collecting flasks are used in the current study for the droplet rain out investigations. The flasks, located under the patternator in the azimuthal orientation, are equidistant from the nozzle. The next section focuses on the nozzle geometry.

4.1.1 Nozzle geometry

A nozzle consists of three parts: the mixing chamber where the gas phase disperses in the liquid phase to establish the two-phase air/ liquid flow. The conus where the cross sectional area of the pipe decreases, in parallel, the two-phase flow accelerates. The third part is the nozzle where the two-phase flow is set forth, herein a certain pattern depending on the flow conditions, to establish laterally the free jet flow into the quiescent ambient with equal or lower pressure. Fig. 16 depicts the nozzle geometry with the relevant pipe dimensions, the nozzle outlet diameter d_{Nozzle} and length L_{Nozzle}. The scheme shows the two interpenetrated pipes connected to the mixing chamber that, in turn, are joined with the nozzle, which allows to directly measure the pressure in the mixing chamber as well at the nozzle outlet. The pressure of the mixing chamber was fixed at a certain value for the investigated mass flow rates of both phases with altering the liquid physical properties, accordingly the value for the outlet pressure will vary. Three geometries are investigated with a nozzle diameter of 3, 5 and 10 mm with a different diameter to length ratio of 10, 7.4 and 6. The indicated geometries were selected to cover the most anticipated normal and upset dispersion scenarios, as well due to the test rig feasibility and laboratory room limitations. The relevant dimensions of the nozzle geometries

and the established two-phase free jet flows provide a confidence in the extrapolation of the experimental conditions to large scale dispersion flows.

d_{Nozzle}	L_{Nozzle}	L/d_{Nozzle}	φ
[mm]	[mm]	[−]	[°]
3	30	10	30.2
5	37	7.4	28.1
10	60	6	22.7
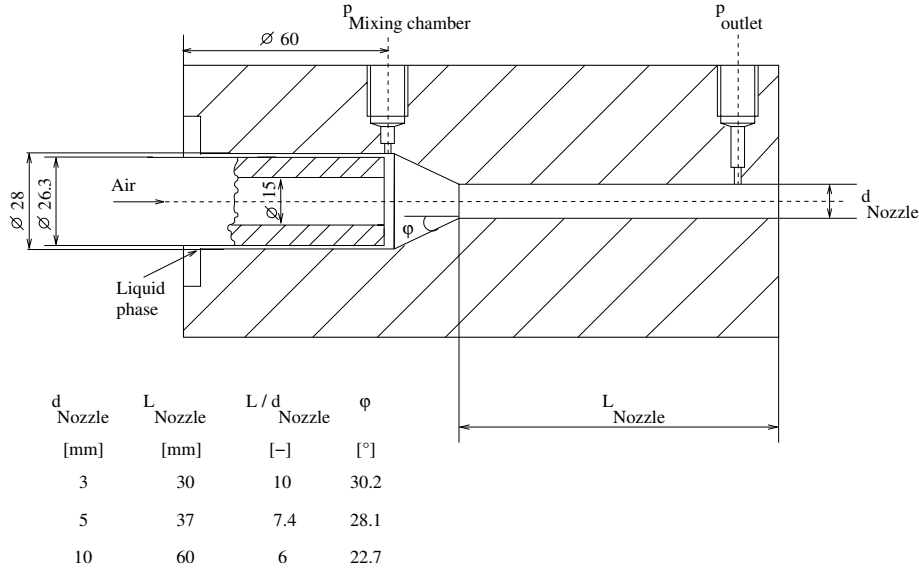
Fig. 16: Nozzle geometries used for the establishment of two-phase air/ liquid phase free jet flows

Altering the diameter to length ratio of the nozzle will change the angle φ from 22.7 to 30.2°. This in turn has an impact on the acceleration of the two-phase flow, hence, the state of the flow at the nozzle outlet. Under these conditions, measurement of the mixing chamber and outlet pressures may give an estimation of the two-phase flow state at the nozzle outlet. Under critical or semi-critical flow conditions, the relation of the mixing chamber and the outlet pressures to the total mass flow rate from the nozzle reads

$$P_{Mix} = P_{outlet} + \frac{\dot{m}^2_{Total\,(Nozzle)}}{2 \cdot \rho_{Nozzle}} \qquad ,$$

where P_{Mix} refers to the pressure in the nozzle mixing chamber. One of the potential targets of the current study is to extend the scope of previous investigations to include wide variations in the flow conditions and the liquid properties. On confirming the capability of the test rig to simulate a dispersion flow, with a systematic variation of the mass flow air quality in the range of 1 to 46 %, it is possible to vary the mixing chamber pressure between 2 and 7 bar for the investigated nozzle outlet diameters. The nozzle is mounted in the horizontal direction due to the pre-defined or enforced orientation of the droplets for measuring purposes. Furthermore, there is a possibility of an instable behavior for the vertical orientation of the free jet flow as well as due to the laboratory room limitations. The instrumentation implemented for the measuring purposes follows in the next section.

4.2   Instrumentation

The measurements of the droplet velocity and size have been performed with the Phase Doppler Anemometry technique. High speed cinematography is used to visualize the jet flow at different nozzle downstream locations. Phase Doppler Anemometry technique is firstly described.

4.2.1   Phase Doppler Anemometry technique

Laser-based techniques, implemented for measuring the droplet attributes in two-phase free jet flows, have the following advantages: non-intrusive nature, data acquisition rates and the speed of processing. This technique involves setting up an interferogram in space by overlapping two monochromatic, similarly polarized interacting beams which, subsequently, provide signals as the liquid droplets pass through the measuring volume. A very small volume in the order of 1 mm^3 is available for the measurements. The signals are collected by a receiver mounted with an off-axis angle and are further analyzed in order to obtain the the droplet velocity and size. The Phase Doppler Anemometry technique is capable of measuring a number of useful parameters for the free jet characterization, including local droplet velocity, size spectra, volume flux and number density of the generated droplets.

A schematic setup of Phase Doppler Anemometer is shown in Fig. 17. An argon-ion laser is used as a coherent light source. The laser beam is split by a beam splitter into two beams of equal intensity. One beam is shifted by a frequency of 40 MHz through the Bragg cell.
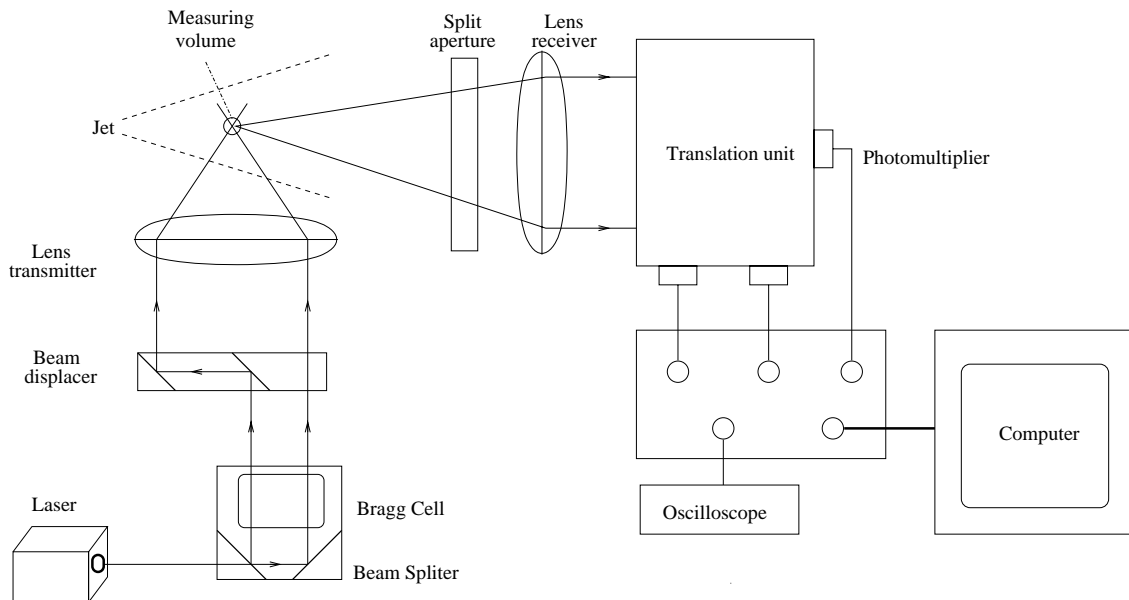
Fig. 17: Typical Phase Doppler Anemometer setup according to [24]

The resulting two parallel beams are adjusted by the beam displacer and then focused by the transmitter unit with a lens of 1000 mm focal length to establish the measuring volume. The

light, scattered from the individual droplets passing through the measuring volume, will be collected by a receiving unit with front lens of 1000 mm focal length. This split aperture acts as a spatial filter, focusing the light scattered from the droplets in the measuring volume with different wavelengths through the receiver to the translation unit. The translation unit contains three photomultipliers to convert the optical signals into electric for further data processing and downloading to a computer. The Doppler signal can also be displayed on an oscilloscope for an optical observation of the data acquisition.

Two beams with split angle, 2α, intersect establishing the measuring volume with an interference fringe spacing of Δs. Fig. 18 depicts the establishment of the measuring volume of two beams. Light scattered by the droplets, moving through the measuring volume, issue intensity modulated signals with a frequency that is directly proportional to the droplet velocity component normal to the fringes and is inversely proportional to their spacing.
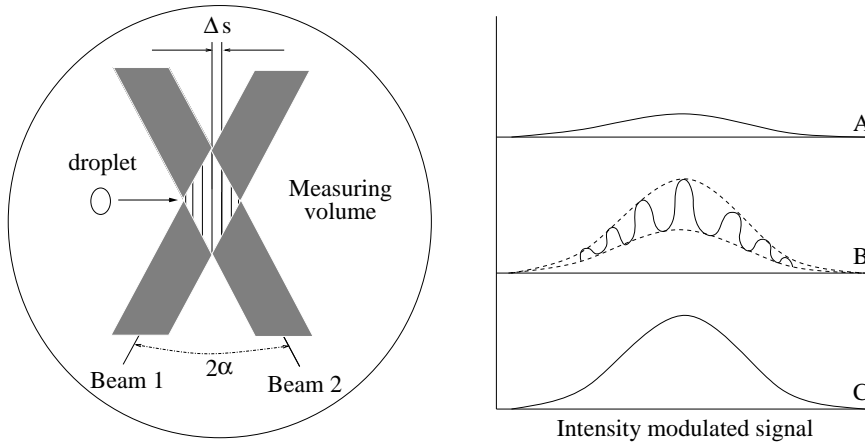
Fig. 18: Measuring volume of two intersecting laser beams along with the intensity modulated signal curves

The emitted scattered light shows three curves according to the position of the droplet with respect of the measuring volume. Position A outside the two beams intersection where no signals are detected. Position B where the droplet is located at the boundaries, the signal curve is characterized by the oscillating behavior. C is the position where the droplet is completely located within the measuring volume. From the analysis of these signals, the droplet velocity and size will be determined.

Droplet velocity

The interference fringes are planes of equal intensity, which are perpendicular to the plane of drawing. Droplets passing the measuring volume illuminate and scatter the light. The resulting oscillation is called Doppler signal. When a droplet transverses the measuring volume, the amplitude of the oscillations initially increases and then decreases according to the Gaussian

intensity distribution of the laser beams. Knowing the fringe spacing, the velocity component of the droplet in the plane of drawing that is perpendicular to the fringes, can be then calculated by the correlation

$$u_{droplet} = \Delta s \cdot f_D \quad \text{with} \quad \Delta s = \frac{\lambda_{wave}}{2 \cdot sin\alpha} \quad ,$$

where $u_{droplet}$ is the droplet velocity and f_D is the frequency of the Doppler signal. The fringe spacing, Δs, is determined by the beam intersection angle, 2α, of the two laser beams and the wave length, λ_{wave}, of the incident light.

Droplet size

The illumination is performed in the way where the Doppler signals are detected at two spatially separated sensors. Fig 19 shows the receiver orientation for the droplet size measurement with respect to the cartesian coordinates. The sensors detect scattered light at the off-axis angle θ. At least one of the sensors is not located in the same observation plane, but is elevated with an angle ϕ. From each sensor a Doppler signal is obtained and, by this, the signals show a phase difference with respect to each droplet based on its size.
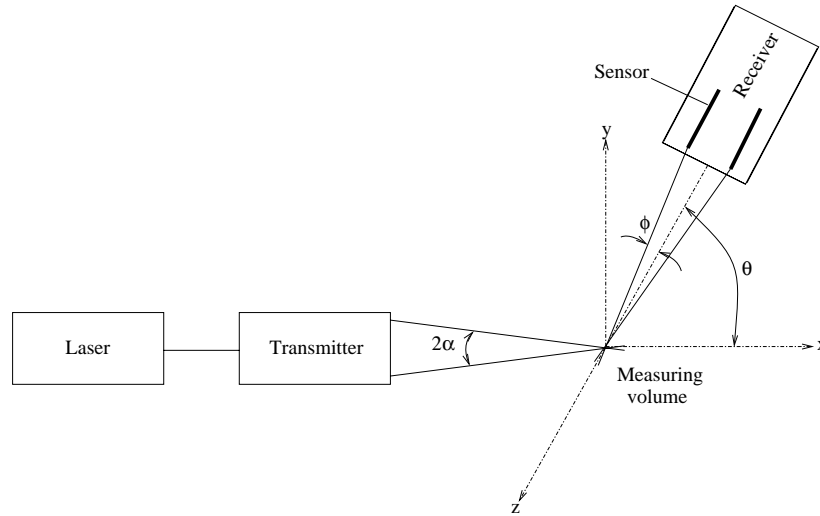
Fig. 19: Receiver orientation for the droplet size measurement with respect to the cartesian coordinates

The relationship between the measured phase difference, denoted by Φ_f, and the droplet size can be expressed by

$$d_{droplet} = \lambda_{wave} \cdot \Phi_f / \left[4\pi \cdot \sqrt{1 + n^2 - n \cdot \sqrt{2 \cdot (1 + \sin \alpha \sin \phi + \cos \alpha \cos \phi \cos \theta)}} - \right.$$

$$-\sqrt{1 + n^2 - n \cdot \sqrt{2 \cdot (1 + \sin\alpha \sin\phi + \cos\alpha \cos\phi \cos\theta)}}\;\Bigg]$$

The off-axis has the value of 60° with an elevation angle of 3.3°. Hence, by obtaining the phase difference and the refraction index, n, the droplet size can be determined. The measuring error of the Phase Doppler Anemometer technique is a compensation between the frequency and the velocity. The frequency error is about ±0.03 MHz, which would result in a velocity error of ±0.31 m/ s. For the droplet size, the measuring error is within the range of ±1%.

Phenomena associated with the droplet formation in the free jet flow, such as collisions or coalescence, can also be observed. When the droplets are simultaneously visualized, one can observe different stages of such phenomena, e.g., two droplets approaching each other and colliding to form a larger droplet. In the coming section, the cinematography is described.

4.2.2 Cinematography

Devices such as high speed Cameras can be arranged, according to the lenses and the light source, in order to visually investigate droplet formation in the free jet flow. Shadows are obtained when the light, focused parallel to the Camera, illuminates the droplet. The light is refracted by the edge of the droplet to draw an image on the Camera film. Short exposure times are required for visualizing the droplets in motion, i.e., droplets moving with the velocity of 100 m/s to transverse a distance of 100 μm during a time interval of 1 μs. This means that exposure times shorter than 1 μs are required in order to obtain sharp images and, hence, light with a wave length in the nano range is usually required according to Hecht [31]. The setup arrangement for visualizing the droplet motion in the free jet flow is presented in Fig. 20.
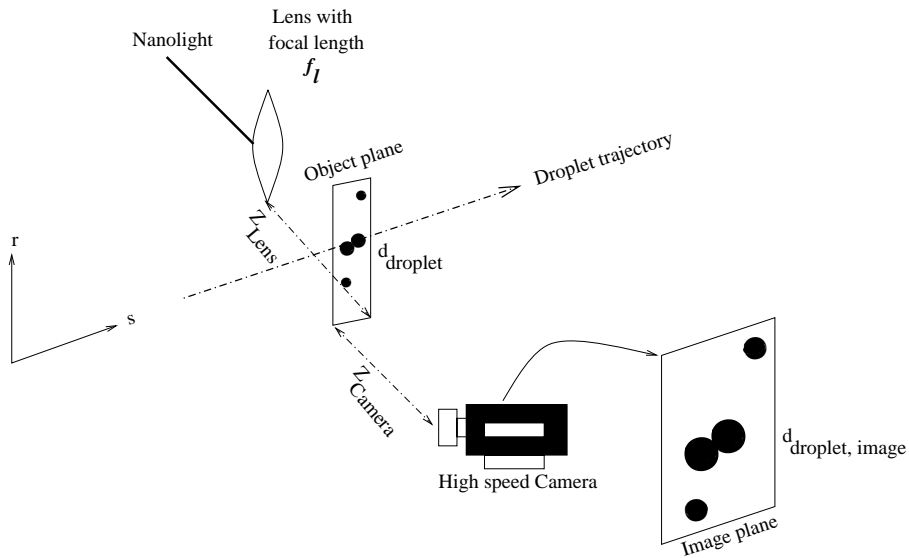
Fig. 20: Setup arrangement for visualizing the droplets motion (droplet dimensions are overscaled)

48

A nano light is focused by lens on a plane where the droplets are to be observed. The observation takes place when a droplet passes through the object plane. With the help of the lens, it is possible to obtain an image of the droplet on the Camera film. The image is then analyzed with an advanced edge detection algorithm to extract the droplet image dimensions. The symbols $d_{droplet}$, $d_{droplet,image}$ are the diameter of the droplet and the tracked image. f_l is the lens focal length with the value of 1000 mm. Z_{Lens}, Z_{Camera} are the azimuthal displacements between the planes of the droplet and the lens, resp., the droplet and the Camera. However, droplets out of the object plane appear as spots of finite size on the film and are not considered. The size of these spots increases when the distance of the droplet from the object plane increases. A high speed Camera allowing visualization rates up to 2000 frame/ s was used to visualize the droplet motion. In the next section, the fluids along with the instruments to measure the liquid physical properties are presented.

4.3 Fluids

The experimental flow conditions were investigated under a stagnation pressure ranging between 2 and 7 bar with the nozzle outlet diameters of 3, 5 and 10 mm. The air to liquid mass flow ratio and the air mass flow qualities are varied between 0.01 and 0.55, resp., 1 % and 46 %. The fluids used in the experiments are air for the gas phase and water, specifically, Newtonian glucose syrup in several concentrations for the viscous liquid phase, Tab. 4.

Fluid 20°C, 1 bar	Concentration [mass %]	Viscosity [mPa s]	Density [kg/m³]	Surface tension against air [mN/m]
Air	–	**0.018**	1.21	–
Water	–	**1**	997	72.6
Glucose Syrup	40.9	**8**	1134	69.5
	70.1	**70**	1227	72.8
	71.8	**100**	1258	71.5
	74.4	**145**	1274	75.9
	80.1	**325**	1328	79.1
	84.2	**760**	1342	79.5

Tab. 4: Fluid properties covered in the experiments normalized to a temperature of 20° C and a pressure of 1 bar

The only disadvantage of the fluids, exhibited with respect to the properties, is that with increasing the liquid viscosity also the density becomes higher. By this the individual effects on the dispersion of two-phase free jet flow can not (yet) be fully separated. The (static) surface tension of the mixtures, on the other hand, does not differ appreciably, so that an effect of this property on the dispersion might be in comparison negligibly small. According to Langner [54], it was concluded that the surface tension forces can be negligibly small, under conditions of high liquid mass flow rate or with substantially poor air mass flow quality, for the two-phase annular flow pattern. In virtue of the experimental apparatus, dispersion experiments were run with a systematic variation of the liquid viscosity, from that of water up to near that of the honey. Aqueous solutions of glucose syrup with mass concentrations, in the range of 41 - 84 %, were used to provide for a wide variation in the liquid viscosity. The experimental apparatus allows for maintaining isothermal flow conditions for the air/ liquid free jet. Hence, the dramatic changes to liquid viscosity, density and surface tension with the temperature are neglected. These physical properties are measured by standard instruments. An overview of the measuring instruments follows next.

Liquid viscosity

A Falling Ball Viscosimeter can measure the viscosity of the aqueous glucose syrup mixtures in the range of 0.5 - 10^5 mPa s. The sphere motion in the sample liquid is transparent, while the dynamic viscosity is determined according to the correlation

$$\eta = K \cdot t \cdot (\rho_{Sphere} - \rho_{Liq}) \qquad ,$$

where η is the dynamic viscosity of the liquid phase. K is the predetermined correlation constant. ρ_{Sphere} and ρ_{Liq} are the sphere and the sample liquid phase density, while t is the measured time that the sphere requires to transverse a definite distance. The liquid density is apparently required for the determination of the liquid viscosity. So, a Pycnometer is implemented to directly obtain the liquid density by the relation

$$\rho_{Liq} = \frac{M_{Pycnometer, Liq} - M_{Pycnometer}}{M_{Pycnometer, ref} - M_{Pycnometer}} \cdot \rho_{ref} \qquad ,$$

where $M_{Pycnometer}$ is the mass of the empty Pycnometer. $M_{Pycnometer, Liq}$ is the mass of the Pycnometer with the sample liquid and $M_{Pycnometer, ref}$ is the mass of the Pycnometer with the reference liquid of the density ρ_{ref}. The reproductive accuracy of the measurements by these instruments is given by $\pm 0.5 \%$.

Surface tension

The static surface tension of liquid against air is measured with the help of a Tensiometer. Fig. 21 shows the principle of the Ring Method Tensiometer. A circular ring is immersed in the liquid phase and is then stretched from the medium with a constant velocity to achieve a balance of the forces exerting on the ring.
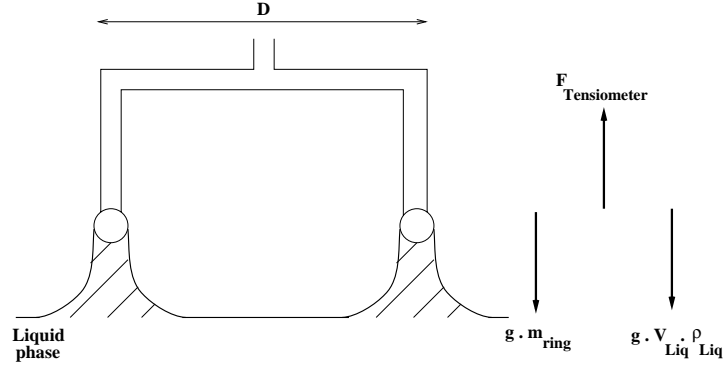
Fig. 21: Principle of Ring Method Tensiometer

The Ring Method Tensiometer accounts for the upward surface tension force, which is proportional to the surface tension of the liquid according to the relation

$$\sigma = \frac{F_{Tensiometer}}{2\pi \cdot D} = \frac{g \cdot (m_{ring} + V_{Liq} \cdot \rho_{Liq})}{2\pi \cdot D} \qquad ,$$

where m_{ring} and D are the mass and the diameter of the ring, while V_{Liq} is the volume of the liquid formed at the interface due to the stretching of the ring from the liquid phase. The volume of the free liquid generally increases when stretching the ring from the medium of higher viscosity, resp., density. Further on, a necking of the free liquid takes place due to the gravity effect on the dense liquid. As a consequence, the free liquid portion is finally disconnected and the ring is released. By this method, the measured values can directly be read from the instrument scale in the units of mN/ m. Accordingly, the measured surface tension of the glucose syrup solutions has a value in excess of that for pure water with increasing the liquid viscosity. The advantages of the Ring Method Tensiometer include the measuring speed and the satisfactory reproductivity within ±0.05 mN/ m.

The consistency of the current experimental conditions with those found in the literature was examined. Fig. 22 shows the air mass flow rate plotted as a function of the liquid mass flow rate, and includes data from by Chen et al. [11] with the liquid viscosity of 1, 8 and 100 mPa s, a nozzle outlet diameter of 10 mm and a stagnation pressure of 3 bar. Obviously, the air mass flow rate decreases as the liquid mass flow rate is increased to achieve the presumed outlet flow

conditions. In general, the data closely follow those from the investigations of Chen et al. [11]. On the other hand, a wide variation in the nozzle flow conditions was applied in the current investigations with respect to that implemented by Chen et al. [11]. By achieving higher liquid mass flow rates, more confidence could be provided for the extrapolation of the experimental results to large scale releases.
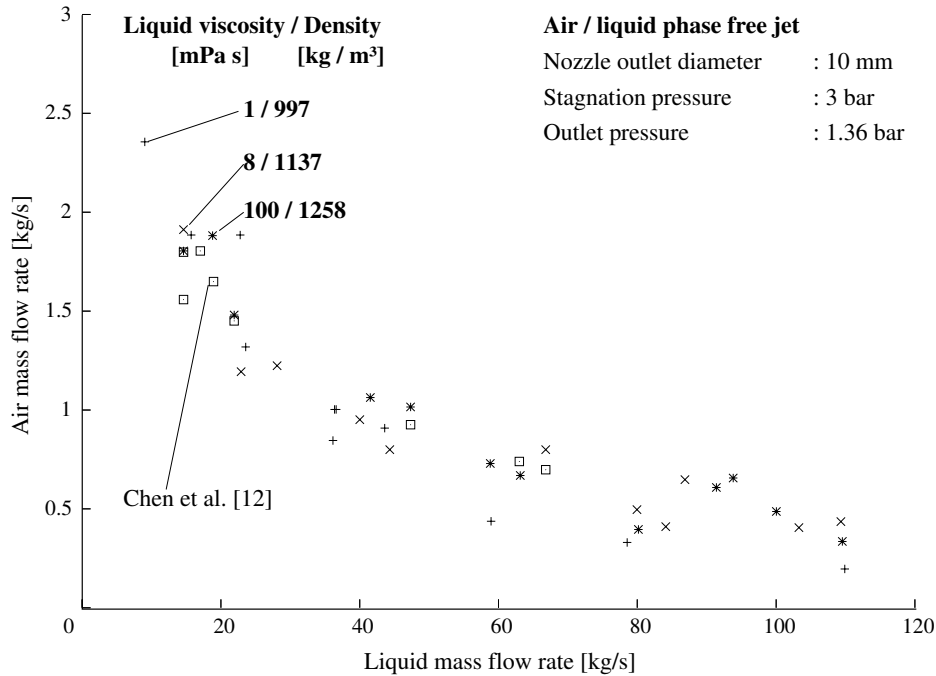
Fig. 22: Air mass flow rate versus the liquid mass flow rate and the data from Chen et al. [11] in case of air/ liquid phase free jet

The flow conditions were varied such that a standard flow pattern inside the nozzle was plausibly kept. This was examined with the help of the flow pattern map by Mandhane et al. [64] for horizontal two-phase flow. Fig. 23 depicts the layout of the experimental conditions on the flow pattern map according to Mandhane et al. [64] for a nozzle diameter of 3, 5 and 10 mm, in case of a two-phase flow of air/ liquid phase with a viscosity of 8 mPa s and a stagnation pressure of 2 bar. Following Mandhane et al. [64] the superficial liquid velocity was plotted against the superficial air velocity.

Obviously, most of the data are located such that the Annular flow pattern will be reasonable with a shift to a Slug flow pattern, particularly, at high liquid flow rate. The data pattern indicates the establishment of a liquid film at the wall while the air fills the central region of the nozzle. Increasing the nozzle diameter reveals the effect of the nozzle geometry. Generally, a transition in the data pattern from the Annular to the Slug regime takes place, since higher amounts of air are required for the establishment of the Annular flow with increasing the liquid flow rate. It can be postulated that the Annular flow pattern is likely to be encountered in the range of current experimental flow conditions. At the nozzle outlet, both phases disperse to

allow for the expansion of the air in the radial and the axial directions, promoting the liquid bulk disintegration into droplets. Based on this finding, it can be simplified that the intensive interactions between the air stream and the main jet flow, within the momentum dominated regime, effectively reduces either the kinetic disequilibrium or the established slip ratio between the mean velocities of the air and the droplet in the jet near field region. Hence, the homogeneous two-phase density and viscosity model are still valid for the calculation of the local jet density and viscosity to an acceptable limit.

<figure>
Nozzle diameter [mm]

Superficial liquid velocity [m/s] (y-axis): 14, 3, 1.2, 0.3, 0.03, 0.003

Regions labeled: Bubble, Slug, Stratified, Wavy, Annular

Superficial air velocity [m/s] (x-axis): 0.03, 0.3, 3, 30, 300
</figure>
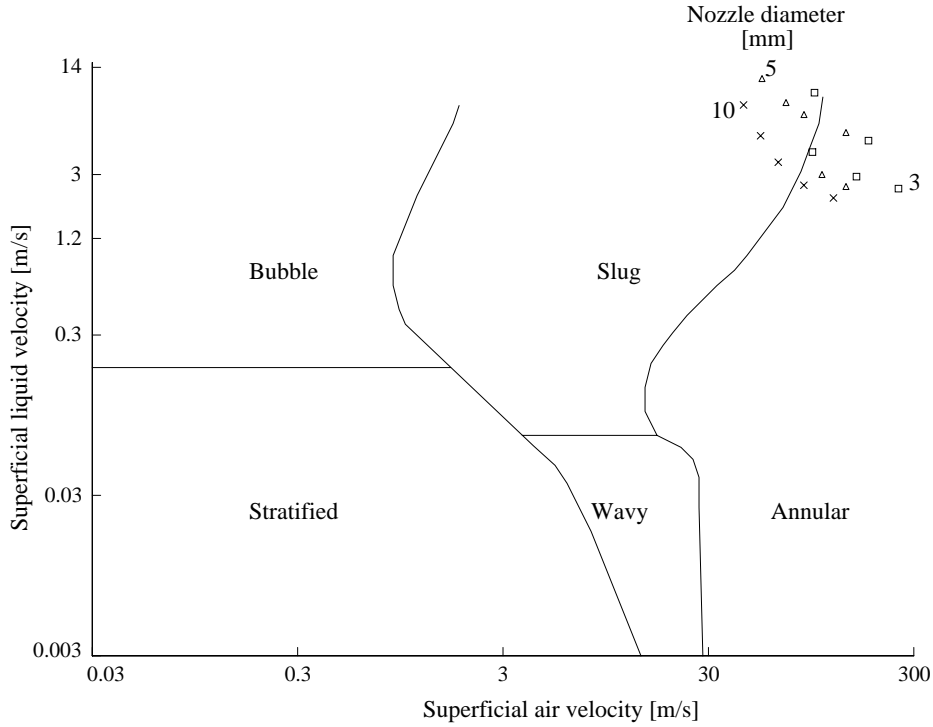
Fig. 23: Layout of the experimental conditions on the flow pattern map according to Mandhane et al. [64] with the nozzle diameter of 3, 5 and 10 mm

By changing the liquid physical properties, the behavior of a momentum dominated air/ water, resp., glucose syrup free jet flow is appeared within the Jet breakup length and the zones of Expansion and Air Entrainment. An illustration is presented in Fig. 24 to shed light on the potential differences in the behavior of the two-phase free jet flows, under almost identical flow conditions but with another liquid viscosity. The left image shows the air/ water free jet and the one on the right is for air/ glucose syrup free jet with a liquid viscosity of 70 mPa s. The jets are established from a nozzle with an outlet diameter of 3 mm. According to the flow pattern map by Mandhane et al. [64] an annular flow pattern at the nozzle outlet is reasonable under these conditions. In this context, a thin film at the jet unbounded periphery still prevails in the Expansion Zone within the Jet breakup length. The jet perimeter apparently increases due to the radial and the axial air expansion in the form of a bell shape in both free jet flows.

The visualizations show that a relatively lower expanding jet flow and a longer breakup length are established for the air/ glucose syrup free jet, which completely disintegrates into liquid droplets within at a distance of 20 mm compared to 13 mm for the air/ water free jet. This may be taken as experimental evidence that the jet flow behavior is sensitive to the liquid phase viscosity. Indeed, the higher liquid phase viscosity will dampen the waves at the liquid surface, leading to less deformation and, therefore, less fragmentation from the liquid bulk can take place. This allows for a lower nominal width of the jet, which remains intact for a longer breakup length. Indeed, the liquid density as well as the surface tension can also be considered as principal dominating factors for jet breakup. Due to the in parallel higher liquid density, i.e., higher inertia along with the superimposed effect of the larger surface tension, the liquid bulk disintegration and the droplet formation will be impeded. In the jet far field region, the generated droplets will be progressively entrained into the air stream and, hence, the air entrainment significantly affects the behavior of the free jet. This entrainment is especially enhanced at a downstream distance of longer than 30 nozzle outlet diameters due to the effect of the co-flowing and the entraining air streams on the two-phase jet flow.

Air/ liquid phase free jet

Nozzle outlet diameter	:3 mm	
Stagnation pressure	:5 bar	
Mass flow rate	:7039 kg/(m² s)	:6640 kg/(m² s)
Mass flow air quality	:5.4 %	:5.6 %
Homogeneous outlet velocity	:86.9 m/s	:80 m/s

Air/ water   **Air/ glucose syrup (70 mPa s)**

Expansion   Air Entrainment $\dot{M}_{Ent}$ (s)

Nozzle

Jet breakup length   :13 mm   **:20 mm**

Fig. 24: Air/ water, resp., glucose syrup free jet flow visualizations

Other potential differences are also deduced in the behavior of the two-phase air/ viscous liquid free jet flows by presenting the experimental data. In the following section, experimental results are presented.

4.4   Experimental results

Measurements of the droplet size and velocity would result, in advances, in understanding the two-phase free jet. The droplet attributes provide the potential to add rather an ample knowledge of the fundamental phenomena established in the free jet flow. The mean droplet diameter is firstly addressed.

4.4.1   Mean droplet diameter

The Sauter droplet diameter, obtained from Phase Doppler Anemometer measurements, is plotted against the air to liquid mass flow ratio in Fig. 25. The parameters are mass flow, liquid viscosity and density for a stagnation pressure of 5 bar at a downstream distance of 30 nozzle diameters.

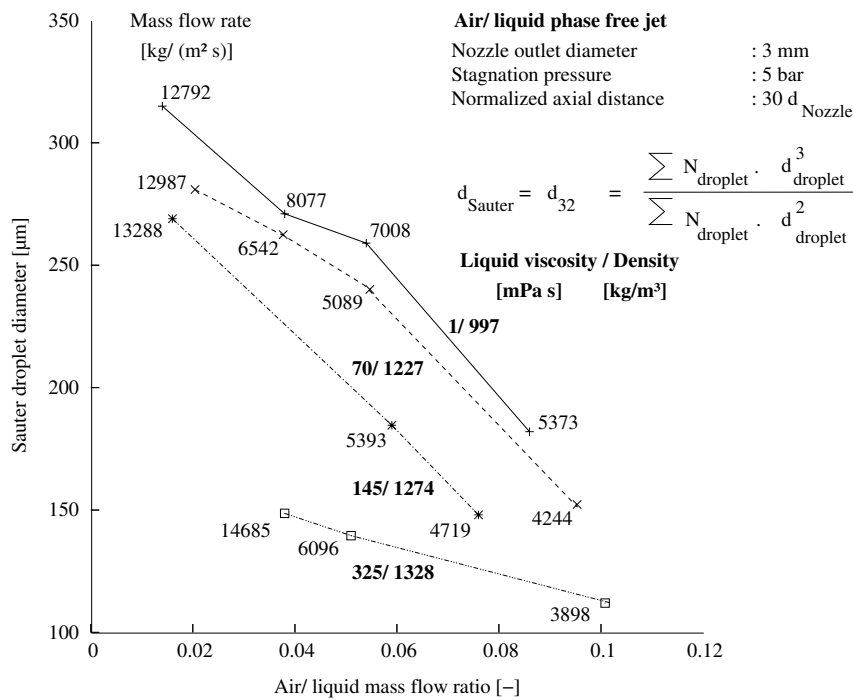**Fig. 25: Experimental Sauter droplet diameter as a function of air to liquid mass flow ratio and liquid viscosity, resp., density at a downstream distance of 30 nozzle diameters with a nozzle outlet diameter of 3 mm**

The Sauter droplet diameter decreases with an increased ratio of air to liquid mass flow. Meaning higher nozzle outlet velocity, almost equal mass flow conditions are maintained. This is

due to the increase of the air impact on the liquid phase, hence, an increase of the aerodynamic forces acting on the liquid causes further disintegration into relatively smaller droplets. The same decrease of the Sauter droplet diameter is also observed when increasing the liquid viscosity, though in this case the liquid density as well as the surface tension are increasing. A higher liquid viscosity than that of water impedes the droplet formation and breakup by reducing the rate of surface perturbations and, consequently, droplet distortions, so that larger fragments prevail. Due to the concomitant higher air impact on the fragments, the liquid bulk allows for further formation of droplets and, hence, a comparatively smaller volume per unit of droplet interface will be established. Consequently, the resulting Sauter droplet diameter is by definition lower. It is apparent that the total mass flow rate follows a trend similar to that of the liquid viscosity on the behavior of the Sauter droplet diameter. By increasing the liquid mass flow rate, the total mass flow rate will become larger, so that fluid dynamic critical flow conditions are established for the two-phase dispersion at almost the same amount of air mass flow rate. Hence, the higher liquid inertia is favoring the formation of droplets with small sizes due to the intensive interactions between both phases at the interface.

In order to examine these trends with other nozzle geometry and different flow conditions, the air to liquid mass flow ratio was varied within the range of 0.01 - 0.55 by virtue of the flow limitations in the experimental apparatus with a nozzle diameter of 10 mm. In Fig. 26, the experimental Sauter droplet diameter is plotted against the air to liquid mass flow ratio. The parameters are the liquid mass flow, liquid viscosity and density and a stagnation pressure of 3 bar at a downstream distance of 30 nozzle diameters.
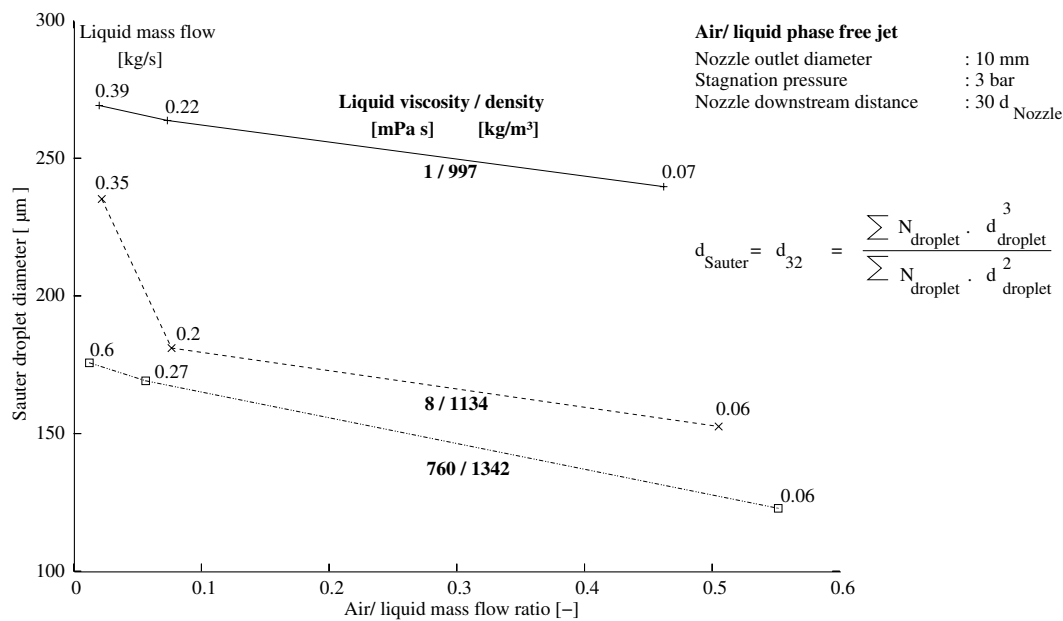

Fig. 26: Experimental Sauter mean droplet diameter as a function of air to liquid phase mass flow ratio and viscosity, resp., density at a downstream distance of 30 nozzle diameters with a nozzle outlet diameter of 10 mm

56

The Sauter droplet diameter decreases with higher air to liquid mass flow ratio, i.e., higher nozzle outlet velocity. This goes along with an increase of the air impact on the liquid phase, keeping almost equal mass flow conditions, hence an increase of the aerodynamic forces acting on the liquid that cause further disintegration into smaller droplets. In particular, the primary breakup of the liquid in the Core region yields fragments that are intrinsically unstable to further deformation as denoted by Faeth et al. [22], Pilch et al. [78] and Walton et al. [106]. The same trend in the behavior of the Sauter droplet diameter is also observed when increasing the liquid viscosity. A higher liquid viscosity than that of water affects the droplet formation and breakup by reducing, resp., damping the rate of surface tension perturbations and, consequently, droplet distortions. This allows for the jet to remain intact for a longer downstream distance breakup length, leading to the formation of droplets with smaller sizes and enhancing the entrainment. This emphasizes the general belief of the combined effects of the air entrainment and of the liquid fragmentation on the local self establishing droplet size distribution.

On changing the liquid viscosity, a variation in the droplet size is straightforward. This will be effectively shown by comparing the droplet size distributions for air and water, resp., viscous liquid phase free jet particularly at specific downstream locations. In Fig. 27, the droplet spectra for a free jet of air and water, resp., glucose syrup with a viscosity of 8 mPa s are presented. The experiments were conducted under almost identical flow conditions and at a downstream distance of 100 nozzle diameters, i.e., in the Similarity region.
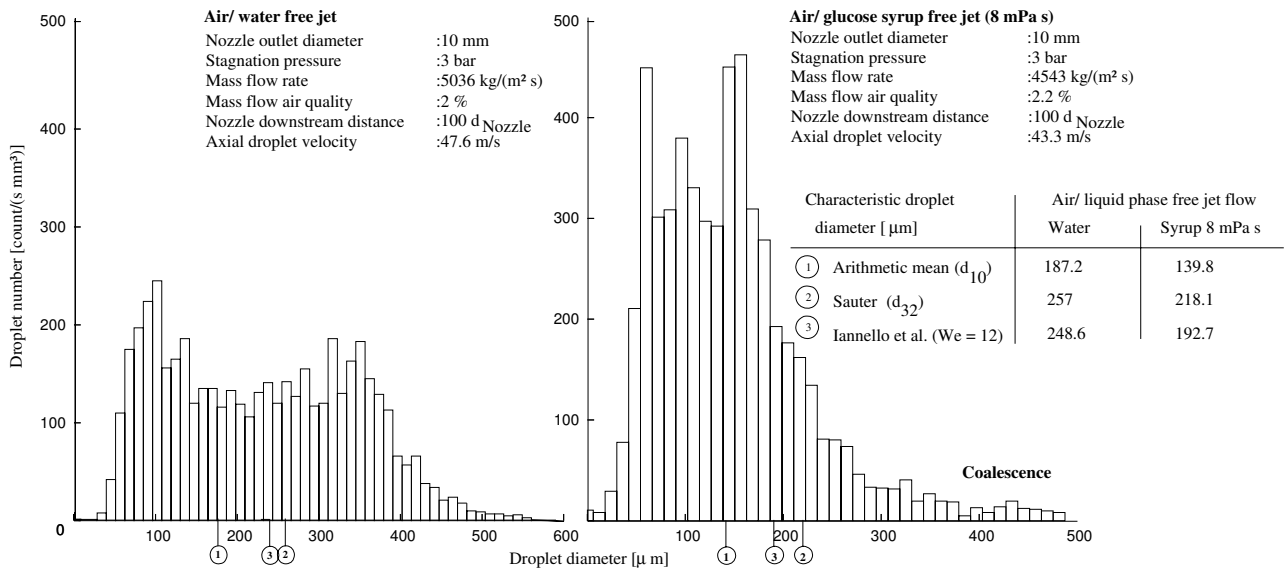

Fig. 27: Experimental droplet spectrum in air and water, resp., glucose syrup free jet with a viscosity of 8 mPa s at a downstream distance of 100 nozzle diameters in case of a nozzle outlet diameter of 10 mm

It is obvious that in both cases bimodal distributions with a relatively long tail are obtained. A comparatively narrow and compact droplet distribution, on the other hand, is seen in the case of the higher viscosity liquid phase. The bimodal type of the droplet spectra might, in the later case, be a mathematical effect. The jet spreads, its boundaries widen with the downstream distance due to the stronger process of air entrainment or higher inertia, and so a lower droplet number density is only detected within the measuring volume. Another possible explanation may be related to the collisions between droplets that may yield coagulation and, hence, the formation of comparatively larger liquid droplets, accompanied with the self establishing of the closer second peak in the droplet distribution. Bach et al. [2] and Bürgermeister et al. [10] also reported such an observation in the droplet size distribution that is enucleating possible droplet coalescence. The representation of the droplet size distribution by the size of the conventionally used characteristic diameters is illustrated in the attached table in Fig. 27, including the arithmetic mean, Sauter mean and maximum stable diameter according to Iannello et al. ($We_{crit} = 12$) for air and water, resp., glucose syrup droplet spectra. Evidently, the characteristic droplet diameter decreases, irrespective of the specific definition, with increasing liquid viscosity, e.g., the resulting value for the arithmetic mean diameter of air and water droplet spectra is 187 μm, while it decreases to a value of about 140 μm for air and glucose syrup droplet spectra with a viscosity of 8 mPa s.

A similar trend in the change of the droplet diameter by increasing the liquid phase viscosity is obtained also in the droplet spectra for air and water, resp., glucose syrup with a viscosity of 100 mPa s, Fig. 28.
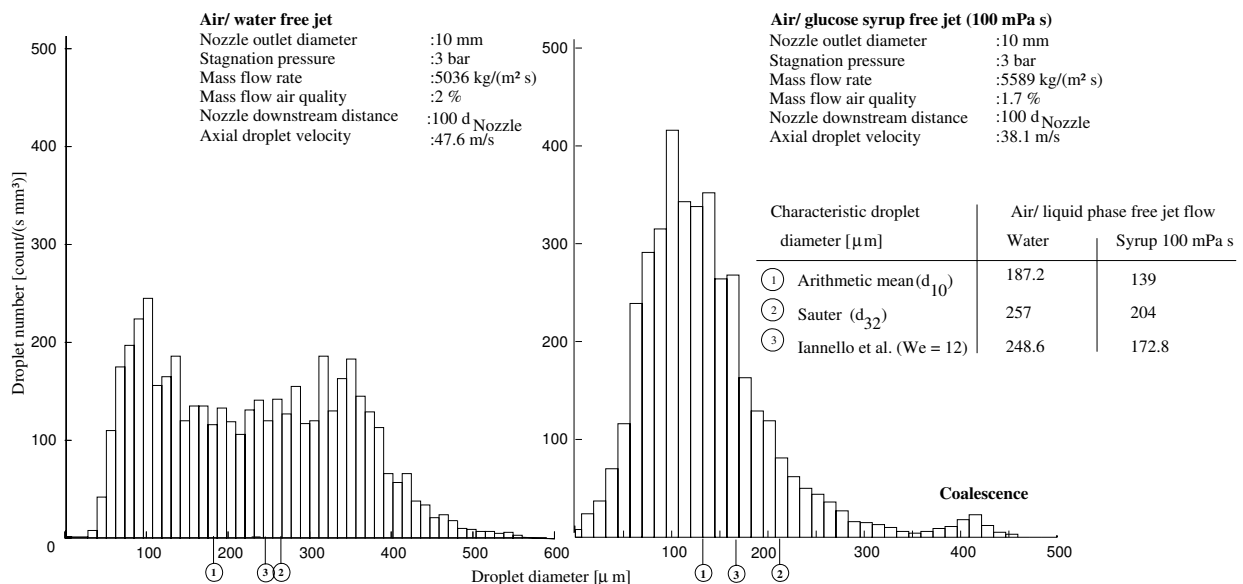

Fig. 28: Experimental droplet spectrum of air and water resp., glucose syrup free jet with a viscosity of 100 mPa s at a downstream distance of 100 nozzle diameters in case of a nozzle outlet diameter of 10 mm

The experiment was again conducted under almost identical flow conditions with a stagnation pressure of 3 bar at a downstream distance of 100 nozzle diameters. The air and water bimodal droplet size spectrum is still as that in Fig. 27. Evidently, the viscous liquid droplet distribution is now only accompanied with the self establishing of a weak second peak. Moreover, a significant number of droplets with diameters of larger than 200 μm are detected in the Similarity region, where the entrained air velocity and the turbulence intensity decreases lower than that at the inception of entrainment, in the region near to the nozzle outlet. Fig. 29 shows the experimental droplet spectrum of air and water, resp., glucose syrup with a viscosity of 760 mPa s under practically identical flow conditions to those in Fig. 27 and 28.
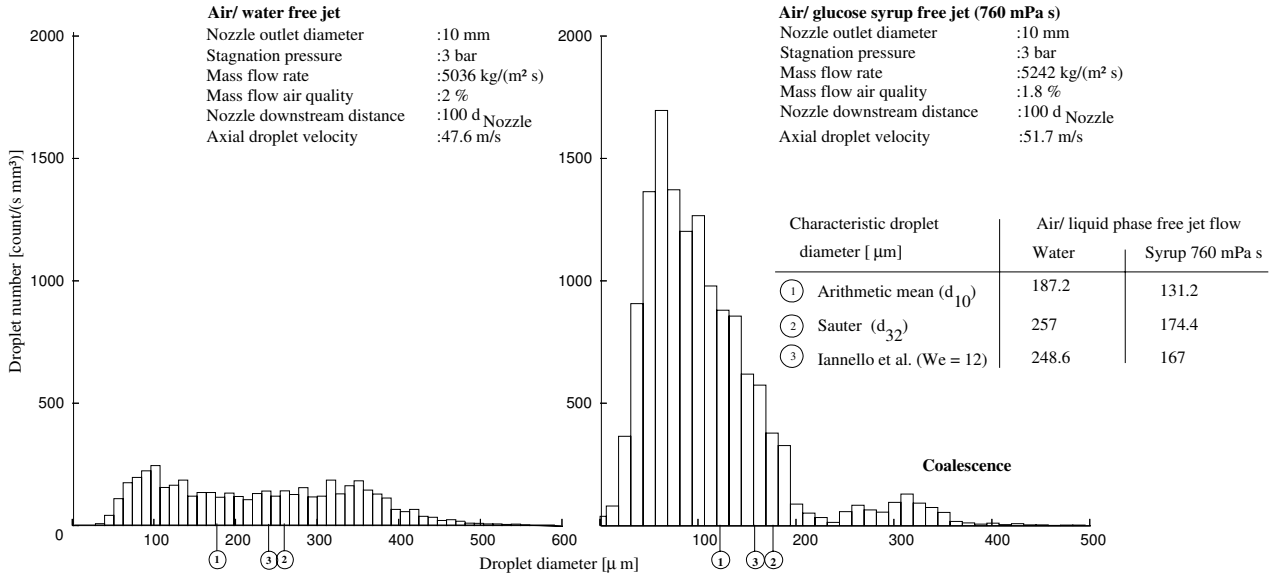
Fig. 29: Experimental droplet spectrum in air and water, resp., glucose syrup free jet with a viscosity of 760 mPa s at a downstream distance of 100 nozzle diameters in case of a nozzle outlet diameter of 10 mm

In principle, the latter findings are confirmed. In total, it can be an indication that the recourse to a mathematical effect in the detection of the droplets is of a minor influence, since larger droplets are obtained with the downstream nozzle distance in the case of air and viscous liquid phase free jet flow. Here, it can be more emphasized the gravity influence on the dispersed droplets, in addition to the interactions between the droplets that are significantly enhanced with the nozzle downstream distance. Generally and as an alternative, it could also be referred to the combined effect of air entrainment and subsequent disintegration as well as possible coalescence of droplets that may produce this specific bimodal droplet size distribution. For substantiation of this hypothesis, jet flow visualizations are presented in the next section.

Jet flow visualization

The droplet distribution characteristics in the case of an air and glucose syrup free jet flow is further clarified by high speed cinematography (2000 frame/ s) in Fig. 30. It includes a left side image for the case of glucose syrup with a viscosity of 100 mPa s for a stagnation pressure of 3 bar, taken at a downstream distance of 100 nozzle diameters. The influence of gravity is observed in comparison with an air and water free jet through a denser distribution of the droplets in the lower jet plane. This is due to the higher density of the glucose syrup when compared to that of water. Obviously, most of the droplets exhibit specific trajectories from the central region towards the jet periphery with different angles. The droplet tracks promote an average inclination angle with a value of about 13°. In this context, they have the possibility to approach each other, compromising droplet collisions between them. Exemplarily, the right side image shows two droplets that are tentatively colliding within a time sequence of 300 μs and a micro distance of 600 μm. The local experimental Sauter mean diameter accounts for a value of 184 μm.

Air/ glucose syrup free jet (100 mPa s)

Nozzle outlet diameter	: 10 mm
Stagnation pressure	: 3 bar
Mass flow rate	: 3906.6 kg/(m² s)
Mass flow air quality	: 4.6 %
Nozzle downstream distance	: 100 d$_{Nozzle}$
Sauter droplet diameter	: 184.1 μm
Homogeneous outlet velocity	: 108.2 m/s

Local droplet velocity : 38.1 m/s
Photo time sequence : 300 μs

13.1°

Jet centerline

13.1°

600 μm

100 d$_{Nozzle}$
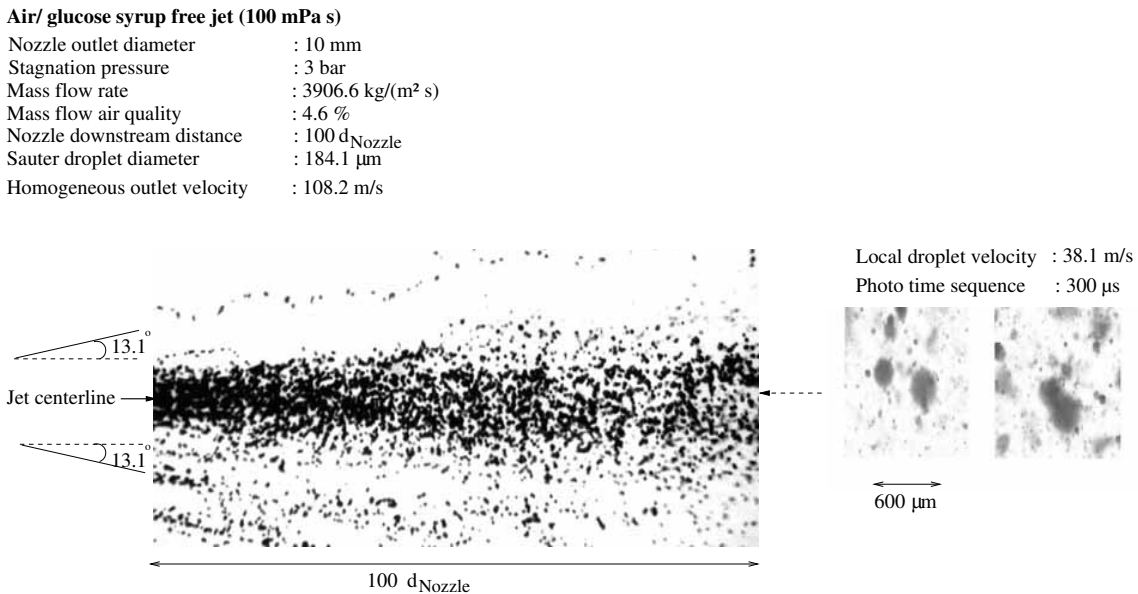
Fig. 30: High speed cinematography (2000 frame/s) of the droplet distribution in horizontal air and glucose syrup free jet flow and droplet collision/ coalescence within a photo time sequence of $300\,\mu s$ **in case of an experimental Sauter mean droplet diameter of** $184.1\,\mu$ **m**

A liquid rim is formed in the gap between the two colliding droplets as they are approaching to each other. Such collisions might promote the coalescence of droplets as well as further downstream again droplet breakup and reformation of smaller individual droplets. Tracking of these two droplets beyond a distance of 600 μm was not possible due to limitations in the experimental apparatus. Nevertheless, it is possible to visualize the outcome of the corresponding collision. With the consideration of a dispersion of mono droplets, the diameter ratio has

a value of unity. Hence the impact parameter, b, according to Ko et al. [47] approaches to a value of 0.45 and the local Collision Weber number converges to a value of 21.3. By plotting this parity value for the impact parameter and the Collision Weber number in Fig. 6, this result supports the hypothesis of coalescence. The relative velocity between these two droplets amounts to a value of 84 m/s, which is comparatively high. Provided that one droplet comes in direct contact with the other, thus, coalescence process will take place as an outcome of this droplet collision. This is compatible with the statement by Schefer et al. [89] and Wygnanski et al. [115] that the flow changes are approaching a self preserving state with the nozzle downstream distance. That is, the turbulence velocity is low such that a surrounding eddy will not separate the droplets from each other. Hence, they coalesce together to form larger droplets. This can be taken also as an experimental evidence of combined effects of the entrainment and the liquid disintegration in the two-phase free jet.

The prediction of the experimental data for the droplet size distribution by the Rosin, Rammler, Sperling and Bennet distribution function are depicted in Fig. 31.

Fig. 31: Experimental cumulative droplet size distribution as a function of droplet size and the prediction by Rosin, Rammler, Sperling and Bennet distribution (RRSB) model at a downstream distance of 30 nozzle diameters

The cumulative droplet size distribution is plotted as a function of the droplet size of air/ glucose syrup with a liquid viscosity of $70\,\mathrm{mPa\,s}$ and a stagnation pressure of 5 bar at a downstream

distance of 30 nozzle diameters. The parameter is the exponent of the distribution function. The experimental data imply a relatively narrow droplet size distribution by establishing a value of 181 μm for the mean droplet diameter and 240 μm for the Sauter droplet diameter. Within this downstream distance, the aerodynamic effects are still significant on the droplet deformation and, hence, a relatively large number density of small droplets is expected. On the other hand, the droplet with large diameters in excess of 350 μm will be subject to further breakup. The experimental droplet size distribution is shown to be reasonably predicted by RRSB function with an exponent of 1.3 for the experimental droplet range characterized by the Sauter droplet diameter. Meanwhile the predictions of the small droplets, diameter less than 100 μm are not substantiated by the size distribution function.

The predictions by RRSB function were also examined for the droplet size distribution established in the downstream distance. Fig. 32 shows the cumulative droplet size distribution as a function of the droplet size for the air/ glucose syrup free jet flow under identical flow conditions as indicated in Fig. 31, but here for a downstream distance of 100 nozzle outlet diameters.
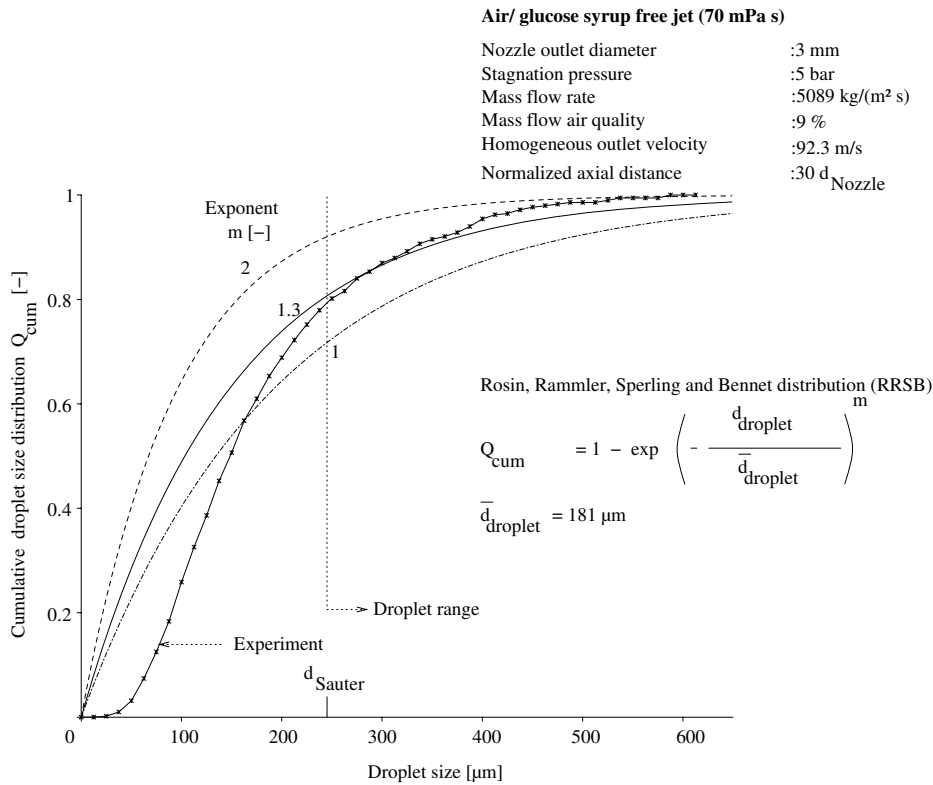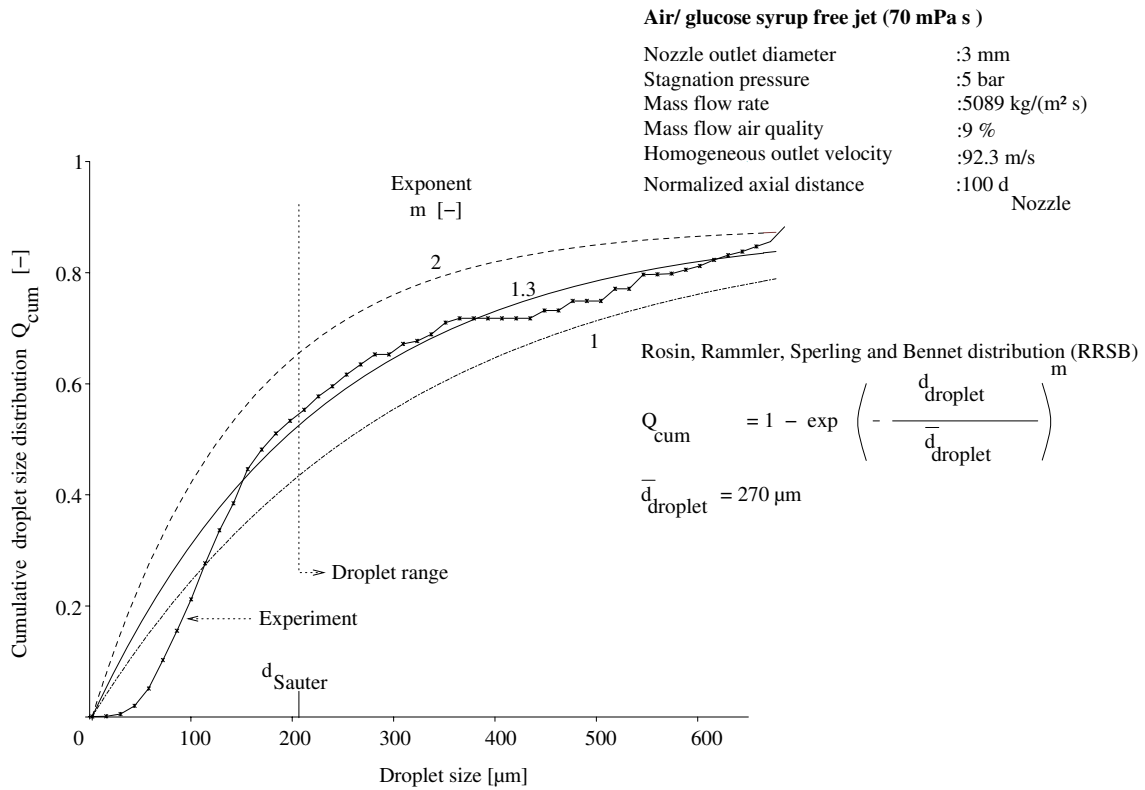

Fig. 32: Experimental cumulative droplet size distribution as a function of droplet size and the prediction by Rosin, Rammler, Sperling and Bennet distribution (RRSB) model at a downstream distance of 100 nozzle diameters

The experimental data result in a mean droplet diameter of 270 μm and 210 μm for the Sauter droplet diameter. In comparison to the experimental data presented in Fig. 31, this variation in the characteristic droplet diameter can be explained due to the collisions between the

droplets that lead to coalescence and, hence, to the formation of large droplet diameter. The reproduction by RRSB function confirms that the value of 1.3 for the exponent properly predicts, to a relatively wider range of the droplet size, the experimental droplet size distribution. Jet spreading with the downstream distance results in reducing the droplet number density. As a consequence the droplet collision probability may be reduced and, hence, finally prompts the formation of relatively smaller droplet sizes. On the other hand, the turbulence intensity achieves a self constituting state with the downstream distance, thus, a decrease in the relative velocity between the droplet and the air flow field is established. This in turn reduces the aerodynamic forces and the droplet breakup frequency, ultimately leading to the formation of relatively larger droplet sizes that are then affected by the gravitational forces to a greater extent, ultimately leading to the droplet rain out in the jet flow.

Based on the theoretical approaches advocated by Ko et al. [47] and Kollár et al. [49], with regards to the energy conservation concept applied for the droplet formation and the collisions, these two-counteracting tendencies must be in balance at each downstream distance establishing a droplet size distribution, which can be reproduced by a standard distribution function. Subsequently, it can be concluded that the RRSB model with the exponent of 1.3 is important in the prediction of the droplet size distribution, irrespective of the downstream distance and of the variation of the characteristic droplet diameter due to the associated phenomena like droplet collisions, break up and rain out. These phenomena, in this context, have also an influence on the mean droplet velocity. This topic is presented in the next section.

4.4.2 Mean droplet velocity

In Fig. 33, the mean droplet velocity is plotted against the radial and axial distance in case of a liquid viscosity of 100 mPa s, at a stagnation pressure of 2 bar and a mass flow air quality of 3.2 %. It can be seen that the velocity distributions in the radial direction, for the Core/ Transition as well as Similarity region, relax to an almost symmetric bell-shaped velocity profile as in single-phase gas free jet flows. A maximum value for the droplet velocity is achieved at the jet centerline as expected. It then monotonically starts to decrease in the direction towards the jet periphery approaching asymptotically a value of zero. The flow fluctuations can significantly intercede a shift in the local velocity distribution, e.g., as it is manifested in the distribution of the measured velocity at axial distances of 750, 1000 and 1400 mm. In the domain of these spatial distances from the nozzle outlet, the aerodynamic forces do not significantly affect the droplet trajectory as within the Core/ transition region, but other influential forces are actually more dominant like the gravitational forces.

As an example, a comparison of the local droplet Reynolds number calculated for air and water, resp., high viscosity liquid phase free jet has been investigated. The increase of the liquid phase viscosity is accompanied with a higher density and, hence, the individual effect on the disper-

sion of air and liquid phase free jet can not yet be incontestably separated. Nevertheless, an attempt for explanation is made by using the Reynolds number as a dimensionless parameter. Droplet Reynolds number is presented in the next section.
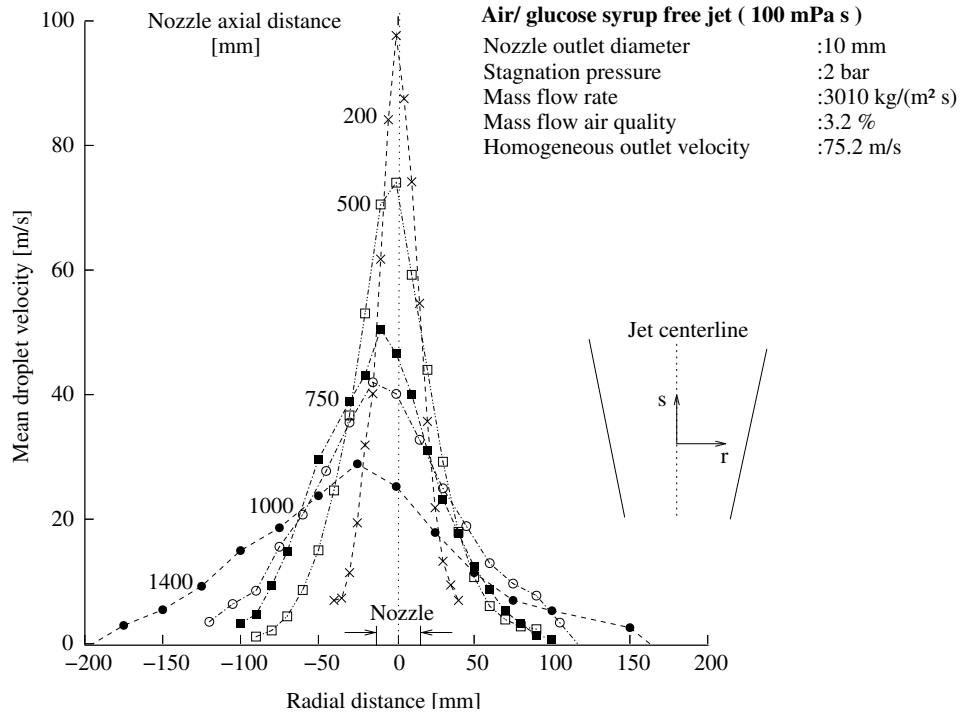
Fig. 33: Mean droplet velocity as a function of the radial and axial distances in case of air/ glucose syrup free jet with a liquid viscosity of 100 mPa s

Droplet Reynolds number

In Fig. 34, the droplet Reynolds number and the experimental Sauter droplet diameter are plotted versus the normalized axial distance in case of air and water, resp., liquid phase with a viscosity of 70 and 325 mPa s. The other flow parameters are a stagnation pressure of 7 bar, a nozzle outlet diameter of 3 mm and a mass flow air quality of 5 %. The droplet Reynolds number is calculated based on the experimental centerline velocity and Sauter diameter. In general, the Reynolds number initially increases slightly with the axial distance of up to 30 nozzle diameters.

A flat maximum is then established, while with the further nozzle downstream distance, the Reynolds number decreases approaching a self constituting value. The droplet Reynolds number ensures the competition between the inertial and the viscous forces. An increasing Reynolds number means that the inertial forces become more relevant for the droplet behavior. Indeed, the competition between both forces occurs along the nozzle downstream distance. Despite the lower level of turbulence intensity in the far downstream, resp., Similarity region, the considered droplets exhibit sufficient inertia to establish a self constituting value for a droplet Reynolds number. A higher liquid viscosity causes smaller droplets to be produced, consequently lower

64

inertial forces and, hence, generally lower Reynolds number are obtained in comparison with the local droplet Reynolds number calculated for air/ water free jet.
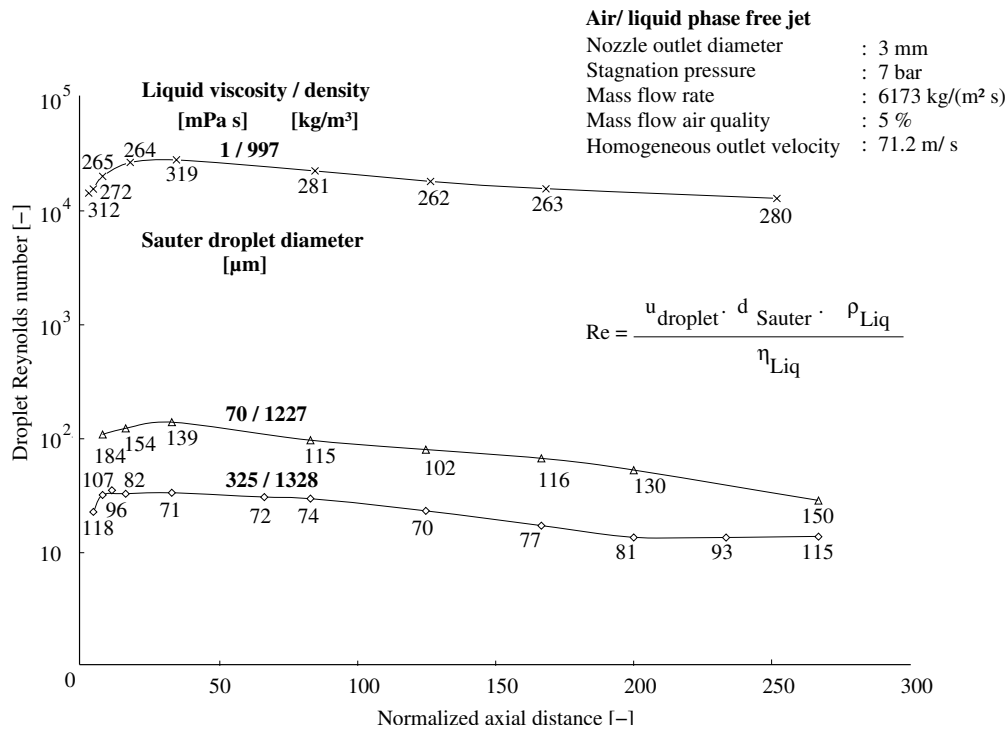
Fig. 34: Experimental droplet Reynolds number based on centerline velocity and Sauter mean droplet diameter as a function of the normalized axial distance in case of air and liquid phase free jet

The droplet Reynolds number behavior confirms that the droplets are subject to external flow fluctuations establishing a self preserving state with the nozzle downstream distance. Within this jet far field region, the gravitational effects are already significant on the droplet velocity profiles in the free jet flow of air/ higher viscosity, resp., density liquid phase than that of water, by interceding an apparent shift in the droplet trajectories. A portion of the dispersed droplets will rain out. The droplet rain out is presented in the next section.

4.4.3 Droplet rain out

Fig. 35 depicts the dimensionless droplet rain out capture plotted as a function of the patternator azimuthal location and normalized axial distance for an air/ water free jet flow with a nozzle diameter of 5 mm, a stagnation pressure of 3 bar and air mass flow quality of 46.2 %. The numbers from one to eight represent the collecting flasks and their azimuthal location with respect to the nozzle. Incidentally, the two-phase free jet flow is established at the azimuthal location coinciding with flask number four. Within a downstream distance of 900 nozzle diameters, the jet completely losses the momentum to the ambient, resulting in total droplet rain

out. Obviously, the maximum droplet rain out collection is obtained in the central region of the jet flow and decreases toward flask numbers one and eight. This indicates that the droplet distribution in the free jet flow is more intensive in the central region in relative to that at the jet periphery. The lack of symmetry in the droplet rain out distribution, at a specific normalized axial distance, could have an indication of the adverse effect of the entrainment on the dispersed droplet and, hence, the jet flow structure. Droplets are also subject to collisions with frequent coalescence along the nozzle downstream distance to encounter an asymmetry in the droplet distribution. It can be concluded that the nozzle flow conditions and the established air vortical structures, interacting with the main jet flow, are important parameters for predicting droplet rain out. Analytical investigations presented in the next chapter.
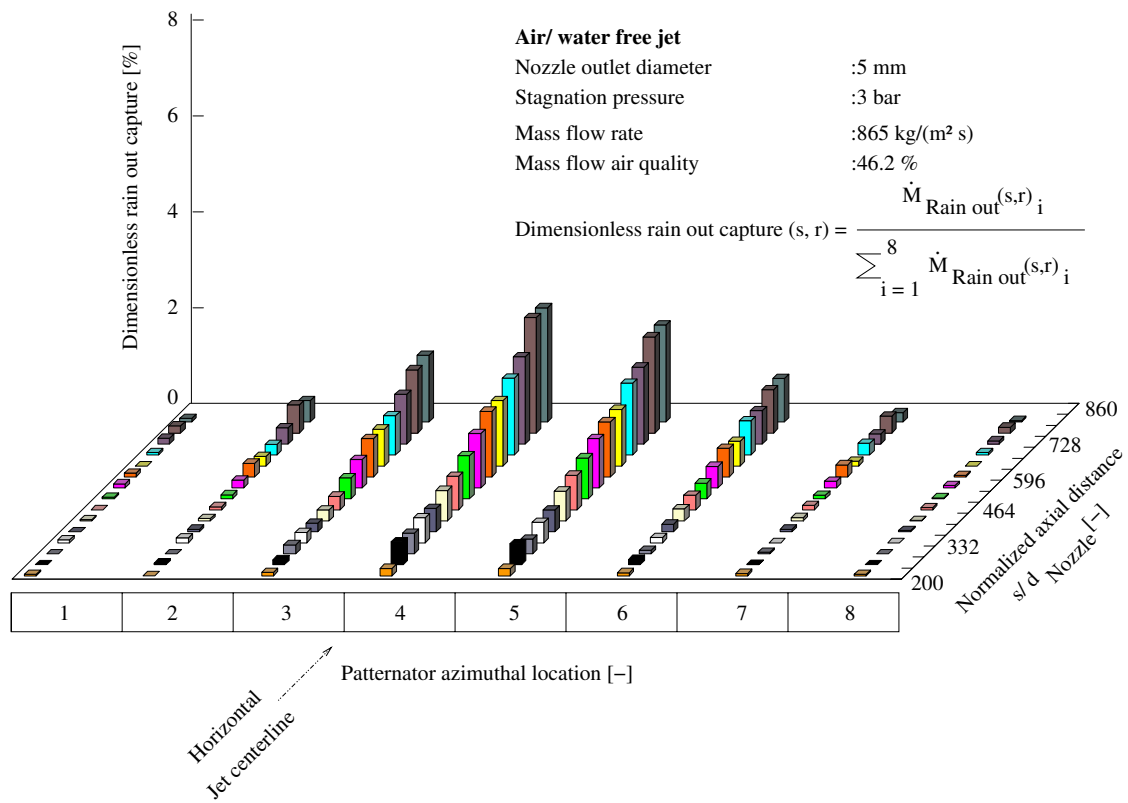
Fig. 35: Dimensionless droplet rain out capture in a horizontal air/ water free jet flow as a function of the patternator azimuthal location and normalized axial distance

5 Analytical investigations

This chapter focuses on the derivation of the main trends of droplet behavior in two-phase free jet flows. Furthermore, the correlations of the proposed model to predict the characteristics of two-phase free jet flow in case of air/ viscous liquid free jet flow are presented.

5.1 Proposed model of free jet characteristics

5.1.1 Droplet rain out

At specific conditions depending on the local droplet size and velocity distribution, some of the droplets will remain airborne within the two-phase jet flow, while others will rain out. In Fig. 36, the characteristics for the droplet rain out modelling are depicted.
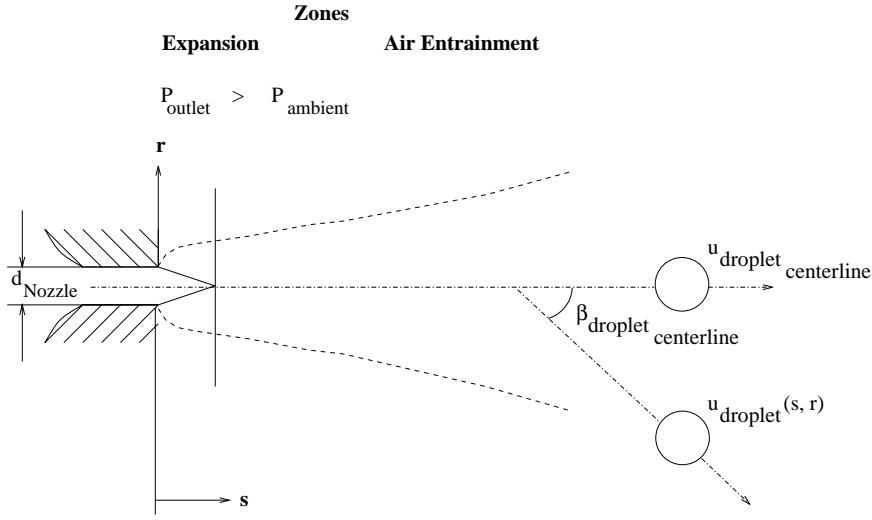
Fig. 36: Droplet rain out characteristics in two-phase jet flow according to Havens et al. [30] (droplet size is overscaled)

It is assumed that a droplet moves, in view of the competition of the inertial and the gravitational forces, in a trajectory with an inclination angle of $\beta_{droplet_{centerline}}$ with respect to the jet centerline. The half jet width angle, $\beta_{0.5}$, characterizes the ideal dispersion of the jet and is related to the entrainment of air from the ambient. These characteristic angles are defined as

$$tan\,\beta_{droplet_{centerline}} = \frac{u(s,r)}{u_{droplet_{centerline}}} \quad , \quad tan\,\beta_{0.5} = C_{Ent,\,2ph} = \frac{\dot{M}_{Air}(s)}{\dot{M}_{Liq}}$$

The condition for the rain out, based on the trajectories analysis of the droplets with respect to the jet flow, is achieved when the inclination angle is larger than the half jet width angle

$$\beta_{droplet_{centerline}} > \beta_{0.5}$$

By this, the effect of gravity with respect to the droplet inertia is high enough to force the droplet out of the jet flow boundaries so that the droplet starts to fall freely. An approach is proposed including the entrainment feature and, hence, the effect of the air entrainment on the droplet velocity. This predictive model for the droplet rain out reads

$$f_{cum}|_{s/d_{Nozzle}} = \frac{\beta_{droplet_{centerline}}}{\sum \beta_{droplet_{centerline}}|_{s/d_{Nozzle}}} = \frac{arctan\left(u(s,\,r)/u_{droplet_{centerline}}\right)}{\sum arctan\left(u(s,\,r)/u_{droplet_{centerline}}\right)|_{s/d_{Nozzle}}}$$

In this context, it should be noted that because the turbulence intensity decreases with the nozzle downstream distance, a droplet which remains initially airborne can rain out further downstream. This characteristic must, therefore, be taken into account in the predictive model, e.g., by using the centerline droplet velocity as reference for droplet rain out. The centerline droplet velocity modelling will be presented next.

5.1.2   Centerline droplet velocity

The following implicit assumptions have been made in modelling the centerline droplet velocity in case of a horizontal jet flow: the shape of the droplets is spherical, the spatial gradients of the steady air velocity field around the droplet as well as the liquid bulk are negligibly small, since there are no external forces from the surrounding to alter them. The shear stress exerted by the air is equal around a droplet and, hence, no rotation or internal oscillation at the interface occurs. Furthermore, the two-phase free jet exhibits enough momentum that the gravity and the buoyancy forces are of minor effects on the motion of the droplet in a near nozzle downstream distance. Otherwise, these forces will be admittedly considered in case of an inclined or a vertically oriented free jet flow.

The differential equation of motion for a single droplet in the jet axial flow direction under the influence of the aerodynamic forces in the case of a uniform and an isothermal air flow field then follows

$$m_{droplet} \cdot \frac{du_{droplet}}{dt} = 3\pi \cdot \eta_{Air} \cdot d_{droplet} \cdot (u_{Air} - u_{droplet}) + \frac{\pi}{12} \cdot \rho_{Air} \cdot d_{droplet}^3 \cdot \left(\frac{du_{Air}}{dt} - \frac{du_{droplet}}{dt}\right)$$

$$+\frac{3\sqrt{\pi}}{2} \cdot d_{droplet}^2 \cdot \sqrt{\rho_{Air} \cdot \eta_{Air}} \int\limits_{0}^{t} \frac{\left(\frac{du_{Air}}{dt} - \frac{du_{droplet}}{dt}\right)}{\sqrt{t-\tau}} dt + \frac{\pi}{6} \cdot \rho_{Air} \cdot d_{droplet}^3 \cdot \frac{Du_{Air}}{Dt}$$

$$+\frac{\pi}{6} \cdot d_{droplet}^3 \cdot g \cdot (\rho_{Liq} - \rho_{Air}) \quad \text{with} \quad m_{droplet} = \frac{\pi}{6} \cdot \rho_{Liq} \cdot d_{droplet}^3 \quad,$$

where Du_{Air}/Dt is the substantial acceleration of the air field around the droplet. The first term on the right side is the steady-state drag as described by the viscous Stokes law. The next term refers to the so called added mass and accounts for the air inertia in the droplet boundary layer when pushed away by the droplet. It is negligibly small compared to the terms magnitude when the air density is small compared to that of the liquid, which usually has a relatively higher density. The third term is the so called Basset history force, which corrects for temporal variations in the relative velocity, since the droplet velocity can not respond immediately to the changes in the air velocity without a time lag, τ. Following Frohn et al. [26], Knubben [45] or Sirignano [93], this force is lower by an order of magnitude compared to the viscous drag term. So the Basset history force contributes little and can also be disregarded. The fourth term accounts for the force on the droplet created by the radial variations in the viscous stress. The effect of this term will be discarded in view of the implicit assumption of an equal shear stress at the air-liquid interface. The last term represents the net effect of buoyancy and gravity on the droplet, which also will be negligibly small since the jet is assumed to exhibit enough momentum to overcome the effects of these two forces. Along with these simplifications, the equation of motion is reduced to a linear differential equation and reads

$$\frac{du_{droplet}}{dt} = \phi \cdot (u_{Air} - u_{droplet}) \quad \text{with} \quad \phi = 18 \cdot \frac{\nu_{Air}}{d_{droplet}^2} \cdot \frac{\rho_{Air(P_{ambient})}}{\rho_{Liq}} \quad ,$$

where ϕ here is a characteristic time constant. It is related to the ambient air physical properties and is inversely proportional to the liquid density as well as to the square of the considered (characteristic) droplet diameter.

The solution for this equation, on applying the boundary conditions of the initial mean velocities of the air and of the droplet established at the nozzle outlet, can be written in the form

$$u_{droplet_{centerline}} = u_{Air} \cdot (1 - exp(-\phi t)) + u_{Nozzle} \cdot exp(-\phi t) \quad \text{with} \quad u_{Nozzle} = \frac{\dot{M}_{Total\,(Nozzle)}}{\rho_{Nozzle} \cdot A_{Nozzle}}$$

The solution is apparently composed of two contributions. The first component refers to the centerline droplet velocity, which would attain the air velocity in a relatively long time interval. The second term accounts for the initial droplet velocity represented by the nozzle outlet velocity which decays progressively. In this context, Michaelides [69] stated that this equation for the droplet motion within an air stream of different density can be too ambiguous for the description of the centerline droplet velocity as a function of the time domain, since the motion of the droplet has two time scales of short and long time intervals. These were considered by Michaelides [69] to account for the kinematic irreversibilities in the force exerted by the air stream on the droplets. Thus, an asymptotic solution for the total aerodynamic force at short

and long time intervals after the onset of droplet motion is derived in the Laplace domain by using standard methods of analysis. The equation of droplet motion according to Michaelides [69, 70] reads

$$m_{droplet} \cdot \frac{du_{droplet}}{dt} = \frac{\pi}{6} \cdot d^3_{droplet} \cdot g \cdot (\rho_{Liq} - \rho_{Air}) + \frac{\pi}{6} \cdot \rho_{Air} \cdot d^3_{droplet} \cdot \frac{Du_{Air}}{Dt}|_{Y(t)} + F_{Total} \quad ,$$

$$F_{Total} = 3\pi \cdot \eta_{Air} \cdot d_{droplet} \cdot (u_{Air}(Y(t), s) - u_{Nozzle}(s)) \cdot \left[\frac{\lambda_{Air}}{9} + \lambda_{Air} + 1 - \right.$$

$$\left. \frac{(\lambda_{Air} + 1)^2 \langle [\lambda^3_{droplet} - \lambda^2_{droplet} \tanh(\lambda_{droplet}) - 2f(\lambda_{droplet})] \frac{\eta_{Liq}}{\beta \cdot d_{droplet}} + f(\lambda_{droplet}) \rangle}{[1 + \frac{\eta_{Air}}{\beta \cdot d_{droplet}}(\lambda_{Air} + 3)][\lambda^3_{droplet} - \lambda^2_{droplet} \tanh(\lambda_{droplet}) - 2f(\lambda_{droplet})] \frac{\eta_{droplet}}{\eta_{Air}} + (\lambda_{Air} + 3)(f(\lambda_{droplet}))} \right]$$

$$\text{with} \quad \lambda_{Air} = \sqrt{\frac{s \cdot d^2_{droplet}}{\nu_{Air}}} \quad , \quad \lambda_{droplet} = \sqrt{\frac{s \cdot d^2_{droplet}}{\nu_{droplet}}} \quad , \quad f(\lambda_i) = (\lambda_i^2 + 3)\tanh(\lambda_i) - 3\lambda_i$$

Here, the index i is assigned to the air, resp., the droplet. The function $Y(t)$ refers to the transformation parameter of the short time scale in the Laplace domain. β denotes the slip coefficient in the Basset history force and is defined by the ratio of the shear stress to the slip velocity at the surface of the droplet. λ_i is the dimensionless length scale of the air and the droplet in the Laplace domain.

With respect to the proposed model and following Clift [13], Frohn et al. [26], Knubben [45], Sirignano [93] or Yarin [116], the Basset history force was omitted since the time scales considered by Michaelides et al. [70] are shorter than these normally required to run the droplet velocity measurements. Instead, it is postulated that the motion of the droplet takes place under steady state conditions. With this simplification, the equation of droplet motion can be reformulated considering the spatial domain represented by the nozzle downstream distance instead of the time domain. The nozzle downstream distance travelled by a single droplet can be determined according to Vogel [104] and reads

$$s = \frac{1}{2} \cdot a \cdot t^2 \quad \text{with} \quad a = \frac{3}{4} \cdot C_{drag} \cdot \frac{\rho_{Air(P_{ambient})}}{\rho_{Liq}} \cdot \frac{u^2_{rel_{Nozzle}}}{d_{droplet}} \quad \text{for} \quad 12 < We < 50 \quad ,$$

$$We = \frac{\rho_{Air(P_{ambient})} \cdot d_{droplet} \cdot u^2_{rel_{Nozzle}}}{\sigma} \quad \text{and} \quad C_{drag} = 1.7$$

where a is the acceleration given by Lovalenti et al. [59] or Pilch et al. [78] with respect to the droplet creation analysis. In Fig. 37, the liquid breakup by shearing in case of a liquid jet core and the viscous drag force exerted on the droplet are presented for this analysis. It is

assumed that the droplet is finally segregated from the liquid jet core and is then immediately susceptible to the expansion of the co-flowing air that acts as the initial exerting force on the segregated droplet, then to the deceleration due to air entrainment from the ambient. For the case of an inviscid liquid the fastest growing Rayleigh-Taylor instability wavelength is claimed to be responsible for the formation of droplets under the acceleration condition. The drag coefficient C_{drag} amounts, according to Pilch et al. [78], to a value of 1.7 in the case of an incompressible liquid and air velocity head based on the relative velocity between that of the air and that of the droplet.
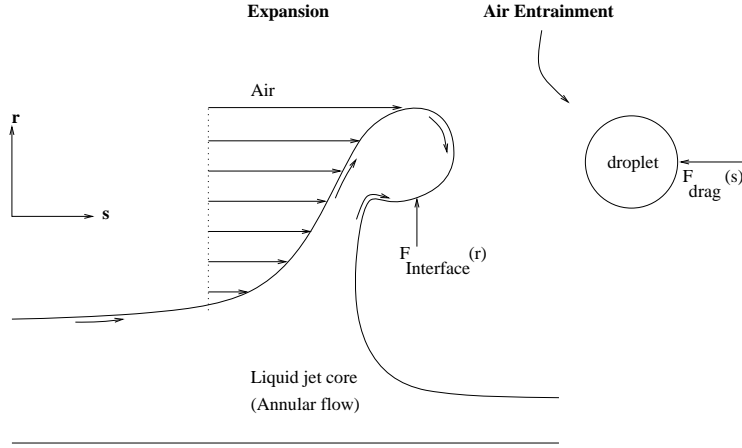
Fig. 37: Liquid breakup by shear process and forces exerted on established droplet

The centerline droplet velocity is finally given by

$$u_{droplet_{centerline}}(s) = u_{Air} \cdot \left(1 - exp \left(-22.5 \cdot \frac{\nu_{Air} \cdot \left(\frac{\rho_{Air(P_{ambient})}}{\rho_{Liq}} \right)^{0.5}}{d_{droplet} \cdot u_{rel_{Nozzle}}} \cdot \left(\frac{s}{d_{droplet}} \right)^{0.5} \right) \right) +$$

$$u_{Nozzle} \cdot exp \left(-22.5 \cdot \frac{\nu_{Air} \cdot \left(\frac{\rho_{Air(P_{ambient})}}{\rho_{Liq}} \right)^{0.5}}{d_{droplet} \cdot u_{rel_{Nozzle}}} \cdot \left(\frac{s}{d_{droplet}} \right)^{0.5} \right)$$

The first term mirrors the pressure drag with an overproportional acceleration that is dominant in the jet near field region, while the second one is the friction drag with a further overproportional deceleration in the jet far field region. The steady state behavior of the droplet under the superimposed effects of acceleration and deceleration have also been stated by Cohen [14], Faeth et al. [22], Kolev [48] and Van de Sande et al. [101].

It would appear that the self establishing droplet diameter is a characteristic input parameter for the centerline droplet velocity prediction. According to Teng et al. [97], the droplet may have a size similar in magnitude to that of the nozzle outlet diameter. Due to this, here, in

the expression for the centerline droplet velocity, the dimensionless downstream distance can be related to the nozzle outlet diameter. Moreover, the nozzle downstream distance variable is adjusted to include the virtual origin distance in order to adequately fit the experimental data. The virtual origin indicates graphically the nozzle downstream distance, where mathematically no air or ambient gas entrainment is considered in view of the air expansion. The formula proposed by Pitts [79] suggests that the dimensionless virtual origin is a function of the nozzle Reynolds number following an exponential trend. It reads

$$\frac{s_{virtual}}{d_{Nozzle}} = 4.3 \cdot (Re_{Nozzle})^{0.097} \quad \text{with} \quad Re_{Nozzle} = \frac{4 \cdot \dot{M}_{Total(Nozzle)}}{\pi \cdot d_{Nozzle} \cdot \eta_{Nozzle}} \quad ,$$

$$\eta_{Nozzle} = 1 / \left(\frac{\dot{x}_{Air(Nozzle)}}{\eta_{Air(P_{ambient})}} + \frac{1 - \dot{x}_{Air(Nozzle)}}{\eta_{Liq}} \right) \text{ and } \dot{x}_{Air(Nozzle)} = \dot{M}_{Air, Nozzle} / \dot{M}_{Total(Nozzle)} > 0 \,,$$

whereby the so called homogeneous two-phase flow viscosity is introduced in the calculation of the nozzle Reynolds number.

Based on experimental data as well as those by Malmström et al. [63] and Surma [96], Fig 38 depicts the related virtual origin plotted as a function of the nozzle Reynolds number. It shows that the jet virtual origin would take negative values in the case of experiments with low mass flow quality, $\dot{x}_{Air(Nozzle)}$ of less than 2 %.

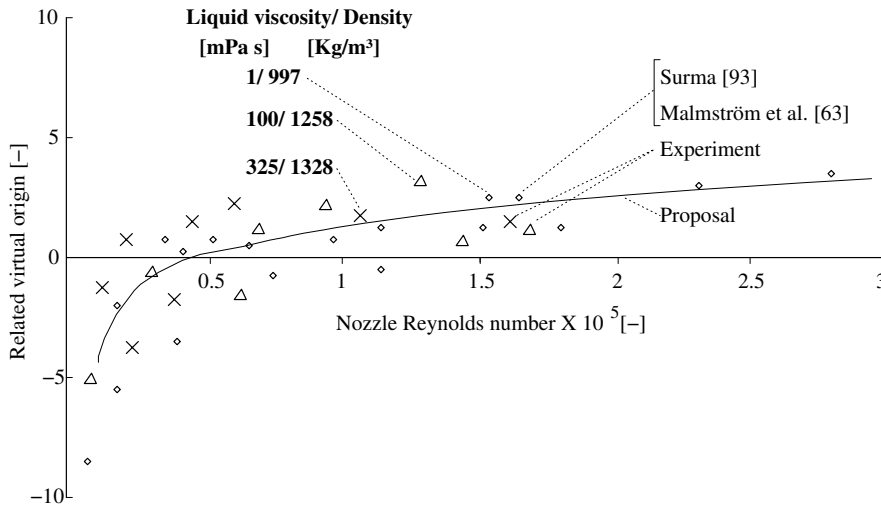**Fig. 38: Related virtual origin as a function of the nozzle Reynolds number based on experimental results and data by Surma [96] and Malmström et al. [63]**

For this reason, a logarithmic dependency was proposed and the numerical constants for this expression were determined by applying the Levenberg Marquadt non-linear algorithm least square analysis to the experimental data. The proposed submodel for the virtual origin reads

$$\frac{s_{virtual}}{d_{Nozzle}} = 1.92 \cdot ln(Re_{Nozzle}) - 23.1 \quad \text{for} \quad 0 < Re_{Nozzle} < 3.0 \cdot 10^5$$

Here the effect of liquid viscosity on the virtual origin is apparent by including the nozzle Reynolds number in the submodel for the prediction of the virtual origin. Increasing the liquid viscosity results in an increment of the predicted virtual origin of the two-phase free jet flow. The final expression of the proposal for the centerline droplet velocity is a function of the independent parameters, i.e., nozzle flow conditions as well as the normalized downstream distance and reads

$$u_{droplet_{centerline}}(s) = u_{expansion_{Air}} \cdot$$

$$\left[\left(1 + \left(1 - exp\left(-A \cdot \sqrt{\frac{s}{d_{Nozzle}} - \frac{s^2_{virtual}}{d^2_{Nozzle}}} \right) \right) \right) \cdot exp\left(-0.158 \cdot \sqrt{\frac{s}{d_{Nozzle}} - \frac{s^2_{virtual}}{d^2_{Nozzle}}} \right) \right]$$

$$\text{with} \quad A = \frac{22.5}{Re_{Nozzle}} \cdot \frac{\eta_{Air(P_{ambient})}}{\eta_{Liq}} \cdot \sqrt{\frac{\rho_{Liq}}{\rho_{Air(P_{ambient})}}} \quad ,$$

$$u_{expansion_{Air}} = u_{Nozzle} + \frac{(P_{outlet} - P_{ambient}) \cdot A_{Nozzle}}{\dot{M}_{Total(Nozzle)}} \quad \text{and} \quad u_{Nozzle} = \frac{\dot{M}_{Total(Nozzle)}}{\rho_{Nozzle} \cdot A_{Nozzle}}$$

The fitting constants in the proposal for the centerline droplet velocity were numerically determined by applying the Levenberg Marquadt non-linear algorithm. These constants, included in the expression for the parameter A, are addressing only the effect of the liquid viscosity on air entrainment, based on an order of magnitude estimates, the magnitude of the nozzle Reynolds number equalizes - on average - the magnitude of the square root of the liquid density to that of the ambient air. This can be taken as an evidence for the enhancement of the air entrainment with increasing only the liquid viscosity. On resuming the modelling, the expression for the centerline droplet velocity is finally given as a function of the air expansion velocity and the net interacting effects of the acceleration and the deceleration terms. The air expansion velocity is calculated based on the nozzle flow conditions. In the case of a two-phase jet dispersing in a vacuum ambient, this model would account only for the droplet acceleration that will continue to an infinite downstream distance, while in case of a two-phase jet dispersing into an ambient fluid with physical properties that are close to those of the jet, the deceleration is mainly dominant due to the intensive drag force exerted by the ambient fluid on the jet. Due to the expansion in the radial direction, a symmetry in the velocity profile is assumed. Hence, the entrainment affects the droplet velocity profile in the radial direction. In the next section, the normalized mean droplet velocity is considered.

5.1.3 Normalized mean droplet velocity

In the normal distance to the jet centerline, the proposed model for the normalized mean droplet velocity distribution reads

$$\frac{u(s,\,r)}{u_{droplet_{centerline}}(s)} = \exp\left(-ln2\left(\frac{r}{C_{Ent,\,2ph}\,(s - s_{virtual})}\right)^{1.3}\right)$$

The two-phase entrainment coefficient and the virtual origin submodels will be identical with these used for the prediction of the droplet centerline velocity. The two-phase entrainment coefficient and the centerline velocity are, by tradition, the basis for modelling the normalized mean droplet velocity distribution where a rotationally uniform air velocity field is ideally assumed. The bell-shaped distribution will be established for the droplet velocity profile in the normal plane to the jet flow. While a shift is introduced in the droplet motion away from the symmetry due to the gravity effect, leading subsequently to droplet rain out with nozzle downstream distance. The modelling of two-phase entrainment coefficient is described in the following section.

5.1.4 Two-phase entrainment coefficient

On reviewing the former definition equation, the two-phase entrainment coefficient will be derived with respect to the nozzle axial distance in order to generate a basic mathematical relation for the fitting. The derivation reads

$$\frac{dC_{Ent,\,2ph}}{ds} =$$

$$\frac{1}{\dot{M}_{Total}(s)\cdot(1-\dot{x}_{Air}(s))}\cdot\frac{d\dot{M}_{Ent}(s)}{ds} - \frac{\dot{M}_{Air,\,Nozzle} + \dot{M}_{Ent}(s)}{\left(\dot{M}_{Total}(s)\cdot(1-\dot{x}_{Air}(s))\right)^2}\left[\frac{d\left(\dot{M}_{Total}(s)\cdot(1-\dot{x}_{Air}(s))\right)}{ds}\right]$$

$$= \frac{1}{\dot{M}_{Total}(s)\cdot(1-\dot{x}_{Air}(s))}\cdot\frac{d\dot{M}_{Ent}(s)}{ds} -$$

$$- \frac{\dot{M}_{Air,\,Nozzle} + \dot{M}_{Ent}(s)}{\left(\dot{M}_{Total}(s)\cdot(1-\dot{x}_{Air}(s))\right)^2}\left[(1-\dot{x}_{Air}(s))\cdot\frac{d\dot{M}_{Total}(s)}{ds} - \dot{M}_{Total}(s)\cdot\frac{d\dot{x}_{Air}(s)}{ds}\right]$$

$$\text{with}\qquad \frac{d\dot{M}_{Total}(s)}{ds} = \dot{M}_{Ent}(s)\quad\text{and}\quad \frac{\dot{M}_{Liq}}{\dot{M}_{Total}(s)} \simeq 1 - \dot{x}_{Air}(s)\qquad,$$

whereby the assumption of no liquid droplet losses in the jet near field region to the ambient through the rain out is included. Thus, the liquid mass flow rate within the downstream near

field of the jet is assumed relatively conservative. The mass flow quality variation with the nozzle axial distance is obtained by

$$-\frac{\dot{M}_{Liq}}{\dot{M}_{Total}^2(s)} \cdot \frac{d\dot{M}_{Total}(s)}{ds} = -\frac{d\dot{x}_{Air}(s)}{ds} \quad \text{with} \quad \frac{d\dot{x}_{Air}(s)}{ds} = \frac{\dot{M}_{Liq}}{\dot{M}_{Total}^2(s)} \cdot \dot{M}_{Ent}(s)$$

With rearrangement, it can be finally rewritten as

$$\frac{d\dot{M}_{Ent}(s)}{ds} = \dot{M}_{Total}(s) \cdot (1 - \dot{x}_{Air}(s)) \cdot \frac{dC_{Ent,\,2ph}}{ds} \quad \text{with} \quad \frac{dC_{Ent,\,2ph}}{ds} = \frac{B}{d_{Nozzle}} \cdot \sqrt{\frac{\rho_{Air(P_{ambient})}}{\rho_{Nozzle}}}$$

By integrating this equation and using the experimental data and those of Surma [96] for the adjustment of the constants, the entrainment coefficient variation with nozzle downstream distance reads

$$C_{Ent,\,2ph}(s) = \begin{cases} 0.11 & \dot{x}_{Air(Nozzle)} = 0 \\[2ex] 0.11 - \dfrac{0.02}{1 - \dot{x}_{Air(Nozzle)}} \cdot \sqrt{\dfrac{\rho_{Air(P_{ambient})}}{\rho_{jet}(s)}} & 0 < \dot{x}_{Air(Nozzle)} < 1 \end{cases},$$

$$\rho_{jet}(s) = 1 / \left(\frac{\dot{x}_{Air}(s)}{\rho_{Air(P_{ambient})}} + \frac{1 - \dot{x}_{Air}(s)}{\rho_{Liq}} \right) \quad \text{for} \quad s > 30 - 40\, d_{Nozzle}$$

The proposed model, for the two-phase entrainment coefficient, is applied in case of air/ liquid phase free jet flow. The constant value of 0.11 is valid in case of only single-phase liquid dispersion flow. Indeed, the constant value of 0.02, in the definition for the two-phase entrainment coefficient, substantially differs from the values stated in the literature which range between 0.26 and 0.3. This difference mainly originates from the proposition of critical two-phase flow conditions at the nozzle outlet, which were not considered in most of the other studies.

The decrease of the two-phase entrainment coefficient with the nozzle downstream distance was not considered in previous studies. Indeed, the resulting linear dependence of the two-phase entrainment coefficient on the downstream distance in the Similarity region is consistent with the assumptions by Wygnanski et al. [115] that the turbulent two-phase free jet will approach a self preserving state. It is worth mentioning that the variation of the two-phase entrainment coefficient, with the downstream distance, is a fitting peculiarity in the momentum dominated regime of the two-phase free jet flow. On the other hand, the air entrainment is a real physical effect of the phenomena dominating the free jet flow within the Buoyancy/ gravity and the Atmospheric turbulence regimes, see Fig. 1. For the substantiation of this hypothesis, the effect of liquid viscosity on the entrainment coefficient, in the momentum dominated regime, will be illustrated in the following section.

5.2 Effect of liquid viscosity on entrainment coefficient

Fig. 39 is intended to clarify the effect of liquid phase viscosity on the net effect coefficient of the acceleration and deceleration terms of this new proposal, the predicted two-phase entrainment coefficient by Iannello et al., Ejet code and Surma model included for the purpose of comparison. These parameters are plotted as a function of the normalized axial distance in free jet flow of air/ water, resp., glucose syrup with a viscosity of 100 mPa s. The nozzle diameter is 10 mm and the stagnation pressure of 2 bar prevailed while almost identical flow conditions are conserved.

Air/ liquid phase free jet

		Air/ water	Air/ glucose syrup (100 mPa s)
Nozzle outlet diameter	:10 mm		
Stagnation pressure	:2 bar		
Mass flow rate		:2041 kg/(m² s)	:2416 kg/(m² s)
Mass flow air quality		:6.7 %	:5.2 %
Homogeneous outlet velocity		:102.2 m/s	:95.6 m/s
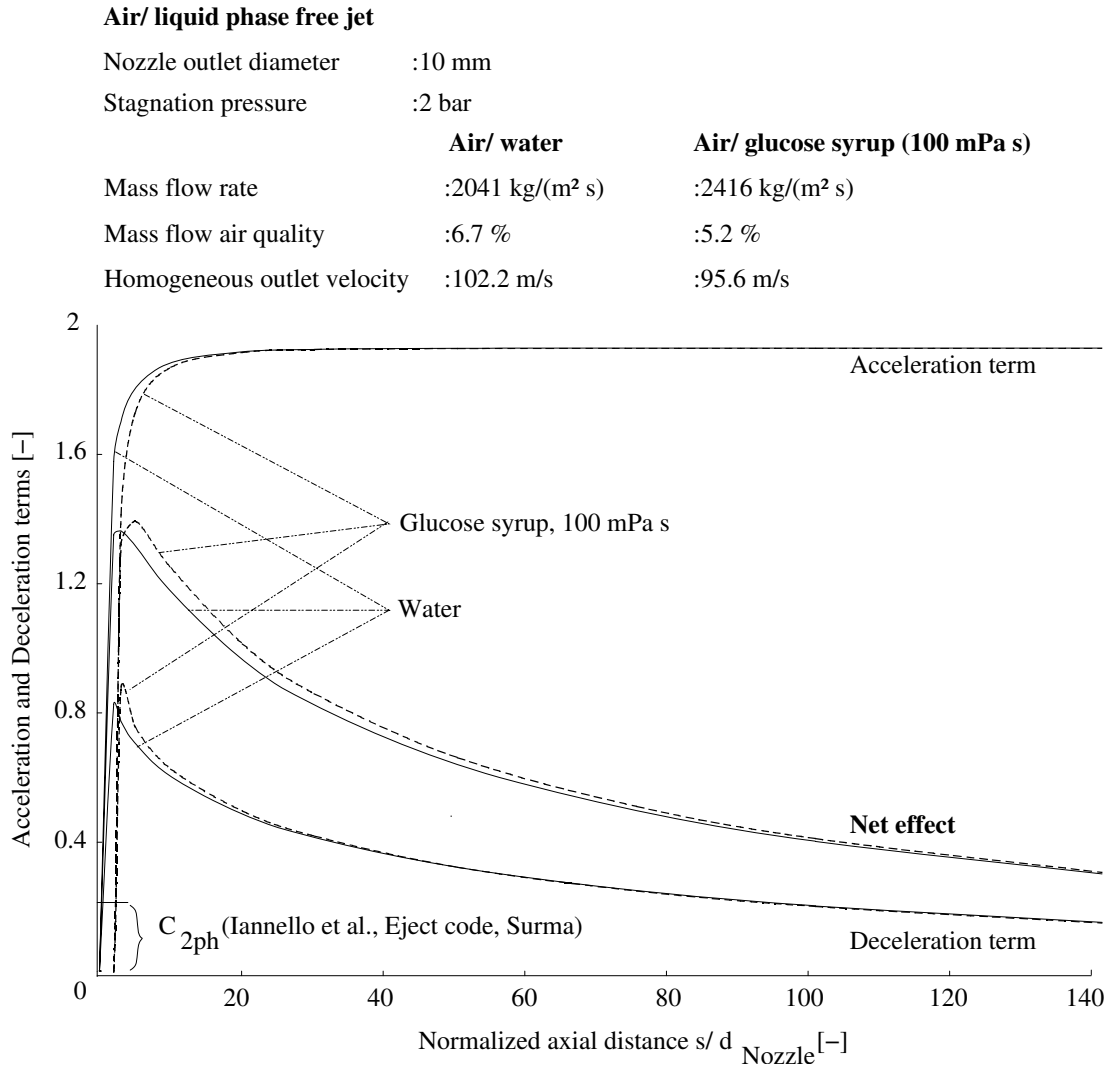
Fig. 39: Acceleration and deceleration terms according to proposal for centerline droplet velocity and predicted two-phase entrainment coefficient by Iannello et al., Ejet code and Surma model as a function of the normalized axial distance in free jet flows of air and water, resp., glucose syrup with a viscosity of 100 mPa s

The droplet acceleration term increases rapidly in the jet near field region, practically independent of the viscosity. It then levels off, establishing an asymptotic boundary value in the

76

relatively jet far field region. Contrary to this, the deceleration term for the syrup and that for the water begins to increase steeply, exhibiting a maximal peak and then decreases gradually with the normalized axial distance. Apparently, the increase in the deceleration term is attained within a nozzle downstream distance shorter than the established virtual origin distance for both jet flows. The net effect is obtained from the multiplication of the magnitude of these two terms at each relevant normalized axial distance. In total, the net effect firstly increases in the near field region due to the overwhelming effect of the acceleration term, then it decreases with the normalized axial distance due to the domination of the deceleration term on the behavior of the droplet for both jet flows. By comparing the behavior of the net effect term for the glucose syrup with that for the water, it can be seen that the entrainment process is enhanced in case of a viscous liquid phase. The physical reason is that, in total, increasing the liquid phase viscosity promotes the droplets generated from the liquid bulk to establish a relatively smaller Sauter mean diameter. Thus the droplets will be affected by the surrounding air to a relatively greater extent and, hence, the air entrainment process is enhanced. The concurrent increase of the liquid density and surface tension only have a small direct effect on the entrainment.

By comparing the behavior of the variable net effect term to that of the other model coefficients, it can be taken as an evidence that, irrespective of the different coefficient definitions, the existence of both the air and the liquid phase inside the jet flow plays an efficient role in varying the air entrainment process within the momentum dominated regime, contrary to the conclusion stated by MacGregor [62]. These new improvements are employed in the proposed model for the prediction of the droplet velocity and rain out. In the next section, the reproductive accuracy in relation to other models will be presented.

5.3 Reproductive accuracy in relation to other models

For the aim of model re-evaluation, the results of the experimental centerline droplet velocity along with the model predictions by Iannello et al. [40], Ejet code [114] and Surma [96] as well as the proposed model are presented.

Centerline droplet velocity

The experimental centerline droplet velocity is plotted in Fig. 40 as a function of the normalized axial distance in case of air/ glucose syrup free jet with a liquid phase viscosity of 100 mPa s, a nozzle diameter of 10 mm at a stagnation pressure of 2 bar and a mass flow quality of 5.2 %. The parameter is the self establishing Sauter droplet diameter. Firstly, a substantial change is observed in the experimental Sauter droplet diameter along with the normalized axial distance. No systematic trend can be deduced for its variation with the normalized axial distance, although this change supports the idea that there is a combined effect of the air entrainment and the subsequent liquid fragmentation, which physically affects the local droplet size distribution.

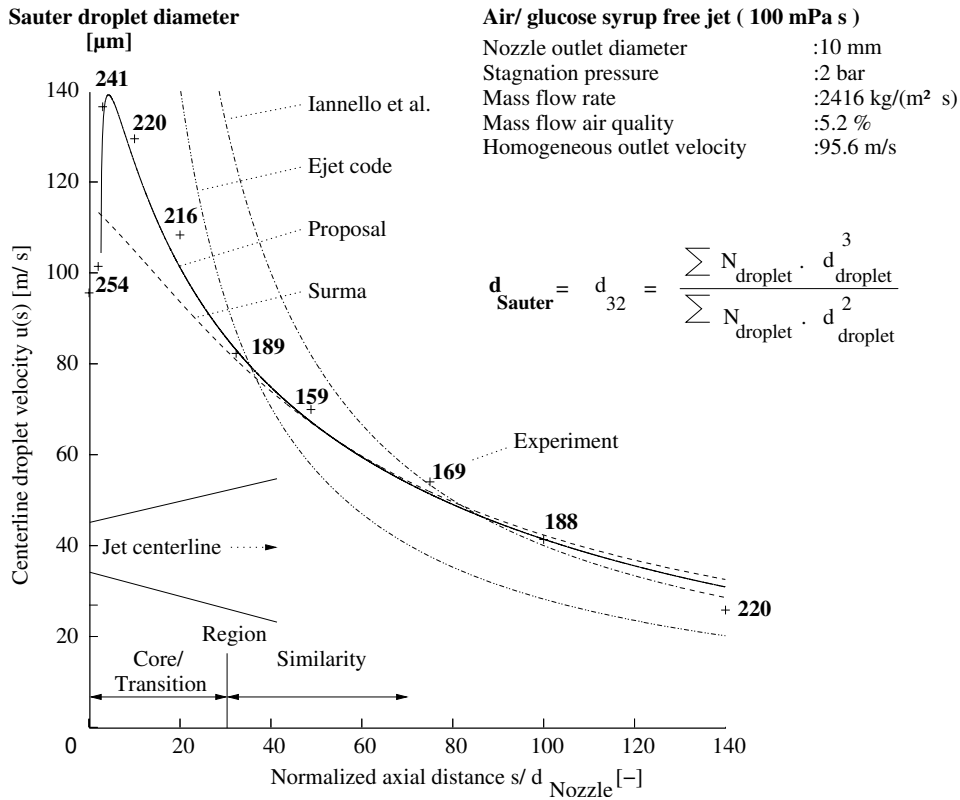Fig. 40: **Experimental centerline droplet velocity and Sauter droplet diameter as a function of the normalized axial distance and predictions by Iannello et al., Ejet, Surma and proposed model in case of viscous liquid phase**

Indeed, this is consistent with the findings by Mansour et al. [65], claiming a primary breakup to form relatively larger fragments of the liquid phase that will be prone for further downstream

secondary breakup. Thereby, a bimodal droplet size distribution will be expected to develop as confirmed by Bach et al. [2]. Basically, the experimental centerline droplet velocity starting from a predicted homogeneous velocity of 95 m/s increases firstly in the near jet field and then, after performing a maximum, decays with the normalized axial distance approaching an asymptotically lower value of about 26 m/s. This trend is next compared with the predictions according to the models by Surma [96] and Iannello et al. [40] as well as by using the Ejet code [114].

Evidently, the models by Iannello et al. and Ejet code exhibit an improper reproduction of the experimental centerline velocity, which indicates that the actual length scale for the velocity decay is somewhat different from that predicted by both models. This difference is mainly attributed to the constant value of the two-phase entrainment coefficient included in both models. In comparison, the model by Surma that was originally developed for jets consisting of air and relatively low viscosity liquid phase exhibits a significant underprediction in the Core/ Transition region, which consequently vanishes, allowing for a rectified prediction in the Similarity region. Indeed, it fails to predict the centerline droplet velocity in the jet near field region, where the local jet flow conditions are still adjacent to the nozzle outlet conditions. Moreover, the model by Surma was found to underpredict the experimental results especially for the case of air and relatively high viscosity liquid phase where then the underprediction of the experimental data is even more pronounced. In contrast to this, the proposed model allows for a pertinent prediction of the experimental centerline droplet velocity in the Core/ Transition as well in the Similarity region with the exception of the data in the Expansion Zone. Obviously, the predicted length scale for the centerline droplet velocity, by inclusion of a variable two-phase entrainment coefficient as a function of the normalized axial distance along with a virtual origin as a dependent function of the nozzle flow conditions, allows for an adequate reproduction of the experimental data. Subsequently, the reproductive accuracy of the centerline droplet velocity will be presented in the next section.

Reproductive accuracy of the centerline droplet velocity

Tab. 5 contains all data pertaining to the average reproductive accuracy of the centerline droplet velocity. The data rank between $\pm$ 12.6 m/s to $\pm$ 64.5 m/s for the absolute scatter, and between 9.8 % to 151 % for the logarithmic scatter. Altogether, the predictions according to the models by Ejet, Iannello et al. and Surma are in no single situation as accurate as those of the proposal. This is not only valid for air/ water systems, but uniformly applicable for any two-phase air/ liquid phase flow system irrespective of choosing the absolute or the logarithmic scatter as an authoritative statistic measure. In total, only the proposal allows for a relatively satisfactory reproductive accuracy of the measurements.

| Liquid phase viscosity [mPa s] | Centerline droplet velocity scatter | | | | | | | |
| | Absolute $\pm S_{abs}$ [m/s] | | | | Logarithmic S_{ln} [%] | | | |
	Ejet code	Iannello et al.	Surma	Proposal	Ejet code	Iannello et al.	Surma	Proposal
1	35.4	32.1	21.8	13.6	90.0	71.8	28.5	15.7
8	64.5	56.1	32.1	19.9	150.7	107.7	47.6	28.6
70	60.5	57.2	30.3	25.6	138.5	118.8	39.8	21.8
100	52.8	45.3	34.5	25.3	104.4	72.8	51.1	29.2
325	31.1	28.4	32.2	12.6	69.7	56.2	27.5	9.8
760	61.5	53.7	28.7	27.2	134.7	94.4	42.0	38.6

Tab. 5: Average reproductive accuracy of the models by Ejet code, Iannello et al., Surma and the proposal for the centerline droplet velocity in free jet flow of air/ liquid phase on the basis of the absolute and logarithmic scatter

Exemplarily, in Fig. 41, the measured centerline droplet velocity is depicted against the predicted value for the case of free jet flow of air/ liquid phase with a viscosity of 100 mPa s, the nozzle outlet diameters of 3, 5 and 10 mm and stagnation pressures ranging between 2 and 7 bar with the mass flow air quality between 2 % and 33 %. The acceptable layout for these parity data are virtually taken within the limitation lines of $\pm 25\,\%$. Evidently, the model in the Ejet code and that by Iannello et al. largely overpredict the centerline droplet velocity. This is due to the (already mentioned) fact that both models are based on a constant two-phase entrainment coefficient irrespective of the nozzle downstream distance. In addition the model by Surma provides a predictive inaccuracy which is considerably high. Nevertheless, the data obviously are distributed almost systematically around the diagonal, but many of them are located outside of the acceptable limit. Hence, this model implies only a restricted extrapolation for two-phase dispersion flows in case of air/ high viscous liquid. In comparison, the proposal provides parity data that are distributed symmetrically around the diagonal confirming a physically sound comprehension of the trends within a wide range of the dispersion parameters.

Air/ glucose syrup free jet (100 mPa s)
Nozzle outlet diameter : 3 – 10 mm
Stagnation pressure : 2 – 7 bar
Mass flow air quality : 2.0 – 33.3 %

−25 %
+25 %

Ejet code

S_{abs} [m/s] ±52.8

S_{ln} [%] 104.4

Air/ glucose syrup free jet (100 mPa s)
Nozzle outlet diameter : 3 – 10 mm
Stagnation pressure : 2 – 7 bar
Mass flow air quality : 2.0 – 33.3 %

−25 %
+25 %

Iannello et al.

S_{abs} [m/s] ±45.3

S_{ln} [%] 72.8

Air/ glucose syrup free jet (100 mPa s)
Nozzle outlet diameter : 3 – 10 mm
Stagnation pressure : 2 – 7 bar
Mass flow air quality : 2.0 – 33.3 %

−25 %
+25 %

Surma

S_{abs} [m/s] ±34.5

S_{ln} [%] 51.1

Air/ glucose syrup free jet (100 mPa s)
Nozzle outlet diameter : 3 – 10 mm
Stagnation pressure : 2 – 7 bar
Mass flow air quality : 2.0 – 33.3 %

−25 %
+25 %

Proposal

S_{abs} [m/s] ±25.3

S_{ln} [%] 29.2

Measured centerline droplet velocity [m/s]
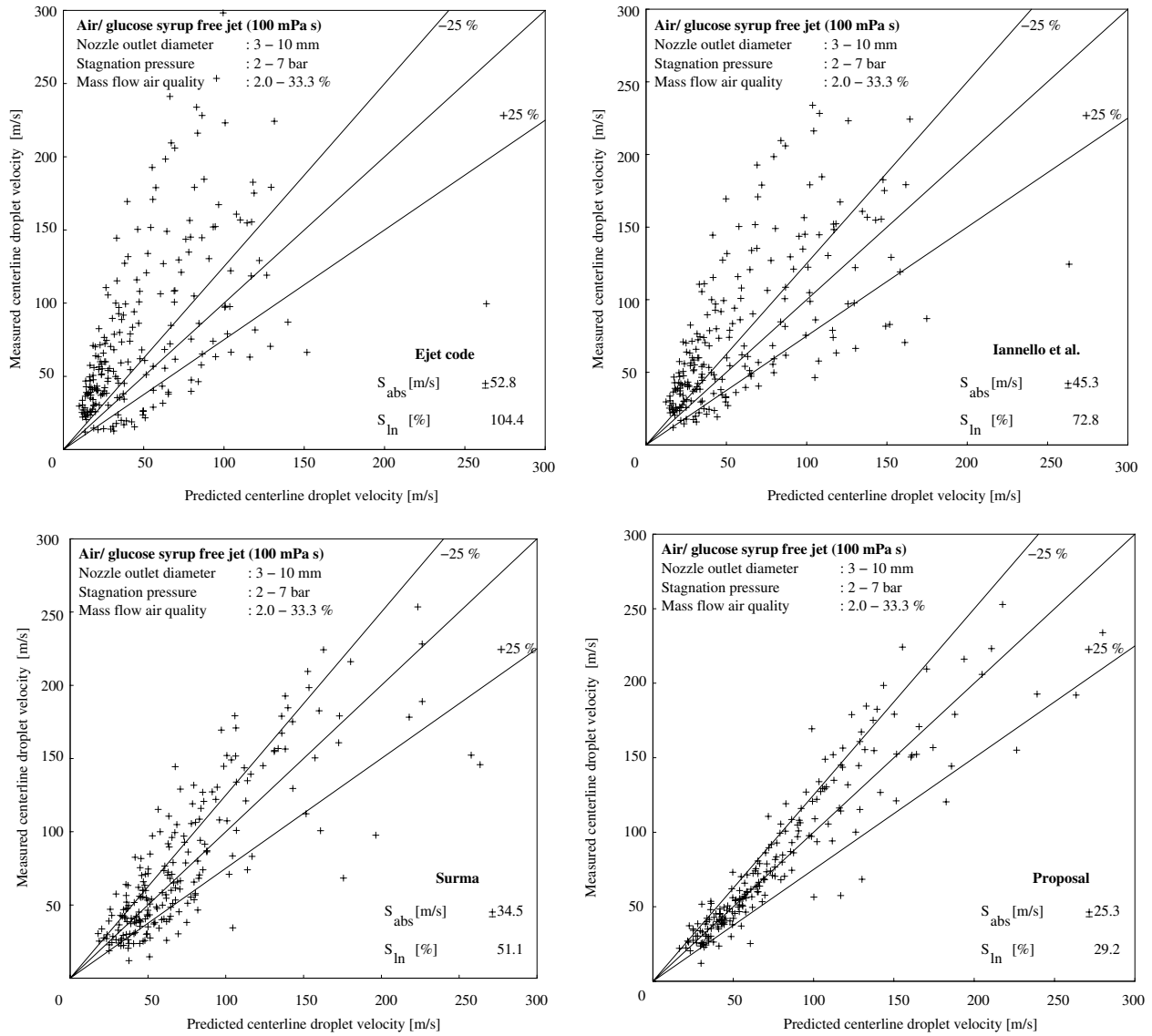
Predicted centerline droplet velocity [m/s]

Fig. 41: Average reproductive accuracy of the models by Ejet, Iannello et al., Surma as well as proposed model of the centerline droplet velocity in free jet flow of air and glucose syrup with a liquid viscosity of 100 mPa s

For a further demonstration of the model performance and generality, the experimental and the predicted results of the normalized mean droplet velocity subsequently are presented next.

Normalized mean droplet velocity

In Fig. 42, the experimental and the predicted normalized mean droplet velocity are plotted against the normalized radial distance for the air/ glucose syrup free jet flow with a liquid viscosity of 100 mPa s and identical flow conditions as stated in Fig 40. It is observed that the experimental velocity distributions in the Core/ Transition as well as in the Similarity region, independent of the nozzle downstream distance, relax to an almost symmetric bell-shaped velocity profile as in single-phase gas jet flows. The maximum droplet velocity is achieved as expected at the jet centerline, and monotonically decreases in the direction towards the jet

periphery, where it asymptotically approaches zero. In comparison, the model by Iannello et al., relying on the Top-hat velocity profile, is simply not applicable for reproducing the experimental data. In general, the Gaussian profile with an exponent of two, as implemented in the Ejet code, qualitatively describes the trend of the data, while the model by Surma and the proposal are allowing for the most pertinent predictions irrespective of the nozzle downstream distance. Indeed, by using a variable two-phase entrainment coefficient for the prediction of the droplet velocity by the proposal, the velocity distributions may slightly differ with the nozzle downstream distance but still adjacent to each other. Hence, it was postulated that these distributions are also independent of the nozzle downstream distance.
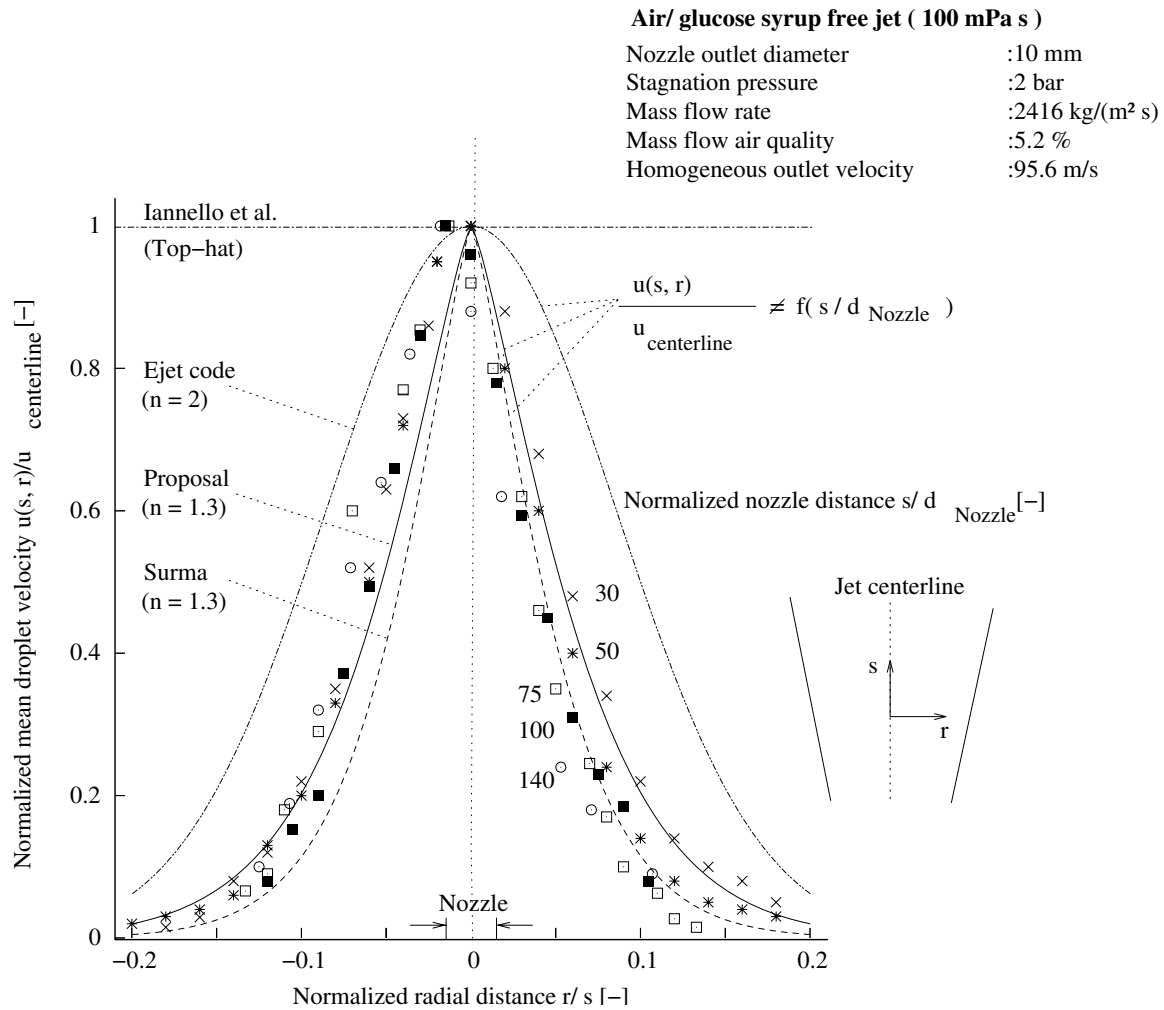
Fig. 42: Experimental normalized mean droplet velocity as a function of the normalized radial distance and predictions by Iannello et al., Ejet, Surma and the proposed model in case of viscous liquid phase

It is worthy mentioning that the maxima in the velocity profiles were obtained at a normalized radial distance of around -0.03 in the lower jet plane for the normalized axial distances of 75, 100 and 140. Within this relatively jet far field region, gravity already significant affects the droplet velocity profiles in the free jet of air/ higher viscosity and density liquid phase

82

(relative to water) by interceding an apparent shift in the distribution and, hence, may lead to the droplet rain out further downstream. The results obtained for the droplet rain out will be next presented.

Droplet rain out

The experimental and the predicted dimensionless cumulative droplet rain out capture are exemplarily plotted in Fig. 43 as a function of the normalized axial distance for an air/ water free jet flow with a nozzle diameter of 5 mm and at a stagnation pressure of 3 bar. The air mass flow quality amounted to 1.1 % and 46.2 %.
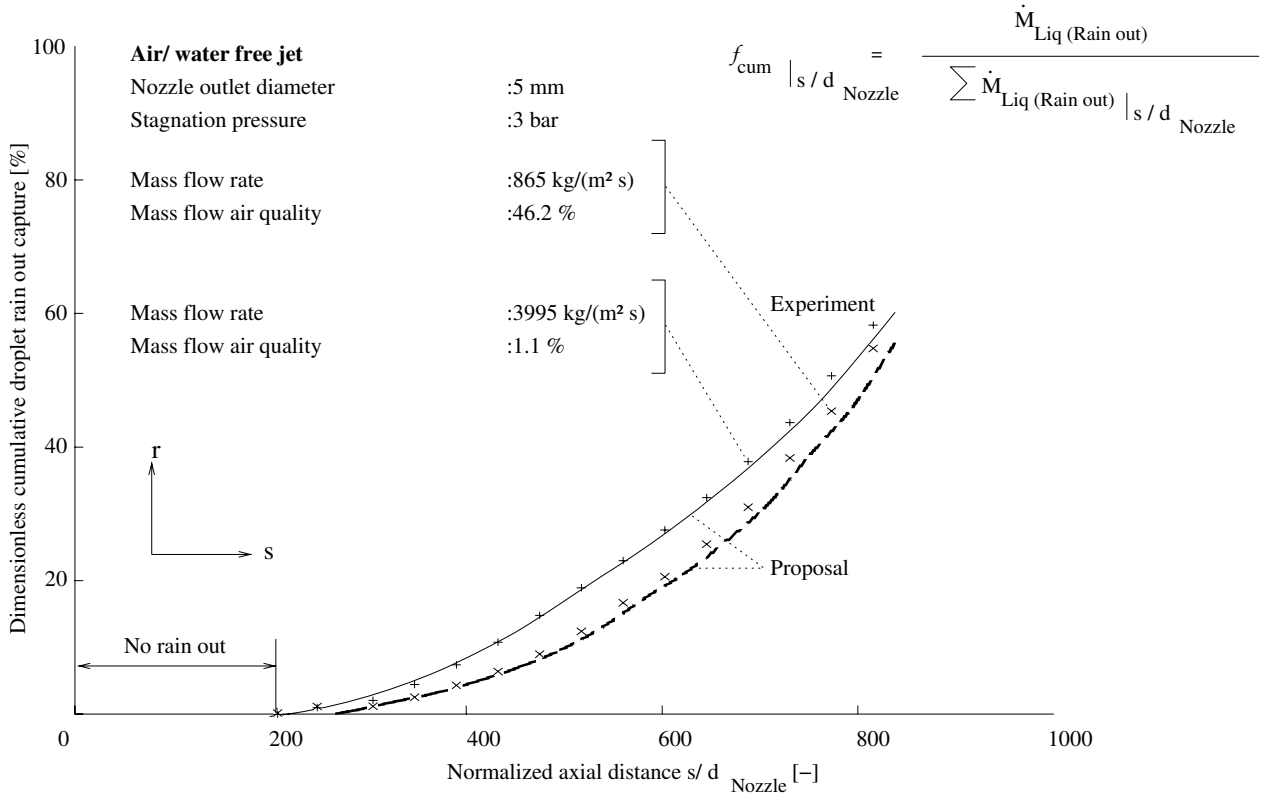
Fig. 43: **Experimental and predicted dimensionless cumulative droplet rain out capture in horizontal air/ water free jet flow as a function of the normalized axial distance**

Herewith, the dimensionless cumulative droplet rain out capture at a specific normalized axial distance is experimentally determined. Apparently, no significant droplet will rain out within a normalized axial distance of less than 200 nozzle outlet diameter in the case of both free jet flows. This indicates that each dispersion flow disposes of a momentum large enough to overcome, to a large extent, the gravity effect on the formed droplets even for a low quality dispersion. Downstream of this distance, the droplet rain out starts increasing exponentially with the distance. This is the consequence that the droplets have now exchanged their remaining momentum with the ambient air to such an extent, that they start to fall out of the

83

jet boundaries. At this stage, intensive interactions between the droplets themselves are to be expected, due to the fact that large droplets are settling down and falling freely under the effect of the gravity. While the smaller sized droplets remain airborne for a further downstream distance, because they have a relatively higher response to the air flow field shearing due to their larger specific interface. It is also known that a high quality dispersion is accomplished with a high air mass flow rate, thus, a relatively more vigorous air flow field than that in the case of a low quality dispersion will be established. Consequently, the higher impact that will force the droplets to remain airborne for further downstream distance. This ultimately leads to a lower amount of droplet rain out captured in the case of a high quality dispersion at a certain downstream distance. The proper predictions of the droplet rain out, in comparison to the experimental results under both free jet flow conditions, reflect also some merits of implementing the proposed model in predicting the droplet velocities in two-phase air/ liquid phase free jet flows.

5.4 Concluding remarks

Based on experimental results of horizontal and isothermal two-phase free jet flows in case of air/ water, resp., viscous liquid phase and data found in the literature, it is shown that a free jet flow of air and high viscosity liquid phase establishes a smaller Sauter droplet diameter. The air entrainment process is enhanced with the increasing liquid viscosity. The homogeneous two-phase liquid viscosity is introduced in the nozzle Reynolds number for the prediction of the virtual origin. The liquid density as well the surface tension will change with the increasing liquid viscosity. It is found that the liquid density has small direct effect on the entrainment model parameters. In the mean time, the surface tension does not affect the air entrainment, hence, is not included in the proposed model. A two-zone model was proposed for predicting the centerline droplet velocity, the normalized mean droplet velocity and the rain out distribution by using a variable two-phase entrainment coefficient. In comparison with other models, a higher statistical reproductive accuracy of the experimental data is achieved.

In the next chapter, implications of the results are addressed.

6 Implication of the results

This chapter summarizes the implications of the results along with the model validity for other dispersion conditions with noncircular outlets and inclined as well as vertical oriented two-phase free jet flows. Then, recommendations and extension of the current investigations to further work follow.

6.1 Model validity

The proposed model correlations properly describe the characteristics of two-phase air/ liquid phase free jet flow with a varied viscosity in the range from that of water to about 760 mPa s. It is believed that the Rosin, Rammler, Sperling and Bennet distribution, with an exponent of the value of 1.3, is a standard function in presenting the droplet size distribution. This finding is based not only on the pertinent reproduction of the experimental droplet size distribution, but also the incorporation of physical phenomena that are responsible for the establishment of the local droplet size distribution.

It is shown that a high viscosity liquid phase is associated with a smaller self establishing Sauter droplet diameter. This supports the general assumptions about the combined effects of liquid bulk disintegration and the air entrainment. The liquid viscosity dampens the waves at the liquid surface, thus, less fragmentation from the liquid bulk takes place. This allows more time for the droplet velocity to relax toward the ambient flow field and, in turn, enhances the air entrainment. These findings were employed in the new model for the droplet velocities and the rain out. A two-zone model involving the droplet acceleration/ deceleration was proposed for predicting the centerline droplet velocity and the normalized mean droplet velocity distribution, by the inclusion of a variable two-phase entrainment coefficient along with a submodel for the jet virtual origin as a function of the nozzle flow conditions. In relation to other jet models, a more satisfactory reproductive accuracy of the predicted length scale of the jet flow is achieved. For the rain out, more accurate predictions when extrapolating to other flow systems with a relatively higher viscosity are expected, due to the incorporation of the turbulence intensity variation with the nozzle downstream distance along with considering the centerline droplet velocity taken as a reference criteria for the droplet rain out model.

Furthermore, the current experimental and the analytical investigations are devoted to a better approach, that involves multi-physical trends for risk and hazard assessment and is an improved calculational method to be applied in computer codes. In a view of predicting the dispersion characteristics accompanied with non-isothermal flow conditions, a connection with the model by Michaelides et al. is proposed to account for the heat and mass transfer from/ to the liquid surface with altering the temperature as well as the subsequential effect on the entrainment process. It is assumed that such boundary driven transfer occur in the course of the short

time scale, and will not interfere with the long time scale of the breakup process since the jet turbulence and, hence, the intensive interactions between both phases, involved in the proposed model, will reduce the effect of the momentum and thermal thickness at the phase interface. Along with the assumption of a local equilibrium at the interface between the air and the liquid phase, the efforts to simulate the dispersion flow for a process unit are simplified. Particularly in terms of safety aspects, accurate predictions would be ascertained when extrapolating to other flow systems with a relatively higher viscosity and noncircular outlets.

6.1.1 Noncircular outlets

In view to apply the proposed model for other dispersion flows from noncircular outlets, it is customary to simply introduce the usual hydraulic diameter instead of the nozzle diameter. Nevertheless, the outlet flow cross section size will be required to describe more adequately the dispersion behavior in view of the emergency problems and, hence, being on the safe side with respect to the mass flow rate when simulating a worst credible scenario for a process unit.

6.1.2 Inclined and vertical free jet flows

This model is basically derived for horizontal free jet flows. In general, when a transition occurs to vertical or inclined free jet flows, the effects of the buoyancy and/ or the gravity forces are then significant on the droplet velocity behavior. The two-dimensional force balance accounts for the slip ratio, established between the droplet and air flow field, with respect to the dispersion flow direction. The model ability would, in this context, be modified to handle more complex site topographies.

6.2 Recommendations for further work

More investigations are required to account for the thermodynamic non-equilibrium effects on the air entrainment in predicting the dispersion flow characteristics associated with non-isothermal flow conditions, e.g., dispersion flow under flashing and/ or fluid dynamic critical conditions. The heat and mass transfer, occurring within the boundary layer, may not interfere with the breakup, consequently, the entrainment process, since the jet turbulence intensity is considered high enough to reduce the effects of the established momentum and thermal thickness at the phase interface. Furthermore, considerations for the case of inclined as well as vertical free jet flows are meriting a further work.

7 Summary

Two-phase free jet flows typically originate from the accidental relief of an industrial unit. For safety reasons, the spread and length of the jet must be known. A detailed model for the air entrainment that depends on the self establishing droplet size spectrum and velocity distribution is needed. The two-phase jet predictive models for droplet size and velocity include simplifications applied for single-phase flow or based on two-phase dispersion experiments performed with a liquid phase of relatively low viscosity. Further uncertainties remain with regards to the extrapolation of the laboratory results to real industrial releases with fluids of a relatively high viscosity. In the frame of this work, a validated two-phase entrainment model based on the upstream flow conditions for the case of air/ high viscosity liquid phase has been developed. In particular, the liquid phase breakup and the droplet rain out which in turn depends on the established droplet velocity and size spectra, will provide sufficient information to comprehend the dispersion behavior.

Experimental investigations on the dispersion of horizontal, isothermal two-phase air/ liquid free jet flows have been conducted, including measurements of droplet velocity and size using a two-dimensional Phase Doppler Anemometry in free jet flows with several nozzle conditions under systematic variation of the air mass flow quality and the liquid phase viscosity. For a proper interpretation of the results, high speed cinematography of the air/ liquid phase free jet flows at different locations has been performed. The entrainment is enhanced in relation to the increased liquid viscosity while all other nozzle flow conditions are maintained. At the same time, the liquid density as well the surface tension vary with increasing the liquid viscosity. No systematic trends are yet incorporated for the effect of these physical properties on air entrainment.

A two-zone entrainment model is proposed for predicting the droplet velocity and rain out. The model is based on physical effects and theoretical aspects of dispersion flows such as the droplet acceleration/ deceleration, the velocity profiles and the homogeneous flow definitions for the calculation of the two-phase jet properties. The model is validated depending on experimental data and those found in the literature, utilizing a variable two-phase entrainment coefficient with the downstream distance, as well as a submodel for the jet virtual origin as a function of the nozzle flow conditions. In comparison with other predictive models for two-phase dispersion flows, according to Ejet Code and Iannello et al. as well as Surma, a satisfactory reproductive accuracy of the experimental data has been achieved.

Nomenclature

2α	Beam intersection angle
A	Area
a	Acceleration
B	Perpendicular distance between the vectors of the two droplet trajectories
	Constant of the entrainment correlation
b	Impact parameter
β	Jet spreading angle [°]
	Slip coefficient in the Basset history force expression
C_{Ent}	Entrainment coefficient
C_o	Rouhani correlation constant
c	Concentration
Δ	Diameter ratio of the two colliding droplets
Δs	Interference fringe spacing
d_{mean}, $\bar{d}_{droplet}$	Mean droplet diameter
d_1, d_2	Diameter of two droplets before collision
d_{Sauter}, d_{32}	Sauter droplet diameter
d_{Nozzle}	Nozzle outlet diameter
d_{jet}	Jet diameter
η	Viscosity
ϵ	Mean void fraction
f	Degree of freedom
	Dimensionless droplet rain out capture
f_D	Frequency
F	Force
ϕ	Density ratio
	Sensor elevation angle $= 3.3°$
φ	Inclination angle of the conical part of the nozzle
J	Jet momentum
h	Enthalpy
g	Gravitational acceleration
L	Length
λ	Turbulent Schmidt number
λ_{wave}	Wave length
K	Constant
$\dot{M}$	mass flux
$\dot{m}$	mass flow rate
m	Exponent
n	Refractive index
$n_{droplet}$	Droplet number

ν	Kinematic viscosity
Oh	Ohnesorge number
P	Pressure
$p(d_{droplet})$	Probability function
Q_{cum}	Cumulative distribution
Re	Reynolds number
r	Radial distance
ρ	Density
S	Scatter
	Slip ratio of the mean velocities of both phases
s	Downstream distance
$s_{virtual}$	Jet virtual origin
σ	Static surface tension
σ_G	Standard deviation
t	Time
θ	Inclination angle between the two vectors of droplet trajectories
	Sensor off-axis angle with respect of the cartesian coordinates
$u_{droplet_{centerline}}$	Centerline droplet velocity
$u(s,\,r)$	Local droplet velocity
$U_1,\,U_2$	Velocity of the two droplets before collision
U^{new}	Droplet velocity after collision
U_{rel}	Relative velocity of the two droplets before collision
u_{io}	Superficial velocity
u'	Turbulent velocity fluctuation in longitudinal direction
$\dot{V}$	Volumetric flow rate
$\dot{x}_{Air}$	Mass flow quality
Y	Self-establishing quantity
$Y(t)$	Laplace transformation of the short time scale
Z	Azimuthal location
We	Weber number
w_R	Velocity difference constant

Indices

0.5	Half value
$2ph$	Two-phase mixture
$Aero$	Aerodynamic
$Atmos$	Atmospheric turbulence
abs	Absolute
$Buoy$	Buoyancy
Ent	Entrainment
$crit$	Fluid dynamic critical
cum	Cumulative
exp	Experimental
hom	Homogeneous
Liq	Liquid
ln	Logarithmic
max	Maximum
Mix	Mixing
$Moment$	Momentum
$pred$	Predicted
ref	Reference
rel	Relative
$stagn$	Stagnation

References

[1] Azzopardi, B. J., Hewitt, G. F.: Droplets in Annular Two-phase Flow. Int. J. Multiphase Flow 23 (1997) 2, 1 - 53.

[2] Bach, W., Nürnberger, F., Philipp, K. and Schaper, M.: Statistische Beschreibung der Tropfengrößenverteilung bei stationären Zestärbeidsprocessen. Forsaking Ingenieurwesen 69 (2005) 3, 181 - 186.

[3] Bayvel, L. and Orzechowski, Z.: Liquid atomization. Washington, 1993.

[4] Birch, A. D., Brown, D. R., Dadson, M. G. and Swaffield, F.: The structure and concentration decay of high pressure jets of natural gas. Combust. Sci. Technol. 36 (1984), 249 - 261.

[5] Blaisot, J. B. and Adeline, S.: Instabilities on a free falling jet under an internal flow breakup mode regime. Int. J. Multiphase Flow 29 (2003), 629 - 653.

[6] Bousfield, D. W., Keunigs, G., Marrucci, G. and Denn, M. M.: Nonlinear-analysis of the surface tension driven breakup of viscoelastic filaments. J. Non-Newton. Fluid Mech. 21 (1986), 79 - 97.

[7] Bricard, P. and Friedel, L.: Two-phase jet dispersion. J. Hazardous Materials 59 (1998), 287 - 310.

[8] Brodkey, R. S.: The phenomena of fluid motions. Addison-Wesley, Reading 1969.

[9] Buchlin, J. M. and St. Geoerges, M.: Detailed single spray experimental measurements and one-dimensional modelling. Int. J. Multiphase flow 20 (1994) 6, 979 - 992.

[10] Bürgermeister, M.: Messungen von Tropfendurchmessern in Ölsprays. Wärmetechnik - Versorgungstechnik 45 (2000) 9, 32 - 39.

[11] Chen, S. K. and Lefebvre, A. H.: Discharge coefficient for plain orifice effervescent atomizers. Atomization and Sprays 4 (1994), 275 - 290, 291 - 301.

[12] Chiang, H. C. and Sill, B. L.: Entrainment models and their applications to jets in a turbulent cross flow. Atmospheric Environment 19 (1985) 9, 1425 - 1438.

[13] Clift , R., Grace, J. R. and Weber, M. E.: Bubbles, drops and particles. Academic Press, Yew York, 1978.

[14] Cohen, R. D.: Effect of viscosity on drop breakup. Int. J. Multiphase Flow 20 (1994) 1, 211 - 216.

[15] Cossali, G. E.: An integral model for gas entrainment into full cone sprays. J. Fluid Mech. 439 (2001), 353 - 366.

[16] Crow, S. C., and Champagne, F. H.: Orderly structure in jet turbulence. J. Fluid Mech. 48 (1971) 3, 547 - 591.

[17] Czerwonatis, N.: Zerfall flüssiger Strahlen und Widerstand von Tropfen in verdichteten Gasen am Beispiel des Verfahrens der Hochdruck-Sprüh-Extraktion. Diss. Techn. Univ. Hamburg-Harburg. VDI Verlag 2002, Reihe 3, Nr. 729.

[18] Dahm, W. J. A. and Dimotakis, P. E.: Measurements of entrainment and mixing in turbulent jets. J. AIAA 25 (1987) 9, 1216 - 1222.

[19] Dhainaut, M.: Literature study on observations and experiments on coalescence and breakup of bubbles and drops. SINTEF Report STF24 A0253, 2002.

[20] Das, P. K.: Prediction of maximum stable diameter of viscous drops in a turbulent dispersion. Chem. Eng. Technol. 19 (1996), 39 - 42.

[21] Epstein, M., Fauske, H. K. and Hauser, G. M.: A model of the dilution of a forced two-phase chemical plume in a horizontal wind. J. Loss Prev. 3 (1990), 280 - 290.

[22] Faeth, G. M., Hsiang, L. P. and Wu, P. K.: Structure and breakup properties of sprays. Int. J. Multiphase Flow 21 (1995) Suppl. 1, 99 - 127.

[23] Falcone, A. M. and Cataldo, J. C.: Entrainment velocity in an axisymmetric turbulent jet. Trans. ASME 125 (2003), 620 - 627.

[24] Fiber PDA: Installation and users guide. DANTEC measurement technology, 1994.

[25] Friedman, J. A. and Renksizbulut, M.: Interaction of an annular air jet with a non-evaporating liquid spray. Part. & Part. Syst. Charact. 11 (1994), 442 - 452.

[26] Frohn, A. and Roth, N: Dynamics of droplets. Springer, Heidelberg, 2000.

[27] Görtler, H.: Berechnung von Aufgaben der freien Turbulenz auf Grund eines neuen Näherungsansatzes. Z. angew. Math. Mech. 22 (1942) 5, 244 - 254.

[28] Grolmes, M. A. and Coats, S. G.: Progress report on high viscosity two-phase flow modelling. Part II 20th DIERS Users Group Meeting 1997, 1 - 15.

[29] Hanson, A. R., Domich, E. G. and Adams, H. S.: Shock tube investigation of the breakup of drops by air blasts. Phys. Fluids 6 (1983), 1070 - 1080.

[30] Havens, J. A. and Spicer, T. O.: Development of an atmospheric dispersion model for heavier than air gas mixtures. U.S. Coast Guard Report Nr. CGD2385, Washington DC, 1985.

[31] Hecht, E.: Optics. New York, 1987.

[32] Hetsroni, G., Danon, H. and Wolfshtein, M.: Numerical calculations of two-phase turbulent jet. Int. J. Multiphase Flow 3 (1977) 3, 223 - 233.

[33] Hetsroni, G. and Sokolov, M.: Distribution of mass, velocity and intensity of turbulence in a two-phase turbulent jet. J. Applied Mech. 38 (1971), 315 - 327.

[34] Hewitt, G. F., Mayinger, F. and Riznic, J. R.: Phase interface phenomena in multiphase flow. New York, 1991.

[35] Hill, B. J.: Measurements of local entrainment rate in the initial region of axisymmetric turbulent air jets. J. Fluid Mech. 51 (1972) 4, 773 - 779.

[36] Hirst, E. A.: Analysis of round, turbulent buoyant jets discharged to flowing stratified ambients. Oak Ridge National Lab. (1949), ORNL 4685.

[37] Hoyt, J. W., Taylor, J. J., and Runge, C. D.: The structure of jets of water and polymer solution in air. J. Fluid Mech. 63 (1974) 4, 635 - 640.

[38] Hsiang, L.P. and Faeth, G.M.: Drop deformation and breakup due to shock wave and steady disturbances. Int. J. Multiphase Flow 21 (1995) 4, 545-560.

[39] Hussein, H. J., Capp, S. P. and George, W.: Velocity measurements in a high Reynolds number momentum conserving, axisymmetric, turbulent jet. J. Fluid Mech. 258 (1994), 31 - 75.

[40] Iannello, V., Rothe, P. H. and Wallis, G. B.: Aerosol research program: Improved source term definition for modelling the ambient impact of accidental release of hazardous liquids. Proc. Loss Prevention Symposium, Oslo 58 (1989), 1 - 30.

[41] Imine, B., Saber-Bendhina, A. and Imine, O.: Effects of a directed co-flow on a non-reactive turbulent jet with variable density. J. Heat Mass Transfer 42 (2005), 39 - 50.

[42] Ishii, M. and Grolmes M. A.: Inception criteria for droplet entrainment in two-phase concurrent film flow. J. AIChE 21 (1975) 2, 308 - 318.

[43] Johnson, D. W. and Woodward, J. L. : RELEASE a model with data to predict aerosol rainout in accidental releases. New York, 1999.

[44] Khan, H. J.: Helium jet dispersion to atmosphere. NASA CR 189885, 1986.

[45] Knubben, G.: Numerical simulation method to predict droplet trajectories for designing industrial systems of IC-engines. Wibro Eindhoven, 1995.

[46] Kim, W. T., Mitra, S. K., Li, X, Prociw, L. A. and Hu, T. C. J.: A predictive model for the initial droplet size and Velocity distributions and comparison with experiments. Part. & Part. Syst. Charact. 20 (2003), 135 - 149.

[47] Ko, G. H. and Ryou, H. S.: Modelling of droplet collision - induced breakup process. Int. J. Multiphase Flow 31 (2005) 6, 723 - 738.

[48] Kolev, N. L.: Fragmentation and coalescence dynamics in multiphase flows. Experimental Thermal Fluid Sci. 6 (1993), 211 - 251.

[49] Kollár, L. E., Farzaneh, M. and Karev, A. R.: Modelling droplet collision and coalescence in an icing wind tunnel and the influence of these processes on droplet size distribution. Int. J. Multiphase Flow 31 (2005), 69 - 92.

[50] Krishna, K., Kim, T. K., Kihm, K. D., Rogers, W. J. and Mannan, M. S.: Predictive correlations for leaking heat transfer fluid aerosols in air. J. Loss Prev. Process Ind. 16 (2003), 1- 8.

[51] Kuhlman, J. K.: Variation of entrainment in annular jets. J. AIAA 25 (1987) 3, 373 - 379.

[52] Kumagai, M. and Endoh, K.: Effects of kinematic viscosity and surface tension on gas entrainment rate of an impinging liquid jets. J. Chem. Eng. Japan 15 (1982) 6, 427 - 433.

[53] Kuta, T. J., Plesniak, M. W. and Sojka, P. E.: Entrainment control for ligament-controlled effervescent atomizer sprays. Atomization and Sprays 13 (2003), 561 - 577.

[54] Langner, H.: Untersuchungen des Entrainment-Verhaltens in stationären und transienten zweiphasigen Ringströmungen. Diss. Techn. Univ. Hannover, 1978.

[55] Lee, C. H. and Reitz, R. D.: An experimental study of the effect of gas density on the distortion and breakup mechanism of drops in high speed gas stream. Int. J. Multiphase Flow 26 (2000) 2, 229 - 244.

[56] Lefebvre, A. H.: Properties of Sprays. Part. & Part. Syst. Charact. 6 (1989), 176 - 186.

[57] Li, M. and Folger, H. S.: Acoustic emulsification. Part 2. Breakup of the large primary oil droplets in a water medium. J. Fluid Mech. 88 (1978), 513 - 528.

[58] Liepmann, D. and Gharib, M.: The role of streamwise vorticity in the near-field entrainment of round jets. J. Fluid Mech. 245 (1992), 643 - 668.

[59] Lovalenti, P. M. and Brady, J. F.: The hydrodynamic force on a rigid particle undergoing arbitrary time-dependent motion at small Reynolds number. J. Fluid Mech. 256 (1993) 561 - 605.

[60] Lörcher, M.: Zestäuben von zweiphasigen Gemischen aus Flüssigkeiten und Gasen. Diss. Univ. Hannover, 2003.

[61] Lund, M. T., Sojka, P. E., Lefebvre A. H. and Gosselin, P. G.: Effervescent atomization at low mass flow rates. Part 1: The influence of surface tension. Atomization and Sprays 3 (1993), 77 - 89.

[62] MacGregor, S. A.: Air entrainment in spray jets. Int. J. Heat Fluid Flow 12 (1991) 3, 279 - 283.

[63] Malmström, T. G., Kirkpatrick, A. T., Christensen, B. and Knappmiller, K. D.: Centerline velocity decay measurements in low velocity axisymmetric jets. J. Fluid Mech. 246 (1997), 363 - 377.

[64] Mandhane, J. M., Gregory, G. A. and Aziz, K.: A flow pattern map for gas-liquid flow in horizontal pipes. Int. J. Multiphase Flow 1 (1974), 537 - 553.

[65] Mansour, A. and Chigier, N: Air-blast atomization of non-Newtonian liquids. J. Non-Newtonian Fluid Mech. 58 (1995), 161 - 194.

[66] Mayer, W. O. H. and Branam, R.: Atomization characteristics on the surface of a round liquid jet. Experiments in Fluids 36 (2004) 6, 528 - 539.

[67] Mayinger, F.: Strömung und Wärmeübergang in Gas-Flüßsigkeits-Gemischen. Berlin, Springer Verlag, 1982.

[68] McKeogh, E. J. and Ervine, D. A.: Air entrainment rate and diffusion pattern of plunging liquid jets. Chem. Eng. Sci. 36 (1981), 1161 - 1172.

[69] Michaelides, E. E.: Review - The transient equation of motion for particles, bubbles and droplets. J. Fluids Eng. 119 (1997), 233 - 247.

[70] Michaelides, E. E. and Feng, Z. G.: The equation of motion of a small viscous sphere in an unsteady flow with interface slip. Int. J. Multiphase Flow 21 (1995) 2, 315 - 321.

[71] Middlemann, S.: Modelling axisymmetric flows dynamics of films, jets and drops. Academic Press, 1995.

[72] Morton, B. R., Taylor, G. L. and Turner, J. S.: Turbulent gravitational convection from maintained and instantaneous sources. Proc. R. Soc. 234A (1956), 1 - 23.

[73] Muralidar, R.: A Two-phase release model for quantifying risk reduction for modified HF alkylation catalysts. J. Hazardous Materials 44 (1995), 141 - 183.

[74] Ohnesorge, W.: Die Bildung von Tropfen an Düsen und die Auflöung flüssiger Strahlen. Z. Angew. Math. Mech. 16 (1936), 355 - 358.

[75] O'Neill, P., Soria, J. and Honnery, D.: The stability of low Reynolds number round jets. Experiments in Fluids 36 (2004) 6, 473 - 483.

[76] Ooms, G.: A new method for the calculation of the plume path of gases emitted by the stack. Atmospheric Pergamon Press 6 (1972) 899 - 909.

[77] Piesche, M., Breitling, M. and Schütz, S.: Zeitliche und räumliche hydrodynamische Instabilitäten feststoffbeladener Flüssigkeitsstrahlen. Chem.-Ing.-Tech. 77 (2005) 6, 742 - 747.

[78] Pilch, M. and Erdman, C. A.: Use of breakup time data and velocity history data to predict the maximum size of stable fragments for acceleration-induced breakup of a liquid drop. Int. J. Multiphase Flow 13 (1987) 6, 741 - 757.

[79] Pitts, W. M.: Effects of global density ratio on the centerline mixing behavior of axisymmetric turbulent jets. Experiments in Fluids 11 (1991), 125 - 134, 135 - 141.

[80] Qian, J. and Law, C. K.: Regimes of coalescence and separation in droplet collision. J. Fluid Mech. 331 (1997), 59 - 80.

[81] Quinn, W. R.: Measurements in the near flow field of an isosceles triangular turbulent free jet. Experiments in Fluids 39 (2005), 111 - 126.

[82] Rayleigh, L.: On the stability of jets. Proc. Lond. Math. Soc. 10 (1878), 4 - 13.

[83] Reitz, R. D.: Atomization and droplet breakup collision/ coalescence and wall impingement. Multiphase Science Technology 15 (2003) 1-4, 343 - 348.

[84] Reitz, R. D. and Bracco, F. V.: Mechanism of atomization of a liquid jet. Phys. Fluids 25 (1982) 10, 1730 - 1742.

[85] Richter, T.: Zertäuben von Flüssigkeiten: Düsen und Zertäuber in Theorie und Praxis. Renningen, Expert Verlag, 2004.

[86] Ricou, F. P. and Spalding, D. B.: Measurements of entrainment by axisymmetrical turbulent jets. J. Fluid Mech. 11 (1961), 21 - 32.

[87] Rouhani, Z. S.: Modified correlations for void and two-phase pressure drop. AE-RTV-841, 1969.

[88] Sallam, K. A., Dai, Z and Faeth, G.M.: Drop formation at the surface of plane turbulent liquid jets in still gases. Int. J. Multiphase Flow 25 (1999), 1161 - 1180.

[89] Schefer, R. W., Hartmann, V. and Dibble, R. W.: Conditional sampling of velocity in a turbulent nonpremixed propane jet. J. AIAA 25 (1986) 10, 1318 - 1330.

[90] Schmelz, F. and Walzel, P.: Breakup of liquid droplets in accelerated gas flows. Atomization and Sprays 13 (2003), 357 - 372.

[91] Schlünder, E. U.: Über die Ausbreitung turbulenter Freistrahlen. Z. Flugwiss. 19 (1971) 3, 108 - 113.

[92] Seifert, H., Giesbrecht, H. and Leuckel, W.: Dispersion of heavy gases and single- and two-phase vapours escaping from vertical outlets. Ger. Chem. Eng. 7 (1984), 126 - 137.

[93] Sirignano, W.A.: Fluid dynamics and transport of droplet and sprays. Cambridge University Press, New York, 1999.

[94] Snyder, H. E. and Reitz, R. D.: Direct droplet production from a liquid film: a new gas-assisted atomization mechanism. J. Fluid Mech. 375 (1998), 363 - 381.

[95] Song, L. and John, A.: Entrainment characteristics of transient turbulent round, radial and wall impinging jets: theoretical deductions. J. Fluids Eng. 125 (2003), 605 - 612.

[96] Surma, R.: Analytische und experimentelle Untersuchung der Ausbreitung von isothermen, turbulenten Zweiphasen-Freistrahlen in ruhender Umgebung. Diss. Techn. Univ. Hamburg-Harburg, 2005.

[97] Teng, H., Kinoshita, C. M., and Masutani, S. M.: Prediction of droplet size from the breakup of cylindrical liquid jets. Int. J. Multiphase Flow 21 (1995) 1, 129 - 136.

[98] Theofanous, T. G., Li, G. L. and Dinh, T. N.: Aerobreakup in rarefied supersonic gas flows. J. Fluids Eng. 126 (2004), 516 - 527.

[99] Tickle, G. A., Jones, S. J., Martin, D., Ramsdale, S. A. and Webber, D. M.: Development and validation of integral models of two-phase jets. European Commission Final Report, AEAT/1389, Issue 1, 1997.

[100] Tseng, L. K., Wu, P. K. and Faeth, G.M.: Dispersed phase structure of pressure-atomized sprays at various gas densities. J. Prop. Power 8 (1992), 1157 - 1166.

[101] Van de Sande, E. and Smith, J. M.: Surface entrainment of air by high velocity water jets. Chem. Eng. Sci. 28 (1973), 1161 - 1168.

[102] Vandroux-Koenig, S. and Berthoud, G.: Modelling of two-phase momentum jet close to the breach, in the containment vessel of a liquefied gas. J. Loss Prev. Ind. 10 (1997) 1, 17 - 29.

[103] Varga, C. M., Lasheras, J. C. and Hopfinger, E. J.: Initial breakup of a small-diameter liquid jet by a high-speed gas stream. J. Fluid Mech. 497 (2003) 24, 405 - 434.

[104] Vogel, G. K.: Physik. Springer, Berlin, 1982.

[105] Walter, C. Mih.: Equations for axisymmetric and two-dimensional turbulent jets. J. Hydraulic Eng. 115 (1989) 12, 1715 - 1719.

[106] Walton, D., Spence, M. K. and Reynolds, B. T.: The effects of free stream air velocity on water droplet size and distribution for an impaction spray nozzle. Institution Mechanical Engineers 214 (2000) 5, 531 - 537.

[107] Webber, D. M. and Kukkonen, J. S.: Modelling two-phase jets for hazard analysis. J. Hazardous Materials 23 (1990), 167 - 182.

[108] Weber, C.: Zum Zerfall eines Flüssigkeitsstrahles. Z. Angew. Math. Mech. 11 (1931) 2, 136 - 159.

[109] Wheatly, C. J.: Discharge of Ammonia to moist atmosphere–Survey of experimental data and model for estimating initial conditions for dispersion calculations. SRD R410, UKAEA, 1987.

[110] Whitlow, J. D. and Lefebvre, A. H.: Effervescent atomizer operation and spray characteristics. Atomization and Spray 3 (1993), 137 - 155.

[111] Wierzba, A.: Deformation and breakup of liquid drops in a gas stream at nearly critical Weber numbers. Experiments in Fluids 9 (1990) 1, 59 - 64.

[112] Witlox, H. and Bowen, P.: Flashing liquid jets and two-phase dispersion. HSE Report 403, 2002.

[113] Wong, D. C. Y., Simmons, M. J. H., Decent, S. P., Parau, E. I. and King, A. C.: Breakup dynamics and drop size distributions created from spiralling liquid jets. Int. J. Multiphase Flow 30 (2004), 499 - 520.

[114] Woodward, J. L.: Dispersion modelling of an elevated high momentum release forming aerosols. J. Loss Prev. Process Ind. 2 (1989), 22 - 32.

[115] Wygnanski, I. and Fiedler, H.: Some measurements in the self-preserving jet. J. Fluid Mech. 38 (1969) 3, 577 - 612.

[116] Yarin, A.L.: Free liquid jets and films, hydrodynamics and rheology. John Wiley & Sons, New York, 1993.

Curriculum Vitae

Surname:	Al Rabadi
First name:	Said
Date of birth:	2nd of June 1977
Place of birth:	Ajloun/ Jordan
Nationality:	Jordanian
Marital Status:	Single

School Education:

1983 - 1989	Catholic Elementary School - Ajloun/ Jordan
1989 - 1993	Preparatory School - Ajloun/ Jordan
1993 - 1995	Secondary School - Ajloun/ Jordan
1995	High School Graduate - Ajloun/ Jordan

Academic Education:

1995 - 2000	B. Sc. Chemical Engineering - Jordan University of Science and Technology - Irbid/ Jordan
2000 - 2002	M. Sc. Process Engineering - Hamburg University of Technology - Hamburg/ Germany
2003 - 2007	PhD Process Engineering - Hamburg University of Technology - Hamburg/ Germany